DISSERTATION

RESPONSE OF A TISSUE EQUIVALENT PROPORTIONAL COUNTER TO DIFFERENT IONS HAVING A SIMILAR LINEAR ENERGY TRANSFER

Submitted by

Stephen Brant Guetersloh

Department of Environmental and Radiological Health Sciences

In partial fulfillment of the requirements
For the Degree of Doctor of Philosophy
Colorado State University
Fort Collins, Colorado
Summer 2003

COLORADO STATE UNIVERSITY

June 05, 2003

WE HEREBY RECOMMEND THAT THE DISSERTATION PREPARED UNDER OUR SUPERVISION BY STEPHEN BRANT GUETERSLOH ENTITILED RESPONSE OF A TISSUE EQUIVALENT PROPORTIONAL COUNTER TO DIFFERENT IONS HAVING A SIMILAR LINEAR ENERGY TRANSFER BE ACCEPTED AS FULFILLING IN PART REQUIREMENTS FOR THE DEGREE OF DOCTOR OF PHILOSOPHY.

Committee on Graduate Work

(Please print name under signature)

Hariharan Iyer
HARIHARAN IYER

Cary Zeitlin
CARY ZEITLIN

Robert Ullrich
ROBERT ULLRICH

Thomas Borak
THOMAS BORAK
Advisor Thomas B Borak

John D. Zamboni
Department Head/Director

ABSTRACT OF DISSERTATION

RESPONSE OF A TISSUE EQUIVALENT PROPORTIONAL COUNTER TO DIFFERENT IONS HAVING A SIMILAR LINEAR ENERGY TRANSFER

The Tissue Equivalent Proportional Counter (TEPC) is a part of the active dosimetry of current space missions, measuring high-energy charged particles making up the proton and galactic cosmic radiation (GCR) fields, as well as the fragmentation products produced when these radiations interact with shielding. It is also used to characterize high-energy charged particle beams produced by accelerators used at many tumor treatment facilities throughout the world. A proper understanding of its response to these types of radiation fields is required before an assessment of radiation quality and dose equivalent may be made with confidence.

Past studies have characterized detector response to a single high-energy ion, ^{56}Fe, with energies ranging from 200 to 1,000 MeV/nucleon. It was found that the TEPC could be used to accurately determine the average quality of high-energy charged particles, and therefore dose equivalent, if the dose mean lineal energy, $\overline{y}_d$, were used. The present study is an analysis of TEPC response to several high-energy ions having different charge and velocity, the square of their ratio, Z^2/V^2, chosen such that all ions have a similar Linear Energy Transfer (LET). Four ions, ^{14}N, ^{16}O, ^{20}Ne

and ^{28}Si, all having an LET of about 43 keV/μm were measured at the Heavy Ion Medical Accelerator (HIMAC) in Chiba, Japan with a spherical TEPC having a physical diameter of 1.27 cm. Results of this study indicate that the proper choice of using $\overline{y}_f$ or $\overline{y}_d$ to determine radiation quality and absorbed dose may depend on the associated momentum of the ion.

Stephen Brant Guetersloh
Environmental and Radiological
Health Sciences Department
Colorado State University
Fort Collins, CO 80523
Summer 2003

ACKNOWLEDGMENTS

A special thanks goes out to Dr. Thomas Borak who allowed me to join his group at Colorado State University. His guidance and support have proved to be an invaluable part of this project. As an advisor, he knew when to let his students take the proverbial long walk off a short pier, and when to throw out the life-preserver to bring us back to reality. In the long run, it was the amount of dedication and excitement he showed in every aspect of his work that set an example I believe few could match.

I would also like to acknowledge the group at Lawrence Berkeley National Laboratory, Drs. Cary Zeitlin, Lawrence Heilbronn, and Jack Miller. Their group provided the vast majority of the equipment and expertise behind this experiment. I am especially grateful for the long hours and intellectual insight provided by Dr. Cary Zeitlin, without whose support this project would not have taken place. I have learned much more from him than the scope of this paper implies, by spending many sleepless nights helping (watching) him run the data acquisition system. With the schedule he keeps as an experimentalist, much could be gained in the way of understanding the effects (or lack thereof in this case) of long-term sleep deprivation.

Finally, I would like to thank all the others who either had a role in the experiments or otherwise supported this work. The National Institute of Radiological Sciences in Chiba Japan for the use of the Heavy Ion Medical Accelerator (HIMAC) for the beam time they provided. Drs. Takeshi Murakami and Yoshiyuki Iwata, who spent long hours supporting this project. The funding provided by the National Cancer Institute, NASA's Specialized Center for Research and Training in Radiation Health, as well as the Japanese Society for the Promotion of the Sciences. I would also like to take the opportunity to thank the faculty and staff at Colorado State University for their continued support. I am grateful to my committee members, Drs. Ullrich and Iyer, for their contribution and guidance in this work. And last, but by no means least, Julie Asmus for the help (and coffee) she has provided over the years.

DEDICATION

To my wife, Ana, who over the years has put more hard work and sacrifice into this project than I have . . . . and who, I think, wanted to see its completion more than I.

TABLE OF CONTENTS

LIST OF TABLES

LIST OF FIGURES

FROM APPENDICIES

CHAPTER I - INTRODUCTION

Proper understanding of the instruments used in the dosimetry of ionizing radiation becomes much more important as technology advances and the types of radiations become more diverse. Medical treatment facilities now employ an increasing variety of accelerated ions for use in tumor treatment, therapy and research. Hundreds of patients per day are being treated with fast charged particles in tumor therapy facilities at several locations around the globe.[1] With the frequency and duration of manned space activities also increasing, the exposure to fast heavy ions from Galactic Cosmic Radiation (GCR) is of growing concern.[2,3] Though the relative number of high-energy, high-Z particles (HZE) is only about one percent of the GCR, their contribution to dose during a space mission is significant.[2,3] Proper interpretation and understanding of the spatial patterns of energy deposition from charged particles as they pass through and interact with tissue becomes more important for accurate dosimetry in radiation protection, radiotherapy and radiobiology.

A quantity representing the distribution of energy loss through ionization by a charged particle as it traverses a medium is known as Linear Energy Transfer (LET) and is approximated using the Bethe-Bloch stopping-power formula.[4,5] LET has been defined by the ICRU in Report 16 as follows:[6]

"The linear energy transfer or restricted linear collision stopping power (L_Δ) of charged particles in a medium is the quotient of dE, by dl where dl is the distance traversed by the particle and dE is the mean energy-loss due to collisions with energy transfers less than some specified value."

For a given medium and for the range of energies important in therapy and space dosimetry, the important variables in the Bethe-Bloch equation regarding the incident particle are the charge, Z, and the velocity, V, of the ion. By choosing the charge and velocity of two ions so that the ratio of their squares, Z^2/V^2, is equal, the LET of the two in a given medium are similar. Since they deposit about the same amount of energy per unit path length, one would expect each ion to have the same or similar effects on the medium. In fact, LET is the quantity typically used to determine radiation quality for radiation protection purposes, and is one of the dependent variables in the concept of Relative Biological Effect (RBE) in radiation biology.[7]

In an effort to compare the biological effectiveness of one ion to another, X-rays or ^{60}Co gammas are generally used as the standard. The RBE of a charged particle is defined as the ratio of the dose required of X or ^{60}Co irradiation to the dose required of the given charged particle necessary to produce the same biological effect.[8] When the dose rate and number of fractions are held constant for the accelerated ions, the RBE for a given endpoint is dependent only upon the LET of the particle.[7]

As charged particles pass through tissue the primary mechanism of energy loss is by Coulomb interaction with the outer electrons of the molecules of the

tissue.[5,7] The result is the ejection of secondary electrons which deposit their energy in the medium. The distribution of energies of these secondary electrons is generally dependent upon the energy of the incident particle, not the charge.

Different ions having the same LET may have vastly different energies, which becomes significant in the assumption that similar LET particles have similar biological effectiveness. For an ion having an energy of 800 MeV/nucleon, for example, the distribution of delta rays produced has a maximum energy of about 2.5 Mev, with an approximate range of 12.5 mm in tissue.[4] For incident ions having energies of only 100 MeV/nucleon the maximum energy an ejected electron can have is approximately 230 keV, a factor of ten less, with a maximum range of about 0.55 mm in tissue. While the two particles have the same LET, the different energy spectra of electrons produced in the two cases may have a different impact in the medium, which may be of critical importance for certain biological endpoints.

Tissue-Equivalent Proportional Counters (TEPC) have been commonly used for dosimetry due to their versatility as a radiation detection instrument.[9] They are flown aboard manned space missions as part of the active dosimetry program and are used to characterize high energy therapy beams.[10-14] Since charge is amplified within the detector, signals are considerably larger than those from an ion chamber and the detector can be used in the detection and spectroscopy of low energy X-rays.[15] Due to the (n,p) reaction in the wall surrounding the gas-filled cavity, the detector may also be applied to the detection of neutrons.[15]

The response of a spherical TEPC to high-Z, high-energy (HZE) has been characterized using various energies of ^{56}Fe, ranging from 200 to 1,000

MeV/nucleon.[16,17] Results of these experiments have shown that there are geometric and other factors involved in the design and construction of the TEPC that affect the pattern of energy deposition measured by the detector. In some cases this may be different from the patterns of energy deposited in a homogenous tissue medium. Electron production, for example, is augmented due to density differences between the fill gas and the surrounding wall of the detector.[16,17] The presence of the collecting anode and surrounding helix wire also increase electron production for ions interacting with them. Even with these factors, results have indicated that the TEPC may be used to accurately determine absorbed dose and to estimate the quality of the incident radiation.[16,17]

The objectives of this study focus on the analysis of several high-energy ions having similar LET. By simulating volumes on the order of mammalian cells, the sensitive volume of the TEPC was much smaller than the volume of energy deposition surrounding the track of all ions. Track structure theory indicates that particles with similar LET but different velocities may have different energy loss properties.[18-20] With velocities of the incident ions ranging from 80 MeV/nucleon to 800 MeV/nucleon, the amount of energy escaping the volume of the detector was therefore different in all cases.

Data were recorded for four charged particle species, ^{14}N, ^{16}O, ^{20}Ne, ^{28}Si, at the Heavy Ion Medical Accelerator (HIMAC) in Chiba, Japan. The ions and their energies were chosen based on the limitations of the accelerator facility so that the LET at the position of the TEPC would be similar. The energy loss for all ions at the point of measurement was within few percent of 43.5 keV/μm, the average LET for

all four. Over $1x10^6$ energy deposition events were recorded for each ion using a 1.27 cm diameter TEPC simulating a volume of unit density tissue having a one micrometer diameter. Results were compared with past studies of ^{56}Fe[16,17] and with track structure models.[18-20]

In a similar fashion as in previous studies of energetic ^{56}Fe, energy deposition events were recorded on a particle by particle basis to allow a more detailed analysis of the response of the TEPC. Position Sensitive Detectors (PSDs) placed both upstream and downstream of the TEPC measured both the charge and position of each incident particle. Selecting the ion of interest based on charge, and using information on the horizontal and vertical coordinates in each PSD, the path of every ion with respect to the center of the TEPC was reconstructed.

The first and second moments of the frequency distributions as a function of lineal energy (Chapter III) were compared. The quality of the incident radiation was determined using several methods and presented with results obtained using the method currently recommended by the ICRP, as presented in Publication 60.[21] Unlike past studies analyzing ^{56}Fe, the first moment of the energy deposition distribution after conversion to lineal energy was in some cases a more accurate choice in determining the quality of the incident radiation. Similar to those studies, however, the second moment was a good indicator of quality for ions with the largest momentum. By selecting $\bar{y}_F$ or $\bar{y}_D$ based on the momentum of the ion, the quality factors determined from the measured spectra are within six percent of that calculated using the ICRP 60 recommended method. Use of either summary statistic, without

reference to the momentum of the incident ion, gives a predictor of quality that is within seventeen percent in all cases.

CHAPTER II - REVIEW OF LITERATURE

Energy Lost by Ionization

The quantity representing the distribution of energy loss through ionization by a charged particle as it traverses a medium is known as Linear Energy Transfer (LET). The term was first defined by Zirkle to explain the differences observed on exposing bacteria, haploid and yeast cells to a variety of radiations.[22,23] In general, cell survival curves exhibited an exponential decrease in survival as a function of increasing dose. Furthermore, cells exposed to high LET alpha particles showed lower survival than the same cells exposed to low LET x-radiation at the same dose.[22]

About the same time that Zirkle introduced the concept of LET, a method of calculating the amount of energy transferred to a medium by ionizing radiation was proposed by Niels Bohr, later modified by Bethe and Bloch.[24] This was referred to as the collision stopping power of a particle in a given medium and described the rate of energy lost in the medium per unit track length of the ionizing particle, or dE/dx.[4, 5] (Appendix-A) For radiation protection and radiation biology, collision stopping power for charged particles is generally given in units of keV/μm and the term has been used interchangeably with LET.[5]

Use of LET in Radiation Protection and Radiobiology

I. Relative Biological Effect

Radiobiological experiments have shown that for a similar absorbed dose in tissue, high LET radiations generally produce a greater effect than low LET radiations.[22,25] To compare cellular response to different radiations the concept of relative biological effect (RBE) was introduced.[7] The RBE of a radiation is defined as the ratio of doses of a specified radiation type relative to a standard radiation that produces a certain effect for a specific biological endpoint.[8] Usually he standard chosen is 250 kVp X-rays or ^{60}Co gamma-rays. Equal doses of different types of radiation produce different levels of response in cells. The biological effects of radiation have therefore been described in terms of a dose-response relationship.[4,8,25] Historically, cell survival has been the response of interest, though other end points are now commonly used depending on the focus of the study.[8]

RBE is dependent upon the dose rate, the number of exposures (fractions), the biological endpoint studied and the radiation LET.[8,25] When the same endpoint is studied with the same dose rate and number of fractions, the RBE is generally dependent upon the LET of the radiation.[7] For the survival of mammalian cells, RBE has been shown to increase as a function of LET, having a maximum at an LET of about 100 to 110 keV/μm, then decrease sharply as shown in Fig.2.1.[8] The characteristics of this distribution, however, change with the endpoint studied so it is relevant only under the given conditions.[8]

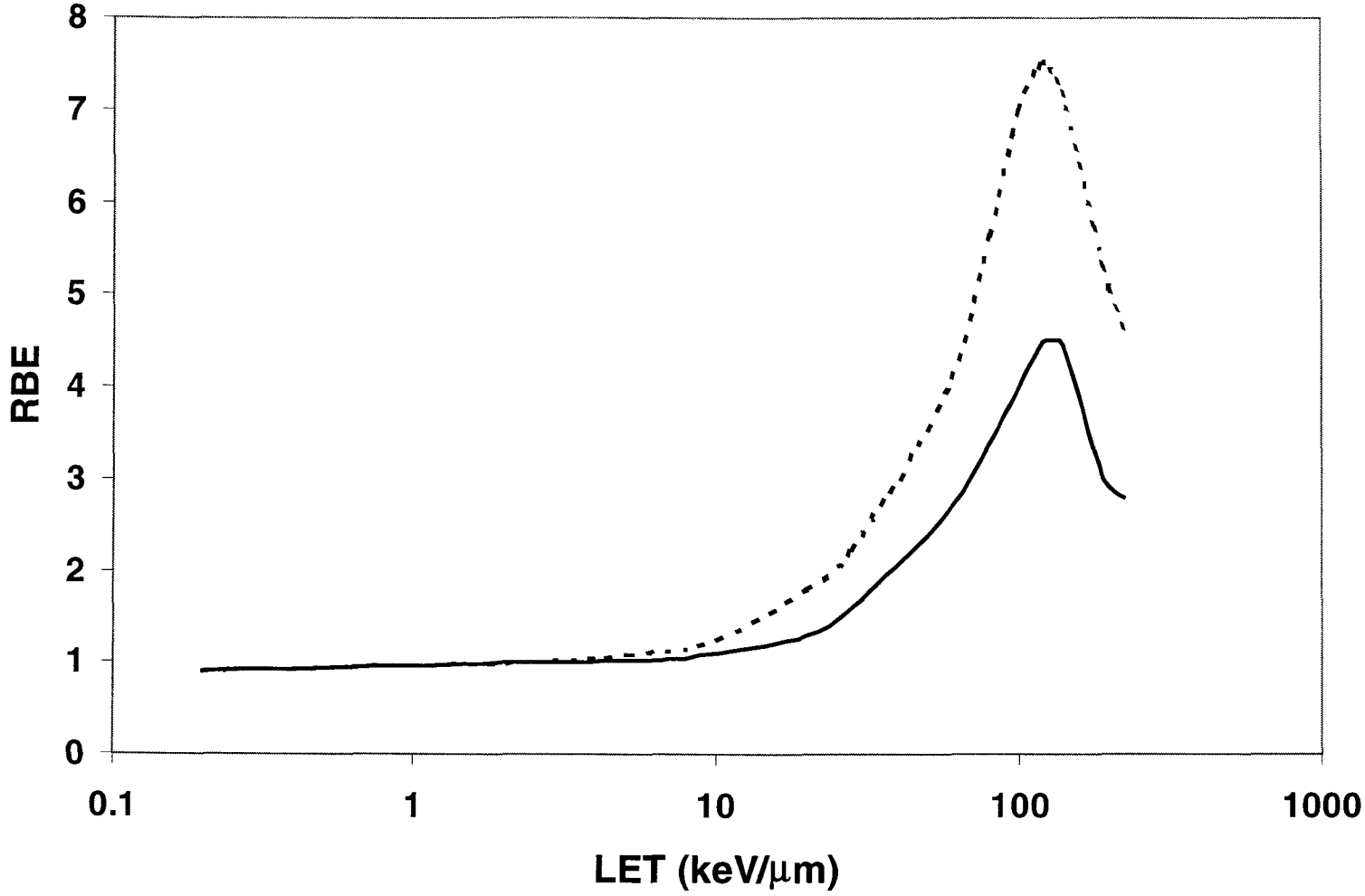

Fig. 2.1. Variation of RBE with LET for the Survival of Mammalian Cells. RBE rises to a maximum at an LET of about 100 keV/m to 110 keV/m then falls sharply. Black curve represents a survival level of 0.1. Dashed curve represents a survival of 0.8, illustrating that the absolute value of RBE depends here on level of damage. (from Hall, E.J., Radiobiology fo the Radiologist, 4th Ed., Lipcott Raven, (1994)

It was later shown that for heavy charged particles having similar LET, measured values of RBE might differ. Studying cell inactivation, protons with an LET of about 20 keV/μm could be up to 1.6 times more efficient than alpha particles at a similar LET.[26] Protons were also seen to be more efficient than neon in the induction of chromosome interchanges and breaks when both ions had an associated LET of about 30 keV/μm.[27] Plotting RBE as a function of LET for three heavy charged particles, ^{3}He, ^{12}C, and ^{20}Ne, the point of maximum RBE shifted to higher values of LET for heavier ions.[28] For a given LET, the RBE of ^{3}He was higher than that of the other ions.[28]

Thus variation in RBE for high-energy charged particles having similar LET may be dependent upon the track structure of the incident radiation. Based on calculations using track structure models, biological effectiveness has been thought to be a function of particle charge instead of LET.[29,30] Current results indicate that effectiveness is inversely related to particle velocity.[31] In fact, as early as 1963, the RBE Committee of the ICRP-ICRU recommended that RBE be confined to radiobiological studies and that for radiation protection the concept of a quality factor, Q, should be used.[32] However, determination of quality is also currently dependent upon the LET of the incident radiation.

II. Quality

For radiation protection purposes, a correlation is made between absorbed dose and the type of radiation delivering energy to the system by use of a radiation quality factor. The quality, Q, of a radiation is discussed in ICRU Report 40 as relating to the nature and energy of the charged particles that produce the absorbed dose.[33] The dose equivalent, H, was then defined as the product of absorbed dose and the radiation quality relating biological risk to exposure.

As more results of biological studies have been published, the definition of quality has been modified but has always been a function of LET.[21] New methods of determining quality based on microdosimetric measurements have also been proposed but have not been adopted.[34,33,35,36] Fig.2.2 compares current recommendations contained in ICRP Publication 60 and a method proposed by the ICRU in Report 40 using direct measurements of energy deposition. Also shown is a hybrid method given by Kellerer and Hahn that relates the second moment of the microdosimetric lineal energy distribution (Chapter III) to nine-eighths times LET, and adds a term to compensate for energy loss straggling.[34,37]

Energy Deposition in Microscopic Volumes

Variations in the observed values of RBE and Q for different radiations have been attributed to differences in the microscopic patterns of energy deposition for

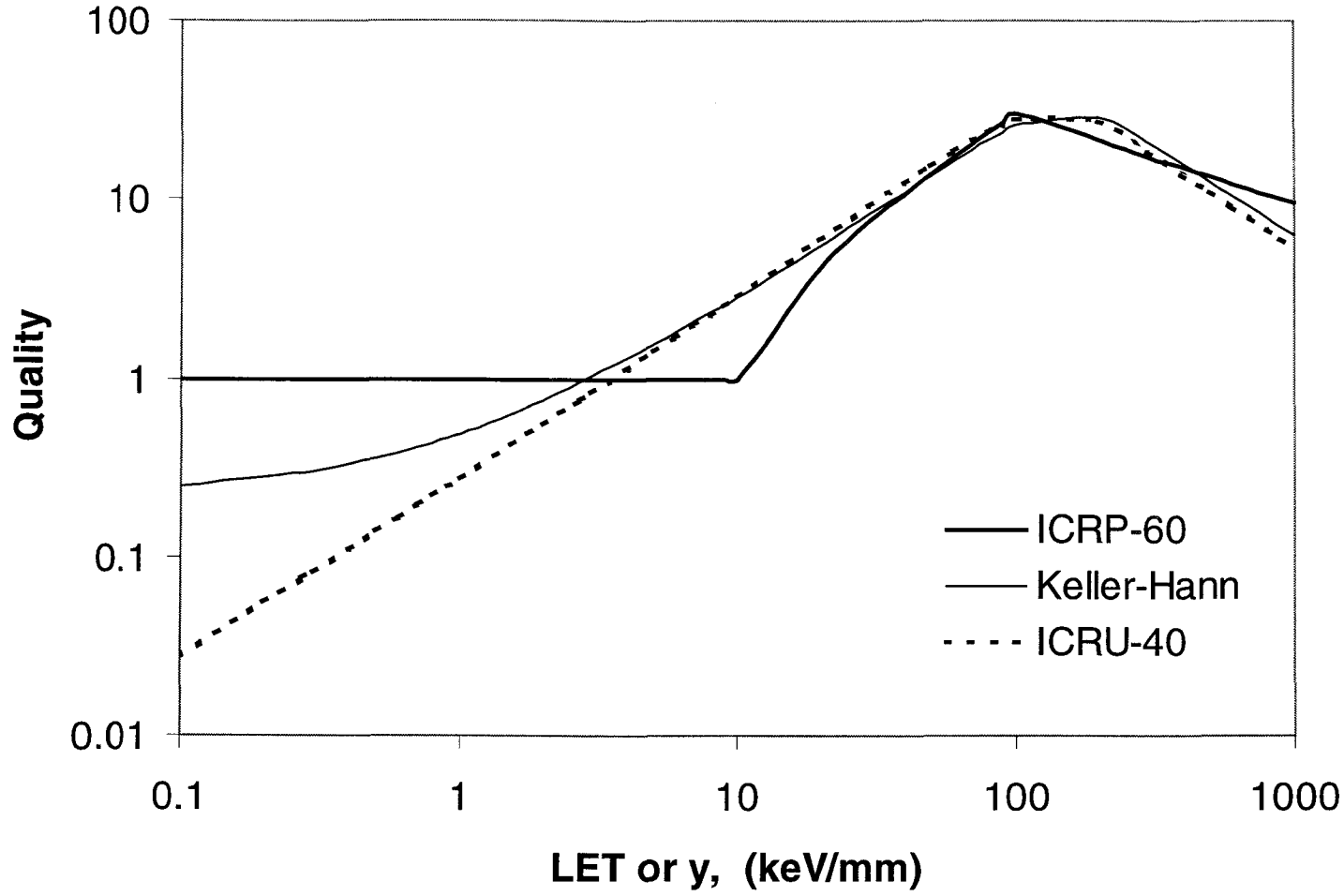

Fig. 2.2. Comparison of Methods Used to Determine Quality Factor. Heavy black line represents the current recommendations of the International Commission on Radiological Protection contained in Publication 60. Dashed line represents the recommendations of the International Commission on Radiation Units and Measurements as given in Report 40. The thin black line is a hybrid method proposed by Keller and Hahn (1988) in an attempt to account for energy loss straggling. The horizontal scale is LET for both ICRP-60 and Kellerer methods, and lineal energy for the ICRU-40 definition.

radiations of differing LET.[8,38] High LET radiations are said to be more 'densely ionizing' than low LET radiations.[8] However, calculations of LET describe only the pattern of energy lost, dE, in one direction, dx. In fact, two particles having the same LET may exhibit large differences in the patterns of energy loss in the radial direction.

Determination of LET is a value averaged over many variables giving the rate of energy lost by the charged particle with respect to distance traveled through the medium. For a medium of infinite radial dimensions, energy lost by the charged particle in the distance dx is equal to energy transferred to the medium. For radial distances smaller than the range of the ejected electrons, only a portion of the energy lost to the electrons is deposited within the site. Furthermore, energy transferred to the site is a stochastic process and may vary considerably.

Thus, for volumes commonly studied in microdosimetry, energy loss and energy deposited are not synonymous since energy deposition on a microscopic scale involves not only LET, but also the energy loss straggling and the dissipation of energy out of the volume by secondary electrons.[35] While energy loss is readily calculated for a known radiation, energy deposition to volumes much smaller than the radial extent of secondary electrons, such as biological cells, is not. To accurately determine energy deposition, either direct measurement simulating volumes of micrometer dimensions, or more complex models employing the full extent of the structure of an ion track must be used.

Track Structure Modeling

Using models to determine the structure surrounding the track of an energetic charged particle, it can be shown that a difference in LET is not required before differences in energy deposition patterns are found. Track structure modeling considers not only the forward direction of the incident ion, but also the radial extent of energy transfer. Some models require only the energy and velocity of the incident particle [18], while others examine the energies and directions of the ejected secondary electrons.[19,30,38,39] In all cases, an attempt is made to determine the energy deposited in a cylinder surrounding a charged particle track traveling a distance of one micrometer. (Details of the models are given in Appendix-C)

I. Structure of Heavy Ion Tracks

Chatterjee, et.al., derived an expression to determine energy deposition, in keV, within a cylinder surrounding a one micrometer track of a heavy ion.[18] The axis of the cylinder is the path of the ion having a length of one micron and the radius is the distance normal to the ion trajectory. It was determined that more than half of the energy was deposited in the very near vicinity of the ion trajectory due to a large number of low energy electrons with very short ranges. This dense region of local energy deposition was termed the core. The radius of the cylindrical volume describing this region was related only to the velocity of the ion. (Appendix C).

The other half of the energy liberated by the ion was contained in a larger volume surrounding the ion track, referred to as the penumbra. The outer radius of the penumbra was determined as a function of only the energy of the ion, in MeV/nucleon. Energy deposition within this region was equated with the inverse of the square of the radial distance from the track core. The fraction of energy deposited within volumes having radii smaller than the outer radius of the penumbra could be determined, and therefore, the amount of energy escaping the volume of interest. Energy deposition in this region was completely described by the LET of the particle, the outer radius of the penumbra based on ion energy, and the radial distance describing the volume of interest.

Using this model to compare three elements, Ne, Ar and Fe, energies were chosen such that the particles would have the same LET of 800 keV/μm in tissue. The energies required in the three cases were 4.4 MeV, 20 MeV, and 51 MeV, respectively. While the core radius of all three varied only slightly, between 1.1 and 3.7 nanometers, the outer radius of the penumbra varied between 0.6 micrometers and 27.0 micrometers. Thus, for a volume of interest having a radius of 0.5 micrometers, the energy liberated by the lowest energy ion, Ne, would be almost completely contained with the volume. Much of the energy of the higher velocity Fe, having a penumbra radius of 27.0 micrometers, would escape the 0.5 micrometer volume.

II. Radial Distribution of Dose

An alternate approach presented by Cucinotta and others also predicts the radial distribution of energy deposited in a cylindrical volume surrounding charged particle tracks, but does so with variables of energy, charge and mass of the ion.[19] Though the model determines dose to cylindrical rings with differential radii, results are easily converted to energy deposited. This model is based in part on a description of the distribution of ejected electron energies described by Rudd,[39] and in part on the method of electron transport in a medium described by Kobetich and Katz.[40] Improvements to the early work of Butts and Katz[30] were made in this model for electron range-energy relationships and stopping power values where the early work showed the greatest error.[19] Good agreement was shown with experimental results except for very large radial distances where calculations underestimated dose.[19]

Measurements

Rossi and Rosenzweig developed the first instrument designed to measure the spatial patterns of energy deposition in volumes having dimensions comparable to that described by track structure models.[41] The device was a proportional counter with a solid plastic wall defining a spherical gas filled cavity, the sensitive volume, where ionizations due to charged particle interaction were recorded. The gas cavity

was operated at a reduced pressure to simulate volumes having diameters on the order of one or a few micrometers.

The fill gas and the surrounding wall were specifically designed to have interaction properties that would approximate those of tissue and the device was known as a Tissue Equivalent Proportional Counter (TEPC). ICRU Report 30 defined tissue-equivalence as:[42]

"... a material, the absorption and scattering properties of which, for a given irradiation, simulate as nearly as possible those of a given biological material such as soft tissue, muscle, bone, or fat ..."

Since the properties of the materials chosen do not exactly match the properties of tissue, the term tissue-substitute has replaced tissue-equivalence and is defined in ICRU Report 44 as: [43]

"Any material used to simulate a particular body tissue with respect to a set of physical characteristics is called a tissue *substitute*. The set of physical characteristics chosen will depend on the application. In general, two different sets of physical characteristics are in use as criteria for the selection of a material as a substitute for a particular body issue, namely (a) the radiation interactions in the body tissue and (b) the dosimetric quantities at a point of interest in the body tissue."

Details of the operation of the TEPC are presented in Chapter IV - *Materials and Methods*.

Wall Effects

Even with the characteristics of the wall and fill gas chosen to simulate the radiological properties of tissue, the distribution of energy deposited as measured by a TEPC differ from the energy deposition patterns that would occur in a homogenous biological medium. These differences are due to the design and construction of the detector and relate most predominantly to the magnitude of electron production occurring in the rigid wall as compared to the evacuated cavity.[44] Secondary electrons are produced in much greater quantities in the wall, directly proportional to the increased density, and have sufficient range to enter the sensitive volume.[45]

In an effort to reduce these wall effects, Glass and Braby designed a TEPC without the presence of a rigid surrounding wall.[45] The sensitive volume of this wall-less counter was completely defined by the electric field existing between a spherical anode and an opposing spherical cathode, both having a radius of about 150 micrometers. The sensitive volume of the detector was defined by the use of a hemispherical guard electrode that delineated the portion of the electric field outside the volume of interest.

One year later, further designs for counters operated without the rigid wall were proposed and tested by Gross, *et. al.*[46] Several designs were presented, but the one that became the instrument used in later comparisons with the walled TEPC was the grid-wall detector. Instead of having a volume completely defined by electric field lines, the sensitive volume was contained within a spherical cathode consisting

of fine grids instead of a solid surface. The detector was not truly wall-less but the area of the grid was generally less than fifteen percent of the surface it defined.[46]

Experiments comparing the distributions of energy deposited measured by walled and grid-walled TEPCs have illustrated the effect that the wall has on the resulting spectra.[47] Fig.2.3 illustrates the differences in the measured distribution of energy deposited within walled and wall-less detectors.[36] Without the presence of a rigid wall, very low energy electrons at the outer radius of the ion track are allowed to enter the sensitive volume contributing to the sharp rise in the low energy "tail" shown in the figure. With the wall present, many low energy electrons liberated by ions with trajectories outside the volume of the detector are screened out. Due to density differences occurring at the gas-wall interface, electrons are produced just inside the wall in numbers several thousand times that of the gas cavity. These electrons enter the cavity and are recorded as a single event causing the increase in high-energy events as shown.

Other Construction Anomalies

Differences in distributions measured with a TEPC were also found when attempts were made to compare methods of calibrating the instrument.[48] On exposing the TEPC to X-ray energies less than 6.0 keV, a two peaks were observed in the spectra. One was due to the primary X-ray. The second, occurring about 2 keV less than the X-ray peak, was initially unexplained. The second peak was not

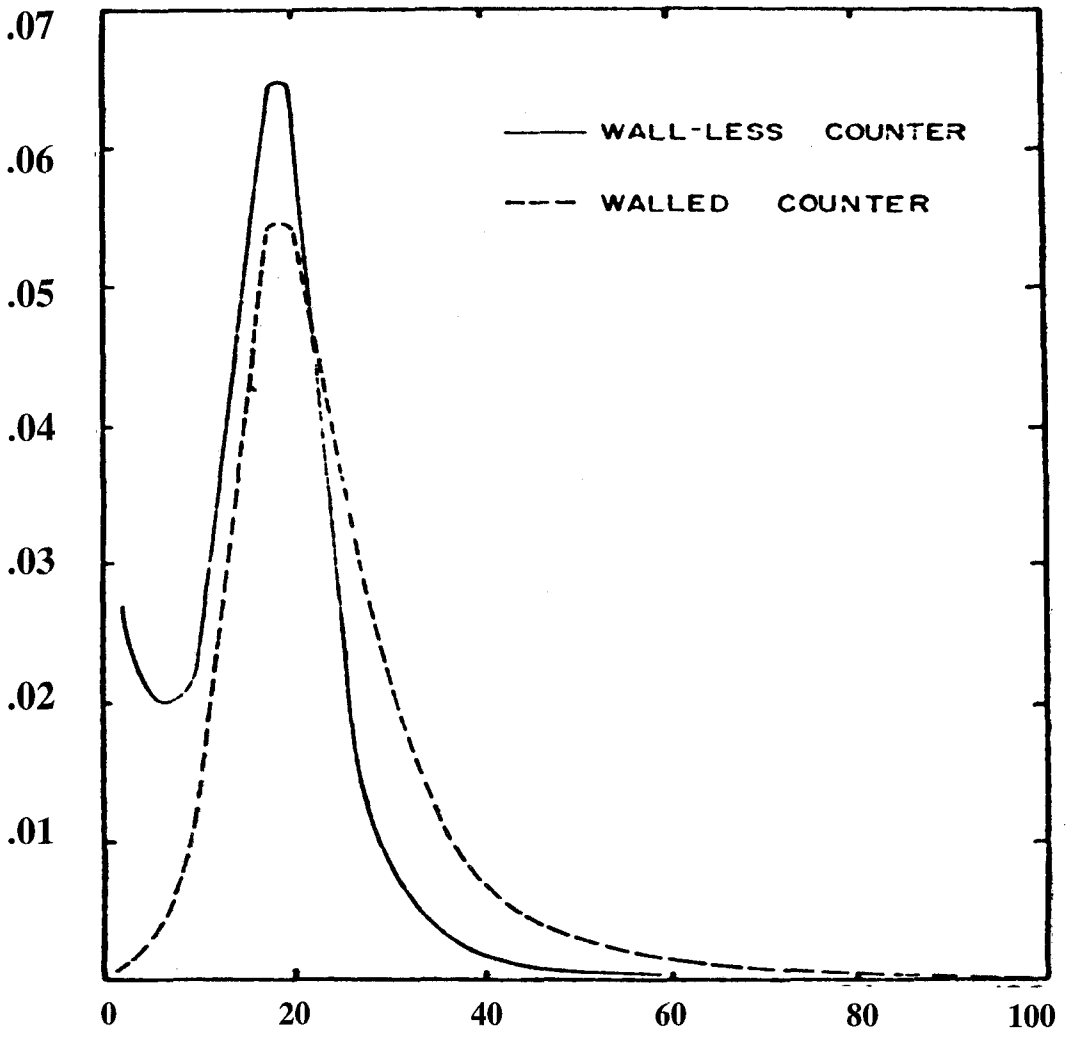

Fig. 2.3. Comparison of Measurements Made with Walled and Wall-less TEPC. Spectra were recorded on 280 MeV/nucleon nitrogen ions in the plateau region of the Bragg curve. Plot is made of the energy weighted frequency distribution, converted to lineal energy, where d(y) = y*f(y). Wall effects, due to the density difference occurring at the gas-wall interface, increase the number of high energy events. The presence of the wall also screens out many low energy events from particle passing outside the detector cavity.

observed when measurements were made using detectors constructed without the presence of a field shaping helix wire (Chapter IV). The helix wires were then disabled on the instruments having them and the secondary peak disappeared.

Though not included in that study, a secondary peak occurring at about half the energy deposition of the primary peak is also observable for calibrations using alpha-sources (Appendix B). These are believed to be due to alpha particles stopping in the central anode and helix wire. With half the path length, energy deposition is half that for particles crossing the full diameter of the TEPC cavity.

Studies Tracking Particle Location

Since the walled TEPC is used extensively in radiation protection, much of the recent experimental studies have focused on a proper interpretation of the measured energy deposition distributions, given that anomalies exist due to detector construction. Rademacher undertook a study of wall effects by incorporating the TEPC into a larger particle spectrometer.[17] The TEPC was exposed to a beam of ^{56}Fe having an energy of 1,000 MeV/nucleon. The study was unique in that energy deposition events were measured with the TEPC together with a detailed recording of the location of every particle with respect to the center of the TEPC. Having this amount of information for each event, wall effects were isolated and determined to contribute to the distribution of energy deposited in both the very low and very high

energy regions. Furthermore, high energy deposition events due to ion interaction with the anode and helix were demonstrated.

Expanding on the work of Rademacher, Gersey exposed the TEPC to ^{56}Fe having energies between 200 and 1,000 MeV/nucleon, also recording the trajectory of each charged particle.[16] This study focused on the reliability of the TEPC, when used for radiation protection purposes, given that the wall effects are clearly present and distort the measured spectra. It was concluded that event though there are artifacts in the measured energy deposition distributions, the TEPC may be used to accurately determine the average quality of the ionizing radiation, and dose equivalent, by using the second moment of the energy deposition distribution, after conversion to lineal energy.

The anomalously large energy depositions occurring at the gas-wall interface has been the subject of much debate. The source of these events have been proposed to be from either spallation, elastic scattering of the incident ion, fragmentation of the ion with neutron loss only, fragmentation of target nucleus only, or the increase in secondary electron production in the dense wall of the detector.[20] Using ion tracks generated by Monte Carlo methods, Nikjoo, et., al. simulated the response both a walled and wall-less spherical TEPC.[20] The large energy depositions shown in the measurement of ^{56}Fe was present in the simulation only for the case of the non-homogenous, walled TEPC. It was further concluded in the simulation that the anomalous energy depositions were due to an enhanced production of secondary electrons in the dense wall of the detector.

Contributions from This Work

This study was designed to further characterize the response of the walled TEPC. Precise locations and magnitudes of the distortions caused by TEPC design and construction have been determined for ^{56}Fe at 1,000 MeV/nucleon.[17] The response of the TEPC to many energies of ^{56}Fe has also been analyzed.[16] However, track structure theory and radiobiological studies show that particles with similar LET may have different energy loss properties. This study therefore focuses on the response of the TEPC to particles with different charge and velocity, choosing energies so that their LET at the sensitive volume of the detector would be similar.

Four ions were measured, ^{14}N, ^{16}O, ^{20}Ne, and ^{28}Si, at the Heavy Ion Medical Accelerator (HIMAC) in Chiba, Japan. The choice of ion was somewhat restricted by the combination of charge and energy easily deliverable at the facility, but all ions had an LET that was within a few percent of a mean value of 43.5 keV/μm at the gas cavity of the TEPC. The simulated volume of the TEPC was smaller than the volume of energy deposition surrounding the incident ions. Track structure calculations, however, predicted a different magnitude of energy escaping the TEPC volume, based on the velocity of the incident ion, even though the LET in each case was similar. Since LET is currently used to determine radiation quality, this study focuses on whether the TEPC may still be used for radiation protection purposes given that, along with anomalies in the measured spectra due to design and construction, there are also differences in track structure leading to possible differences in the measurement for particles with similar LET.

CHAPTER III - MICRODOSIMETRIC TERMS AND QUANTITIES

Analysis of energy deposition in very small sites differs substantially from the methods commonly employed in radiation protection. The usual definitions of absorbed dose and dose equivalent do not provide a complete description of energy deposition characteristics. They are averaged values more relevant to volumes much larger than those studied in microdosimetry. The focus of microdosimetry, on the other hand, is not the average energy absorbed per unit mass of tissue, but more precisely the nature of the energy deposition by single or relatively few incident ions. As the volume of the target to be studied becomes increasingly smaller, the stochastic nature of radiation interaction becomes increasingly important.

Specific Energy

For the purposes of microdosimetry, interest is focused on volumes that have an energy-deposition event. The energy deposited in the volume by a particle, together with all of the secondary electrons produced by it, is called the energy

imparted. This is denoted by the symbol ε. Much like dose, D, the specific energy, z, is defined as the quotient of the total energy imparted, ε, by the mass of the microdosimetric volume of interest, m, or: [34]

$$z = \varepsilon/m \qquad \text{Equation 3.1}$$

As the stochastic analogue of dose, z is proportional to the total energy imparted during an irradiation.[34] Thus, like dose, z is usually expressed in units of Gy.

As z is a probability distribution, it may have a zero value at any specific time, or it may obtain many orders of magnitude greater than its counterpart, D. When averaging over a large number of individual targets, such as cells in tissue, all values of z may occur. Volumes with no energy deposition are averaged with those having higher values and the mean value becomes equal to the average dose. In other words, the mean value, $\bar{z}$, of the probability distribution f(z) is equal to absorbed dose, D.[34] Any statements of z, and its frequency distribution f(z), must therefore contain information on the size of the volume irradiated.[34]

Lineal Energy

Another quantity used is the lineal energy, y, and is related to the non-stochastic concept of restricted Linear Energy Transfer, L_Δ. LET is defined as the mean energy, dE, lost in electronic collision by a charged particle traversing a

distance dx.[6] The restricted LET excludes energies of delta radiation greater than a cut-off value, Δ. The lineal energy, on the other hand, is defined as the quotient of energy imparted, ε, by the mean chord length, $\bar{l}$, of the volume traversed by a single charged particle, or:[4,34,49,50]

$$y = \varepsilon/\bar{l} \qquad \text{Equation 3.2}$$

Thus, y is not restricted by an energy limitation but rather a geometric cut-off based on the size of the volume studied. Similar to z, y is subject to a probability density distribution, f(y), whose mean value, $\bar{y}$, carries a specific meaning. It is the frequency mean specific energy and is denoted $\bar{y}_f$. Unlike z, however, y refers only to the energy imparted in a single event and is usually expressed in terms of keV/μm.

When analyzing microdosimetric spectra in terms of lineal energy, the geometry of the detector must be known in order to find the mean chord length, $\bar{l}$. For any convex body, having surface area S and volume V, exposed isotropically to particles originating outside the volume, the mean chord length, $\bar{l}$, may be found generally by Cauchy's Theorem (Cauchy 1908):[4,34,49]

$$\bar{l} = 4V/S \qquad \text{Equation 3.3}$$

For spherical volumes, the mean chord length is two-thirds the diameter of the site or:

$\bar{l} = 2d/3$ Equation 3.4

Energy imparted, ε, in the definition of y is due to the passage of a single charged particle. In the definition of z, ε refers to the energy imparted by the passage of any number of particles. In order to relate the two quantities, a distinction must be made between the single event and multiple event z distributions. Since the passage of charged particles through the detector are statistically independent, measurement of the single event spectra translates directly to a distribution as a function of lineal energy, f(y), as well as the single event z distribution, $f_1(z)$. The relationship between $f_1(z)$ and f(y) is dependent on the size of the volume irradiated by the following:[34]

$$z = \frac{4y}{\rho S}$$ Equation 3.5

where:

y = energy imparted converted to lineal energy (keV/μm),
ρ = density of tissue (g/cm^3), and
S = surface area of the volume irradiated (μm^2).

The density, ρ, is usually taken as that of tissue, 1 g/cm^3. Since y is expressed in keV/μm and the simulated diameter of the detector is in μm, substituting the surface area of a sphere ($S=4\pi r^2$), and making the conversion to Gy, the relation becomes:

$$z = \frac{0.204y}{(2r)^2} \text{ Gy} \qquad \text{Equation 3.6}$$

Analysis of Spectral Information

The energy deposition distribution observed by measurement is proportional to y and z and is dependent on the stochastic nature of energy deposition events, as well as the modification of the distribution by the measuring system.[34] It is, therefore, determined by a number of random factors. Six independent processes, each of which is subject to statistical fluctuations, are involved in shaping the measured spectra.[49] These are:

1. The distribution of the number of energy deposition events,
2. The LET distribution of the particles,
3. The distribution of the path lengths of particles in the site,
4. The distribution of the number of collisions,
5. The distribution of energy imparted in individual collisions,
6. The distribution of the fraction of this energy retained in the site.

For a full discussion of the relation and interaction of these processes see the section on Microdosimetry by Kellerer in *The Dosimetry of Ionizing Radiation.* [49]

The total variance of the spectra is based on the sum of the variances of these individual processes. For extremely small sites, where the change in LET may be neglected, the predominant effect shaping the distribution is energy loss straggling.[49,59] This is shown graphically in Fig.3.1 where the effects of changes in

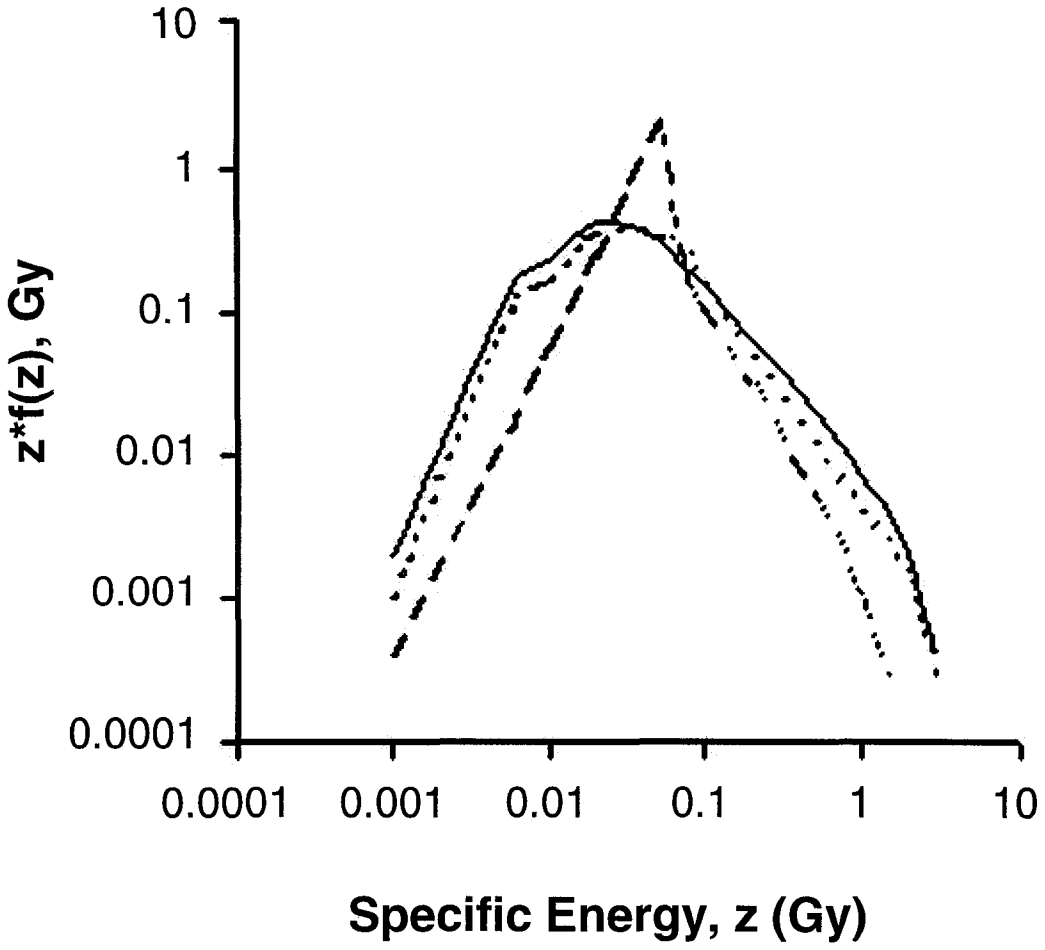

Fig. 3.1. Calculated Effects of Straggling and Variation in LET on Energy Deposition. Solid line is an energy deposition spectra of ^{60}Co, converted to specific energy. Dashed line shows the effects of including only changes in LET in a simulation of energy deposition in a microscopic volume. Dotted line, matching closely with the measured distribution, shows the effects of including only energy loss straggling in predicting the distribution.

LET and the effects of straggling compared to a ^{60}Co energy deposition spectra, converted to specific energy (Chapter III). Including only straggling closely matches the overall energy deposition distribution for ^{60}Co whereas variations in LET alone do not.

Determination of the variance is found by straightforward statistical methods. The mean, μ, of any distribution, f(y), is defined as the first moment about the origin and is the expected value of y, or E[y]. The second moment about the origin is the expected value of the square of y, or $E[y^2]$. The second moment about the mean is the variance in y, denoted σ^2, and is defined as the expected value of the squared deviations from the mean, or $E[(y-\mu)^2]$. [51]

In microdosimetric studies, the first moment of the lineal energy distribution is called the frequency mean lineal energy and is denoted $\bar{y}_f$.[34] It is an estimate of the expected value of y about the origin, $\hat{u}$, or:

$$\bar{y}_f = E[y] = \sum y \cdot f(y) \qquad \text{Equation 3.7}$$

The dose mean lineal energy, $\bar{y}_d$, is the second moment about the origin divided by the first, or:[34]

$$\bar{y}_d = \frac{E[y^2]}{E[y]} = \frac{\sum y^2 f(y)}{\bar{y}_f} \qquad \text{Equation 3.8}$$

By the distributive property of expected values, the variance of the distribution, $E[(y-\mu)^2]$, is numerically equal to the expected value of the square of y, $E[y^2]$, minus the square of the expected value of y, $(E[y])^2$, or:[51]

$$Var(y) = E[(y-\mu)^2] = E[y^2] - (E[y])^2 \qquad \text{Equation 3.9}$$

From Equation 3.7, the estimate of the expected value of y is $\bar{y}_f$, and from Equation 3.8, the estimate of the expected value of y^2 is the product of $\bar{y}_f$ and $\bar{y}_d$. The variance of the distribution becomes:

$$Var(y) = \bar{y}_f \bar{y}_d - (\bar{y}_f)^2 = \bar{y}_f(\bar{y}_d - \bar{y}_f) \qquad \text{Equation 3.10}$$

Thus the standard deviation, σ, which is the square-root of the variance, is therefore:

$$\sigma = \sqrt{var(y)} = \sqrt{\bar{y}_f(\bar{y}_d - \bar{y}_f)} \qquad \text{Equation 3.11}$$

The relative variance of a distribution, V_R, is the quotient of the variance by the square of the mean. This is equivalent to the square of the coefficient of variation.[51] It is a unitless measure of the width of a distribution relative to its mean value.

$$V_R = \frac{\sigma^2}{\mu^2} = \frac{E[y^2] - (E[y])^2}{(E[y])^2} \qquad \text{Equation 3.12}$$

Which is numerically equal to the ratio of the dose mean lineal energy to the frequency mean lineal energy, minus one:

$$V_R = \frac{\bar{y}_d}{\bar{y}_f} - 1 \qquad \text{Equation 3.13}$$

An equivalent analysis is had for the moments of the single event specific energy distribution, $f_1(z)$.

CHAPTER IV - MATERIALS AND METHODS

Four ions were measured, ^{14}N, ^{16}O, ^{20}Ne and ^{28}Si, at the Heavy Ion Medical Accelerator (HIMAC) in Chiba, Japan. The HIMAC accelerator facility was constructed by the National Institute of Radiological Sciences (NIRS) for cancer research and treatment in 1993.[52] By June 1994 treatments using carbon beams had begun and by August 1999 over 600 patients has been treated.[28] The HIMAC facility is capable of delivering a wide range of ions, from protons to iron, with energies ranging from 100 to over 1,000 MeV/nucleon. It is therefore an excellent choice for experiments designed not only to study ions used in tumor therapy and cancer treatment, but also primary ions making up the spectrum of particles in the galactic environment.

The choice of ion measured in this study was somewhat restricted by the combination of charge and energy easily deliverable at the facility, but all ions had an LET that was within a few percent of a mean value of 43.5 keV/μm at the gas cavity of the TEPC. The beam energies of the ions required to give this LET were 100, 165, 230 and 800 MeV/nucleon, for ^{14}N, ^{16}O, ^{20}Ne and ^{28}Si, respectively.

The Tissue-Equivalent Proportional Counter

The choice of using a proportional counter to determine energy deposition in a wide variety of situations is due to its versatility as a radiation detection instrument.[9] Its main characteristic is the ability to distinguish events based on the amount of energy deposited within the detector, unlike Geiger-Mueller tubes which simply record the occurrence of an event without conveying any information on energy deposited.[9,15] Ionizations in the proportional counter are amplified above system noise by a factor related to the anode potential. This multiplication of primary events also allows operation in situations where the number of ion pairs generated would be too small to permit use of ion chambers.[15]

I. Electric Field Within the Detector

Amplification of the ionization from an initiating event is dependent on many factors, but is generally a result of increasing the electric field within the detector to a sufficiently high value to generate secondary ionizations when free electrons undergo collisions with the neutral fill-gas.[15] When the electrons liberated by an ionizing event are accelerated in the applied electric field to energies greater than the ionization energy of the fill-gas, an avalanche of secondary ions is produced by the free electron collisions with gas molecules. Under proper conditions the number of

electrons in the avalanche is proportional to the number of primary electrons created by the incident ion.

For a cylindrical geometry, The electric field strength within the detector at some point, r, radially away from the anode is dependent on anode wire diameter, size of detector and applied voltage[15] and is given by the relation:

$$E(r) = \frac{V}{r \cdot \ln(b/a)} \qquad \text{Equation 4.1}$$

where: V = voltage applied between the anode and cathode,
r = radial distance from the anode wire (meters),
a = anode wire radius (cm), and
b = cathode inner radius (cm).

Typical gases at atmospheric pressure require field strengths on the order of $1x10^6$ V/m to produce the avalanche of secondary electrons.[15] The detector used in these experiments has a 1.27 centimeter diameter and a 0.046 millimeter central anode. An applied voltage of 600 V results in the electric field being $4.64x10^6$ V/m at the surface of the anode. At this point, where r is at its minimum, the electric field strength is at its largest but drops off with increasing r to a point where the avalanche cannot be maintained.

II. Multiplication Factor

For uniform multiplication to occur for all ion pairs formed by the original event, if proportionality is to be achieved, the region of multiplication must be confined to a very small volume around the anode as compared with the volume of the detector. Since the original ion pairs may be formed at any point within the detector volume, requiring multiplication only in the region very near the anode ensures the same multiplication for almost all original ions. The charge collected by the anode is then proportional to the energy of the primary ionization regardless of the location of the originating event.

Gas multiplication within a detector may be predicted based on physical detector parameters and applied voltage. Diethorn derived an expression for calculating the multiplication factor, M, assuming cylindrical geometry.[15]

$$\ln(M) = \frac{V}{\ln(b/a)} \cdot \frac{\ln(2)}{\Delta V} \cdot \left[\ln\left(\frac{V}{p \cdot a \cdot \ln(b/a)} \right) - \ln(K) \right] \qquad \text{Equation 4.2}$$

where: M - gas multiplication factor;
V - applied voltage (V);
ΔV - potential difference through which an electron moves between successive ionizing events (V);
a - anode radius (cm);
b - cathode radius (cm);
p - gas pressure (atm); and
K - value, E(r)/p, below which multiplication cannot occur (V/cm-atm).

Both ΔV and K are constants for a specific fill-gas. Using pure propane, ΔV and K have the values of 29.5 V and $1x10^5$ V/cm-atm, respectively (Knoll, table 6-1). Multiplication factors are given in Table-4.1 for various gas pressures applying a 600V bias.

TABLE-4.1

Gain vs. Pressure for a 1.27 cm Diameter Proportional Counter Applying a Bias of 600 Volts

Gas Pressure (atmosphere)	Multiplication Factor - M
0.2	8
0.1	47
0.05	267
0.025	1521

As can be seen, larger pressures within the detector result in a reduction in amplification of the primary ion. To increase the multiplication factor within a detector operated at a fixed pressure, detector bias must be increased. If the applied voltage becomes too large electrical breakdown occurs, therefore a balance must be found between the desired operational pressure and the multiplication achievable.

For commonly used proportional counters having a spherical geometry, the electric field is not uniform at all points radially away from the anode as discussed above for the case of cylindrical geometry. The spherical detector must be modified to achieve uniform multiplication of the originating event. This is accomplished by

the addition of a helical wire surrounding the anode, as shown in Fig.4.1. A potential is applied to the helix that exists naturally at that radius based on the anode potential and the diameter of the sphere.

Though the distance between the anode and cathode is variable, an equal distance is maintained between the anode and helix, thereby maintaining a uniform electric field in the region of multiplication.[5,34] Uniform multiplication along the entire length of the anode is established.

III. Approximating Energy Deposition in Cellular Volumes

Once it is assured that the detector is operating as a true proportional counter, it is important to be able to relate the energy deposition occurring in the detector to energy deposition in a target of interest, such as a single cell. The energy deposited in any site is the product of the mass stopping power of the target material, the target density and the path-length of the ionizing radiation across its volume,[9] or:

$$E = \left(\frac{dE}{\rho dx} \right) \cdot \rho \Delta x \qquad \text{Equation 4.3}$$

where: E - Local energy deposition (MeV);
$dE/\rho dx$ - mass stopping power of the particle in the medium ($MeV\text{-}cm^2/g$);
ρ - target density (g/cm^3); and
Δx - path-length across target volume (cm).

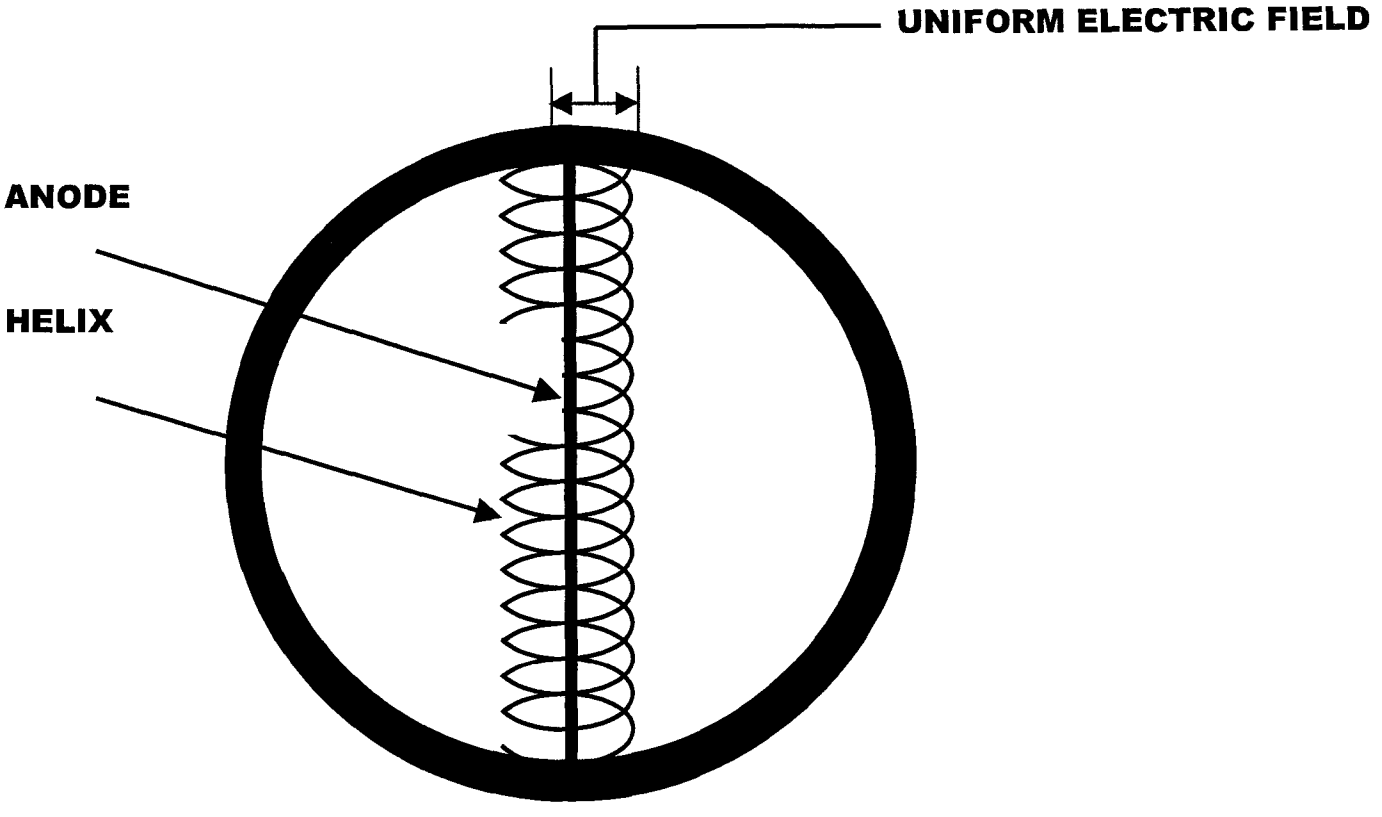

Fig. 4.1. Representation of helix wire surrounding anode used to create a uniform electric field along the length of the anode wire.

In order to simulate a site of biological interest, the energy deposition in the detector gas is set equal to that of the tissue volume:

$$E_g = E_t \qquad \text{Equation 4.4}$$

Where E_g refers to the energy deposition in the gas volume and E_t refers to the energy deposition in a volume of tissue. Thus, we have:

$$E_g = \left(\frac{dE}{\rho dx}\right)_g \cdot \rho_g \Delta x_g = \left(\frac{dE}{\rho dx}\right)_t \cdot \rho_t \Delta x_t = E_t \qquad \text{Equation 4.5}$$

By choosing a fill gas with a proper atomic composition so that the interaction properties are similar to those of tissue, the ratio of the mass stopping power of the gas to the mass stopping power of tissue will approach unity. A gas having this composition is said to be tissue-equivalent, and the mass stopping power term is removed from Equation 4.5. The expression reduces to:

$$\rho_g \Delta x_g = \rho_t \Delta x_t \qquad \text{Equation 4.6}$$

Under conditions of Tissue-Equivalence, the diameter of the site of interest and its associated density form the conjugate pair of equal effective dimensions.[34,53] Since the physical size of the detector and the density of the tissue of interest are known, target size may be approximated by adjusting gas density within the detector, or;

$$\rho_g = \rho_t \frac{\Delta x_t}{\Delta x_g}$$ Equation 4.7

The gas density, which is a function of gas pressure, becomes the only variable in the simulation of microscopic tissue volumes on the order of $1x10^{-18}$ cubic meters. The spatial patterns of energy deposition within the sensitive volume of the detector then become proportional to those that would occur in similarly small biological sites.[53,54] When using a fill-gas that is not exactly tissue equivalent, the true mass stopping powers should be utilized in Equation 4.5 above to achieve a closer approximation.

IV. Experimental Settings

The density of tissue used in microdosimetric studies is generally taken to be 1.0 gram per cubic centimeter.[34] By Equation 4.7, simulation of a one micrometer diameter sphere of tissue using a 1.27 diameter spherical proportional counter requires a gas density, ρ_g, of 0.0787 milligrams per cubic centimeter. Propane based Tissue-Equivalent gas is commonly used as a fill-gas and has a density of 1.826 milligrams per cubic centimeter at standard temperature and pressure.[55] The quotient of the required gas density by the standard density of tissue-equivalent propane gives the pressure reduction factor required to simulate a 1 μm site, or, in this case:

$$\frac{\rho_g}{\rho_{TE\text{-}gas}} = \frac{0.0787}{1.826} = 0.0431 \qquad \text{Equation 4.8}$$

Multiplying standard pressure, 760 Torr, by this factor gives the operational pressure of 32.7 Torr.

TABLE-4.2

Pressure Required for Site Size Simulation Using a 1.27 cm Spherical Tissue Equivalent Proportional Counter

Required Pressure (Torr)	Simulated Site Diameter (μm)
98.4	3.0
65.6	2.0
32.8	1.0
16.4	0.5

Table-5.2 lists the pressures required in simulating tissue volumes commonly used in microdosimetric studies. For this study, all experiments were conducted using the same spherical proportional counter[56] simulating a 1 μm diameter. As well as using a fill gas that is tissue-equivalent, the surrounding spherical wall of this detector was made of tissue-equivalent plastic.[57] This was the identical instrument used in previous studies of ^{56}Fe.[16,17]

Calibration of the instrument was performed using an internally mounted ^{244}Cm alpha source. (see Appendix B) With the detector in its operational position a gravity controlled shutter blocked the alpha particles from entering the gas cavity.[56] When mounted in an inverted position, the shutter opens and alpha particles traverse the diameter of the cavity. After verifying with a research pulser that the pulse-height analyzer was responding linearly (response proportional to the size of the energy deposition event), the location of the energy deposited by the alpha particle with known LET, 84.15 keV/μm, was determined. Since the alpha particles traversed the diameter of the detector, the 1.0 μm path length provided a conversion from channel number to energy deposition.

Data Acquisition

The TEPC was part of a larger particle detection system. Since energetic charged particles undergo both Coulomb multiple scattering and nuclear collisions,[58,59] the location and charge of each individual ion was recorded at several points along the beam-line. This detailed information facilitated not only the elimination of any unwanted events, but also allowed analysis of energy deposition based on the trajectory of the particle through the TEPC.

I. Particle Identification and Tracking

Identification of charged particles and determination of their position is a well established concept.[58,60-63] Knowing the precise location of each particle causing an energy deposition event in the TEPC has led to a better understanding of the information returned by the detector.[16,17,61] Event coordinates were recorded at several locations along the ion trajectories with four pairs of Position Sensitive Detectors (PSDs) mounted along the beam axis as shown in Fig.4.2. Two pairs were mounted between the beam exit and the TEPC and two pairs were mounted downstream of the detector. Numbering of the PSD groups began with the pair closest to the exit window of the beam, PSD1, ending with PSD4 furthest downstream.

Each PSD pair consisted of two circular lithium-drifted silicon detectors having a diameter of 40 millimeters and a thickness of 800 μm to 1050 μm. The total charge, Q, collected on the conducting rear face of the detector was proportional to the energy lost by the ion in the silicon.[60] Since any fragments created along the beam-line had velocities very near that of the incident ion, the energy loss signal, ΔE, was also proportional to the square of the charge, Z, of the particle that traversed the detector.[58,62] The resolution of this signal was sufficient to identify different ions and select only those events of interest, the primary beam species, in later off-line analysis.[63]

An additional silicon detector, labeled 3mm in Fig.4.2, was mounted between PSD3 and PSD4. This detector had a thickness of 3.0 mm and a radius of 1.0 cm and

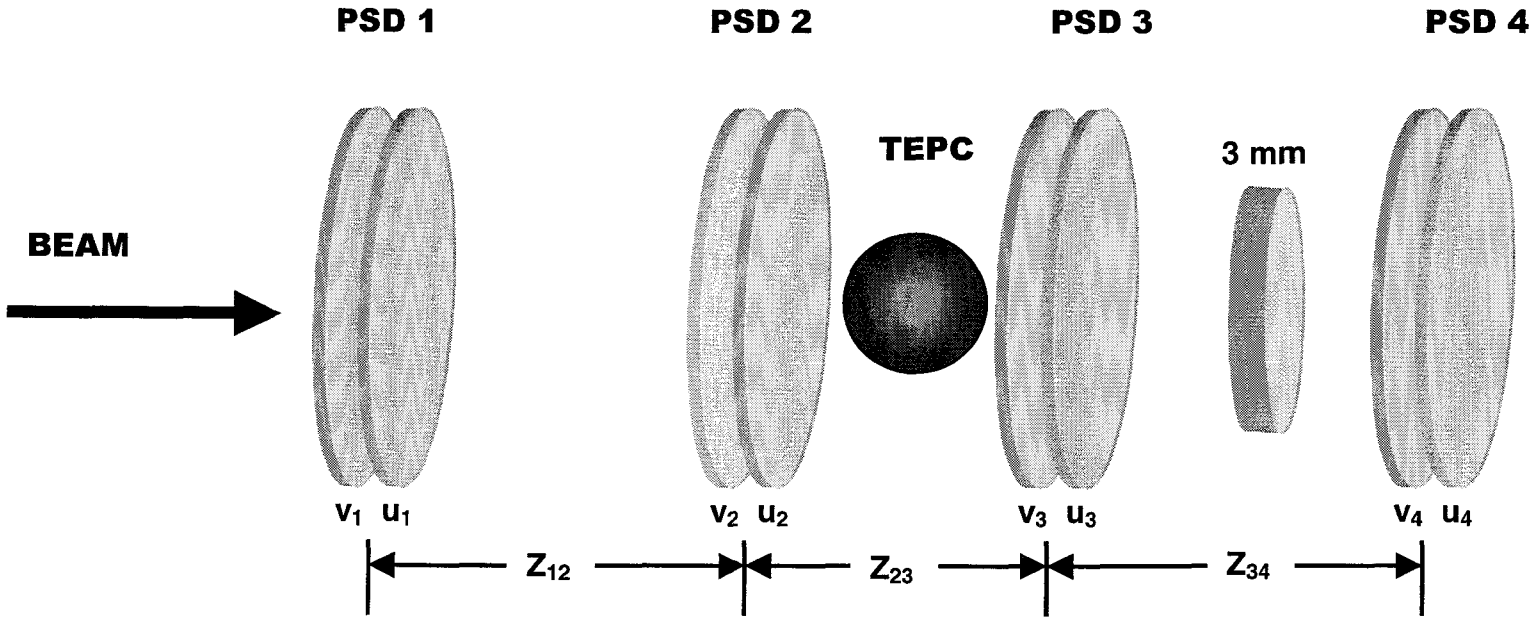

Fig. 4.2. Layout of the particle tracking system showing the location of the position sensitive detectors, TEPC and the 3 mm trigger relative to the beam direction. Silicon detectors labeled u in each PSD group measured the horizontal position of the particle trajectory. Those labeled v measured the vertical. The vertical detector of each group was upstream of the horizontal. The distance between PSD groups, Z_{ij}, represented the third coordinate of the particle trajectories.

was used to increase the efficiency of triggering. Since the radius of the 3mm detector was smaller than the PSD's, incident ions that were well outside the detection capability of the TEPC were not processed in the logic pathway. Events could therefore be recorded by the TEPC, when it was not included in the trigger coincidence, without increasing system dead time.

The front face of each silicon detector was formed by lithium diffusion and operated as a resistive divider. The charge collected on this face was divided between two opposing leads in proportion to the location of the particle that passed between them. The sum of these two charges, q_1 and q_2, was approximately equal in magnitude to the total charge, Q collected on the exit face. Their difference, normalized by the sum, was proportional to the location, L, that the particle passed between the two leads, and is given by the following relation:[60]

$$L(q_1, q_2) = r \cdot \sin\left(\frac{\pi}{2}\frac{(q_1 - q_2)}{(q_1 + q_2)}\right) \qquad \text{Equation 4.9}$$

where:

$L(q_1,q_2)$ = location of the particle between the collecting leads (mm),
r = radius of the silicon detector (mm),
q_1, q_2 = divided charge collected at each of two opposing leads, and

The upstream detector of each PSD group was mounted to record the vertical dimension of the plane perpendicular to beam. The second detector was identical to the first but rotated about 90° to give information on the orthogonal dimension. Since there were errors associated with detector resolution, the coordinates measured were

later transformed into the laboratory coordinate system, x and y, as discussed below. The third dimension, z, is the nominal axis along which beam particles travel.

II. Correction of Particle Location

In theory, information returned by the PDSs should be directly correlated with the position that the particle traversed the detector. In practice, however, non-uniformity in the resistive layer of the silicon, and inefficiencies in charge collection, caused distortions in the values returned.[60,61] The errors were greatest for particles furthest from the center of the detector. The coordinates recorded by the PSDs were referred to using the notation (u,v). Using non-linear regression techniques,[60,64] these coordinates were mapped to the laboratory coordinate system (x, y) by the following:

$$x_i = X(u_i,v_i) = A + Bu_i + Cv_i + Du_i^2 + Ev_i^2 + Fu_iv_i \ ;$$
$$y_i = Y(u_i,v_i) = G + Hu_i + Iv_i + Ju_i^2 + Kv_i^2 + Lu_iv_i \qquad \text{Equation 4.10}$$

To find coefficients A through L of Equation 4.10, specific information on u, v, x and y was required. Since the incident ion had all possible u and v coordinates when recorded, a specially designed collimator was used to screen out all particles except those having precisely known locations. The collimator was made from a brass slab 2.54 cm thick with 0.8 mm holes drilled at 6 mm distances radially around

the center, as shown in Fig.4.3. During the experiment, the masking-collimator was mounted directly upstream of each PSD group to record its response.

The coordinates returned by the PSD after masking were then compared to the known coordinates of the mask, x and y. Multiple regression was performed in off-line analysis to return the recorded positions to their true vales.[16] Fig.4.4a depicts the positions as recorded during the masking run for an incident beam of silicon at 800 MeV/nucleon. Fig.4.4b shows the improvement of the particle locations after the transformation. Comparing the size of the locations with the known size of the holes the absolute resolution of the PSDs was determined to be 0.2 mm.

III. Recreation of Ion Trajectories

After all PSD coordinates were transformed into the laboratory coordinate system, each PSD was aligned with the beam axis. All of the x and y coordinates were adjusted so that the center of the beam in each PSD occurred at the point (0,0). The center of the TEPC was defined as point (x_0, y_0, z_0), and the coordinates of each particle were re-defined with respect to the plane perpendicular to the beam axis at the center of the TEPC, point z_0. Further details are given in the *Data Preparation* section below.

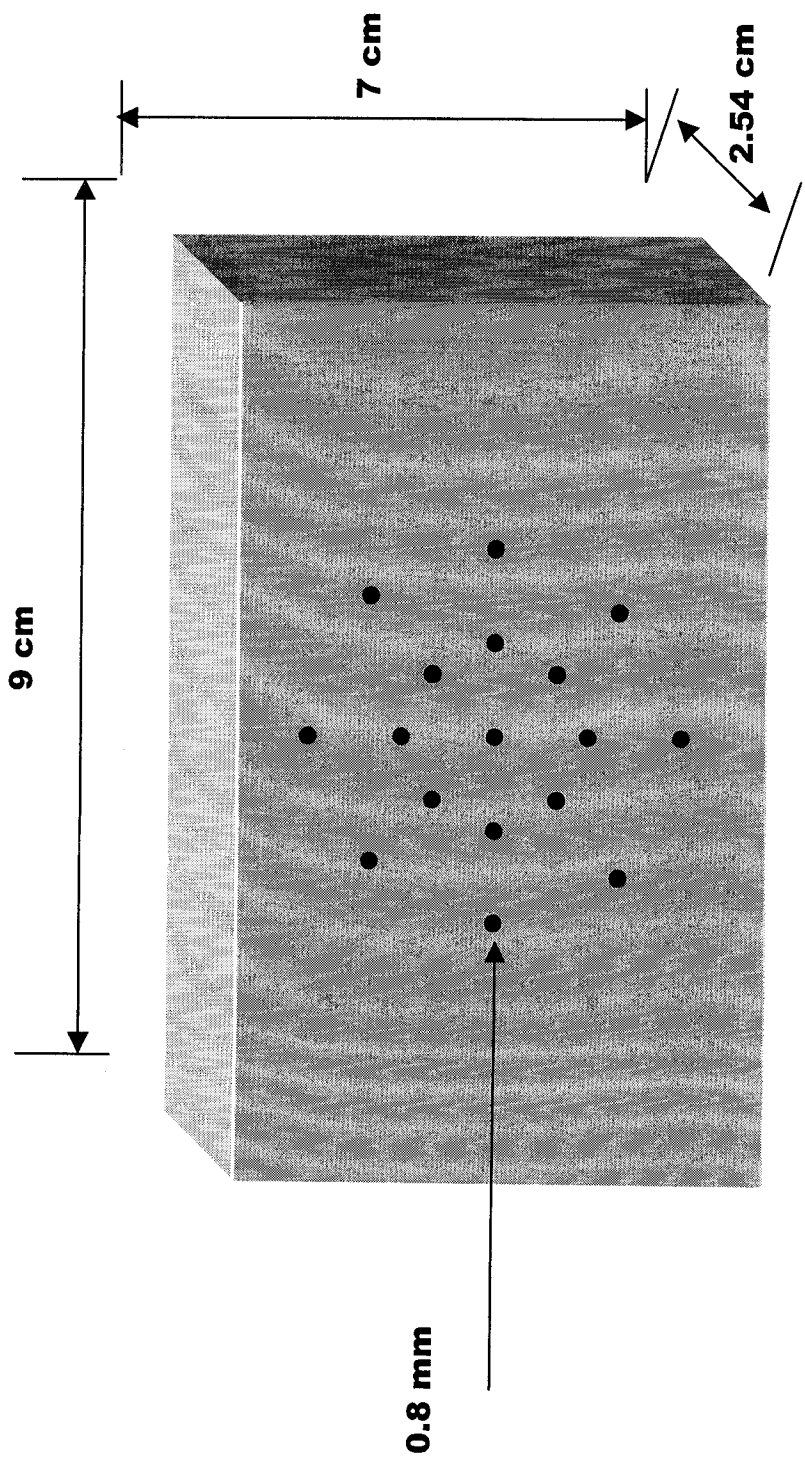

Fig. 4.3. Multi-holed collimator used to transform u,v coordinate system recorded by the PSDs into true X, Y coordinates.

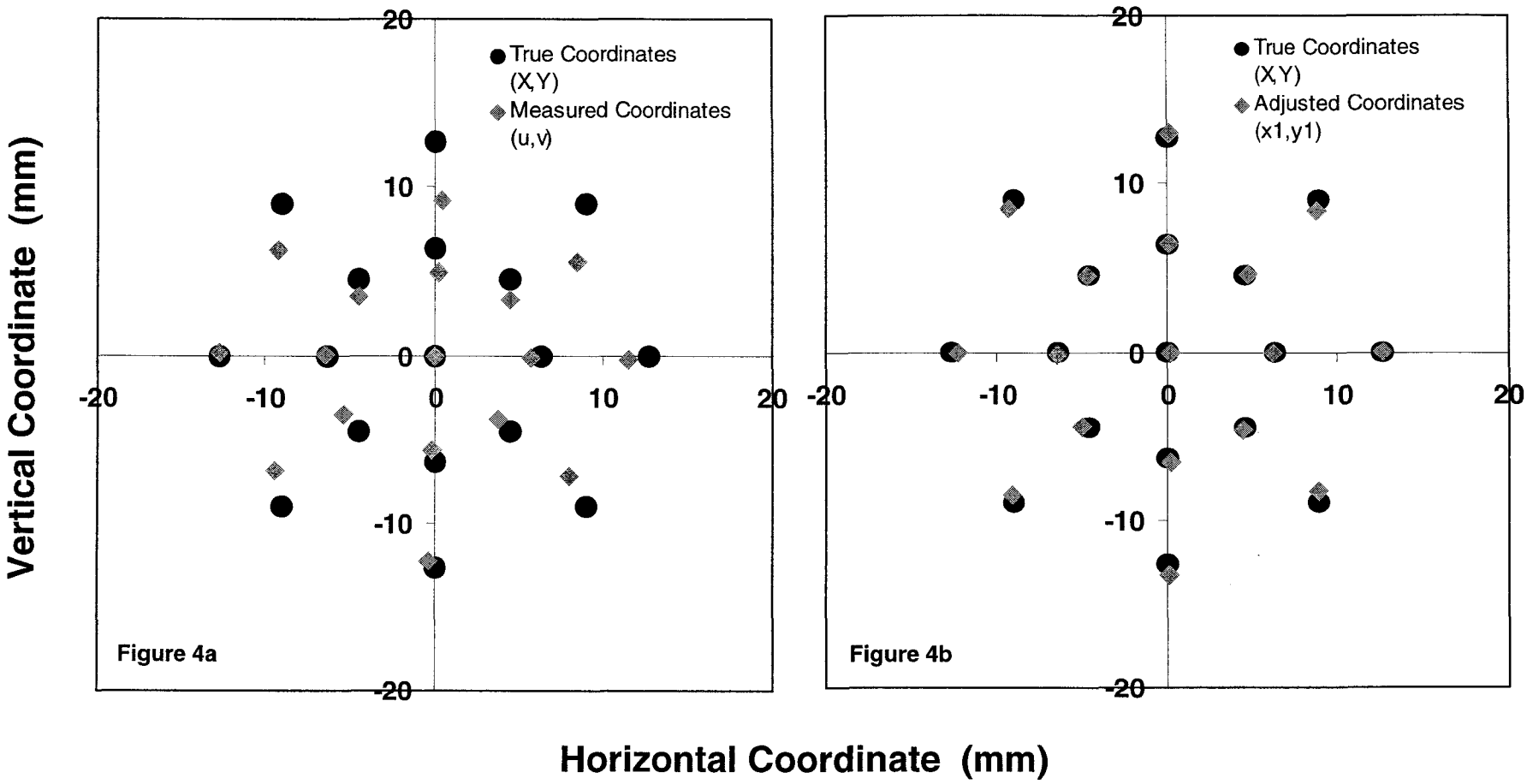

Fig. 4.4. Measured Coordinates and Corrected Locations. Scatter plots showing the results of mapping measured coordinates (u,v) into laboratory coordinate system (x,y). 4a compares the measured locations of mask holes (u,v) to the known values of the collimator positions (X,Y). 4b shows the measured values after the transformation has been applied (x1,y1).

IV. Electronics and Triggering

Each of the three signals from a single PSD was sent to an individual charge sensitive pre-amplifier, shaping amplifier, and then to a CAMAC-based ORTEC[65] analog-to-digital converter (ADC). The four PSD groups, each consisting of two silicon detectors having three signals each, therefore required a total of 24 ADC channels for processing. The digitized signals were then stored on disk, as were the other signals described below.

The signal from the TEPC was attached to an external EG&G ORTEC 142AH charge sensitive preamplifier. Preamplifier output was split and sent into two EG&G ORTEC 572 shaping amplifiers. Each amplifier was set to a different gain to record detailed information on both low and high-energy deposition events. The unipolar output signals from each these amplifiers were also split. One branch was sent into individual ADC channels of the primary data acquisition system while the other was routed to stand-alone MCAs. The shaped signals from the low and high gain amplifiers accounted for two more ADC channels.

One 3mm thick lithium-drifted silicon detector was placed between PSD3 and PSD4 (Fig.4.2). Since the radius of this detector was smaller than the radius of the PSD's, the efficiency of triggering data acquisition was improved when the TEPC was not included in the coincidence logic. This eliminated processing of particles that were well outside the detection capability of the TEPC, but still provided an adequate ratio of events with and without a corresponding signal in the TEPC. The signal from

this silicon detector, recording only dE, required only one ADC channel after pre-amplification, shaping and amplification.

The fast timing output from the pre-amplifiers connected to the TEPC and the 3mm trigger detector were used in the timing pathway as shown in Fig.4.5. A trigger was defined in one of two modes. The first mode used only the 3mm detector and included information on particles that did not cause a signal in the TEPC. The second mode included the TEPC in coincidence with the 3mm detector and recorded information only for incident ions producing a signal in the TEPC.

A valid coincidence between the TEPC and silicon trigger detector required that both of the signals arrive above a predefined threshold. These threshold levels were set and controlled individually for each of the fast timing signals by use of discriminators. Each discriminator created a logic pulse when the input signal was above the threshold. Only when the logic pulses from both discriminators arrived at the first coincidence unit within the proper time was the trigger pathway allowed to continue. This was logged as a valid 'event' and caused the gate generator to change into its 'busy' state.

Having a valid event, the logic signal continued along the pathway and was split. One branch was sent directly into a second coincidence detector. The second was sent through a gate monitoring the status of the data acquisition system before arriving at the second coincidence unit. If the gate generator was in a busy state the event was rejected, adding to system dead time. Scalars recording total events and event + busy were incremented. The width of the "busy" gate was set to allow a full

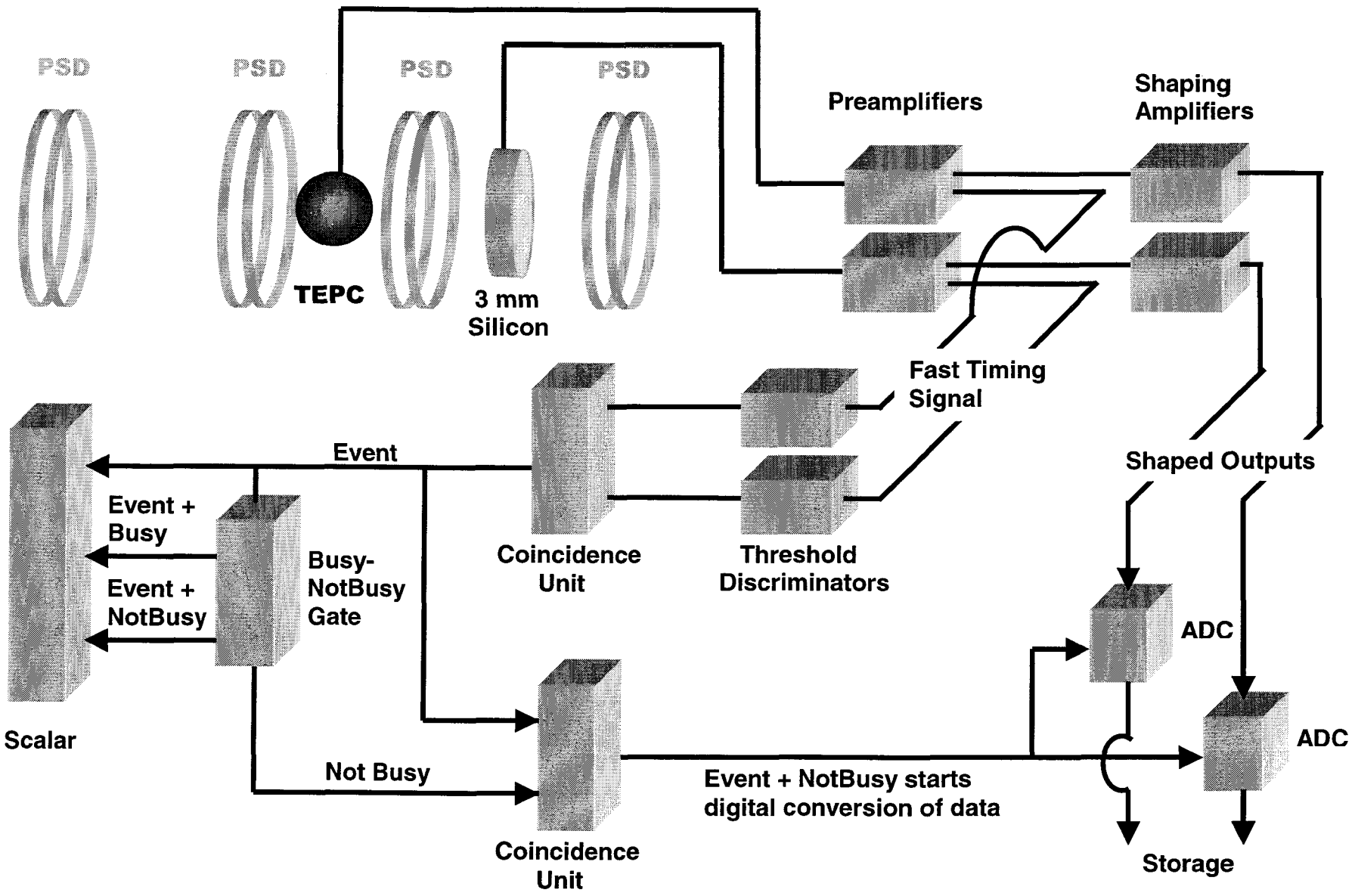

Fig. 4.5. Logic pathway for triggering data acquisition. Fast timing outputs are used for the logic pathway eventually arriving at the Analog to Digital Converter (ADC). Shaped outputs are sent directly to the ADC waiting for the state "Event + NotBusy" to trigger data conversion. If "Event + Busy" is found only the scalars are incremented.

processing of one event before another trigger could be accepted. This width was typically 150 microseconds.

If the gating unit was in a not-busy state, the second coincidence unit allowed the signal to continue through the pathway, arriving at the CAMAC controller. In this case the scalars recording total events and event + not-busy were incremented. An event + not-busy coincidence sent a request to the ADC's to begin conversion of all shaped output signals from analog to digital format. Conversion of all data channels required approximately 80-100 μs and accounted for most of the system dead time.[61] Additional time (2 μs per channel) was allowed for the transfer of data from the ADC's to the local storage within the CAMAC crate, provided by the Hytec 1341 List Processor.[66]

Once the data from all channels had been converted, the list processor buffered the data from each channel and reset the ADCs. The gate generator was then returned to the not-busy state to trigger the processing of the next available trigger signal. With data conversion taking approximately 80 μs and reading out of the converted data taking another 60 μs, overall system dead time was on the order of 150 μs per valid event. This equates with a maximum possible data acquisition rate of about 5,000 events per second. Due to the structure of the beam and the characteristics of the positional detectors, this rate was not achievable.

Particles were extracted from the accelerator and delivered to the detector system in pulses referred to as spills. Each spill lasted approximately one second and came in three and a half second intervals, for about 18 spills per minute. Between spills there was no incident particle to record allowing the acquisition computer time

to empty the list-processor memory and catch-up. During a spill there was the potential for having several particles traverse the apparatus while the system was in the busy state. Thus, data acquisition rates of 600 to 1000 particles per spill were achievable. Due to the possibility of burning out the silicon positional detectors, the rates were kept at about 500 particles per spill.

Data Preparation

To properly characterize the response of the TEPC for a specific ion it was important to eliminate events that could cause misinterpretation of the data. Errors in data processing and fragmentation products were first removed, leaving only those energy deposition events that were a result of a primary ion. These event samples were then reduced to exclude ions that scattered and were no longer traveling parallel to the beam axis. An energy calibration was performed on the remaining data, converting channel number to energy deposited, ε. The beam fluence was then adjusted mathematically to give a uniform coverage over the surface of the TEPC. The final distribution of event frequency as a function of energy deposited represents the response function of the TEPC.

I. Invalid Events

In order to reconstruct the trajectory of each particle, events with errors in positional information were first removed. As discussed above, location of the incident particle was determined in relation to charges q_1 and q_2. Equation 4.9 was used to convert these values to horizontal and vertical coordinates u and v. When an error occurred in either in the data stream itself or in its digital conversion, Equation 4.9 returned a value outside the bounds of the physical dimensions of the positional detectors. Since the position detector operated by charge division, equal, non-zero values of q_1 and q_2 indicated a central location. Another error state was therefore noted when q_1 and q_2 had equal but zero values. The conversion algorithm was designed to assign particles with these associated errors a positional value of -99 so that these events could be easily identified and excluded.

II. Selection of Primary Ions

The next step was the removal of events with nuclear collisions or pulse pileup. In either case, energy deposited in the PSDs was inconsistent with that of a primary beam ion and so they were easily identified by the total charge collected.[60,61] Fig.4.6a shows the number of events as a function of energy deposited in the vertical detector of PSD2 for silicon having an energy of 800 MeV/nucleon. Events causing the prominent peak are single primary ions that have not undergone a nuclear

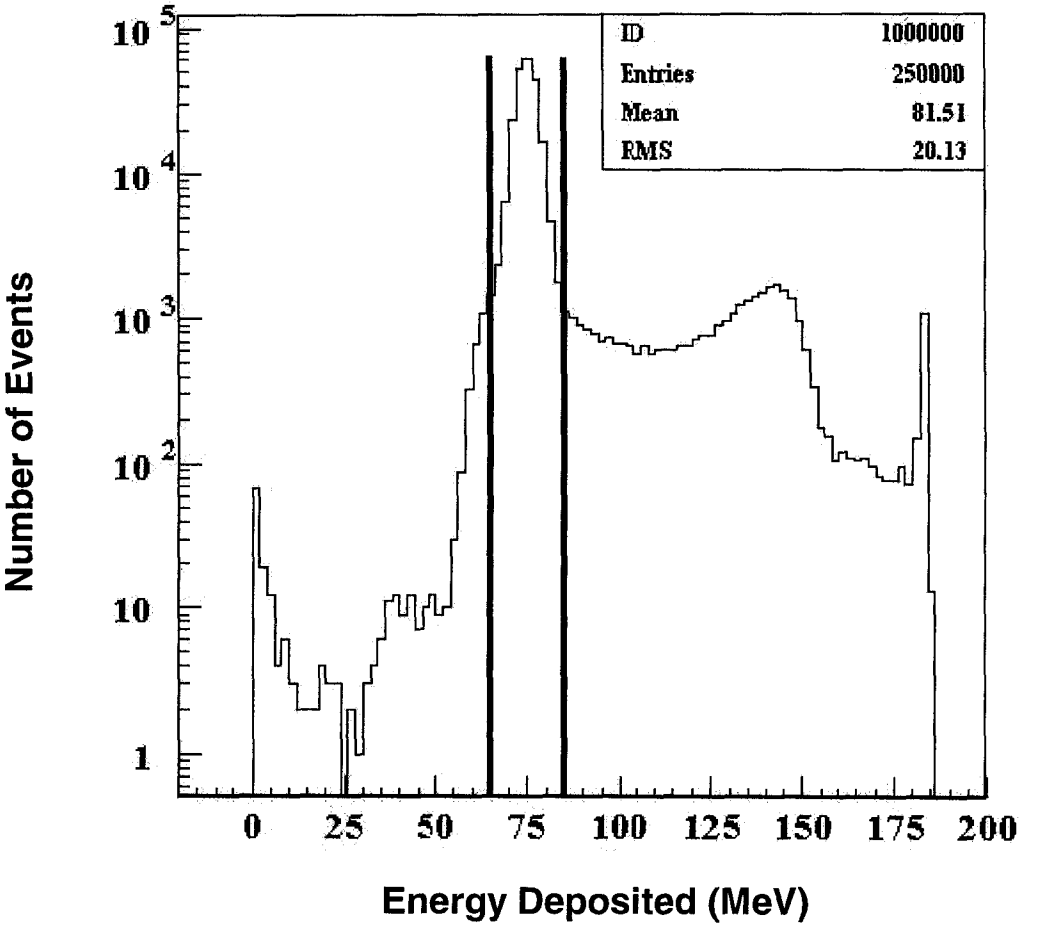

Fig. 4.6a. Energy Deposition in Silicon Positional Detector. Number of events as a function of energy deposited in the vertical detector of PSD2 for silicon at 800 MeV/nucleon plotted on a log-linear scale. Prominent peak of the distribution represents primary ions. Remaining components in the distribution represent ions having a different charge (lower energy depositions) or pileup of more than one event (higher energy deposition). The vertical lines represent the area considered to be primary ions.

collision. Particles depositing a higher energy than those in the primary peak were due to more than one particle being measured during a single trigger, known as pileup.[58]

To the left of the main distribution were fragments having a similar velocity as the primary. Fig.4.6b is a plot of total energy deposition in the vertical detector of PSD4 for the same events of Fig.4.6a showing an increase in fragmentation further downstream. These fragments were easily identified as their energy deposition was proportional to Z^2.[60,62] Selection of only those events contributing to the prominent peak, inside the vertical lines of Fig.4.6a, ensured that only primary ions interacted with the TEPC. When possible, this selection was performed for both the horizontal and vertical detectors of each of the four PSD's.

III. Elimination of Scattered Events

The next selection removed primary events that were not traveling parallel to the beam axis. These events survived the selections above since they had the same charge and velocity as unscattered ions and therefore contributed to the prominent peaks shown in Fig.4.6. To identify these events, trajectories and scattering angles were determined for all events that survived the cuts described so far.

The u and v coordinates recorded by each PSD were first transformed to x and y by the masking technique discussed above in *Data Acquisition*. Fig.4.7 is a representative plot of positional information recorded by the vertical detector of

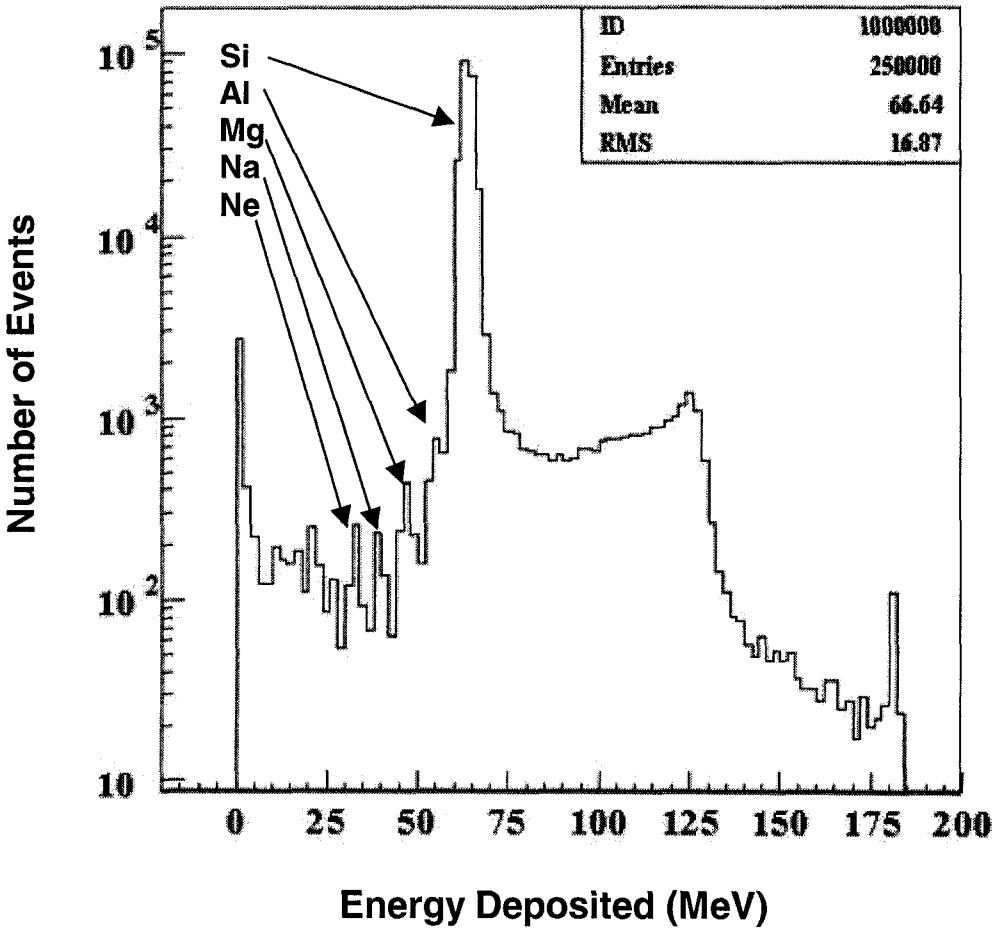

Fig. 4.6b. Energy Deposition in PSD Showing Fragmentation. Number of events as a function of energy deposited in the vertical detector of PSD4 for silicon at 800 MeV/nucleon plotted on a log-linear scale. As compared to Figure-6a, an increase in the number of fragments recorded is shown for events having lower energy deposition than the primary peak.

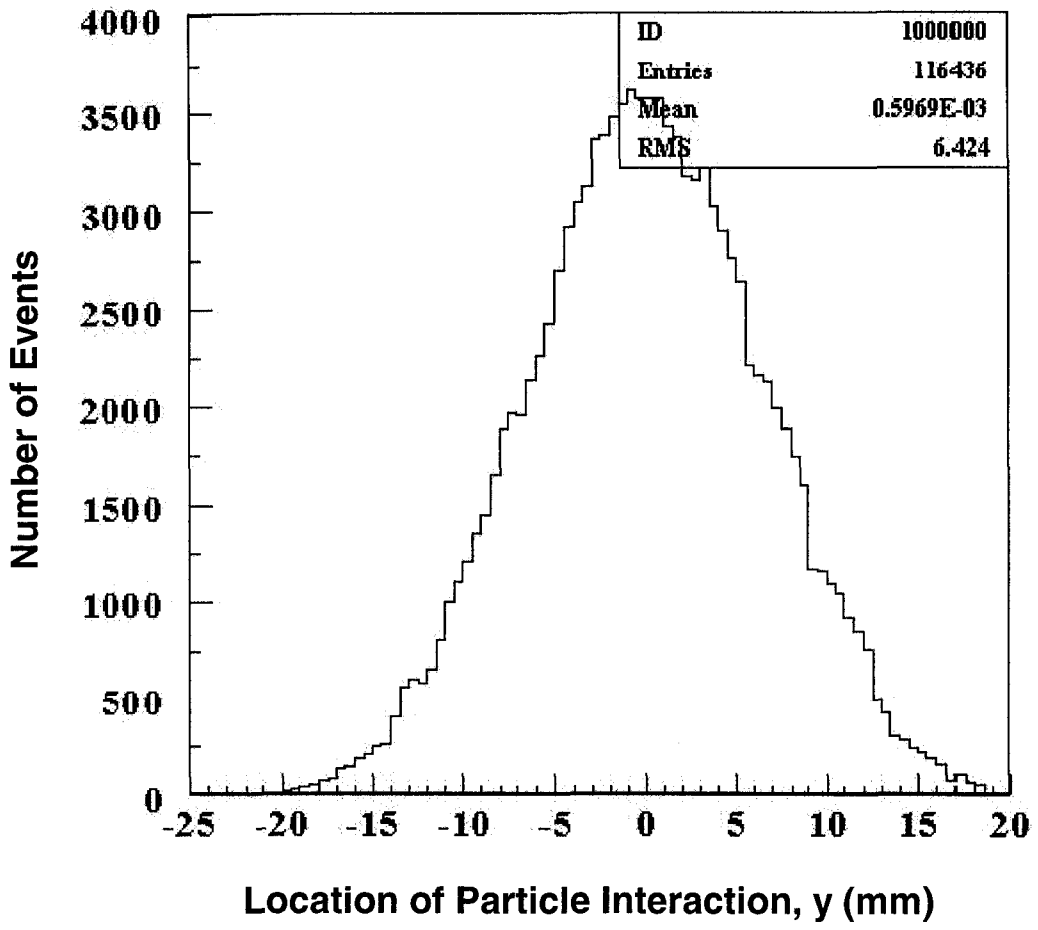

Fig. 4.7. Number of Events as a Function Particle Location Recorded in the PSD. Data was taken from positional information for the vertical detector of PSD2 for silicon at 800 MeV/nucleon. The recorded coordinates have been corrected by applying a masking transformation and now represent the vertical position, y, of the laboratory coordinate system (x,y). As can bee seen, all particles are within the 40 mm diameter of the silicon detector verifying that events having invalid coordinate transformations been removed.

PSD2 after selecting only the primary ion, applying the masking transform and re-aligning the PSD to zero. This was done for both horizontal and vertical detectors in all PSD groups.

The angle of scatter was determined by comparing the difference between similar positional signals of two PSD groups. The result was a second distribution representing the deflection of the particles for the distance traveled, z_{12}, between the two PSD groups, as shown in Fig.4.8. The peak of this distribution being centered about zero shows that most of the remaining particles had little or no divergence from parallel. The tails represent particles that had a significant deflection and were therefore eliminated from the analysis.

Using 2.0 standard deviations from the mean, about 98 percent of the events, many events with large deflections were included in the analysis. Data contained within only 1.0 standard deviation of the mean, 68 percent, eliminated many parallel primary ions. Thus, 1.6 standard deviations, containing 85 percent of the events, was chosen as a balance between maximizing the number of primary ions analyzed while eliminating most of the events with large angles of scatter.

IV. Particle Trajectory Through the TEPC

Selections thus far removed all events except those that constitute a parallel beam of primary particles. The next step was to recreate the trajectory of each ion and define its coordinates with respect to the transverse plane of the TEPC (the plane

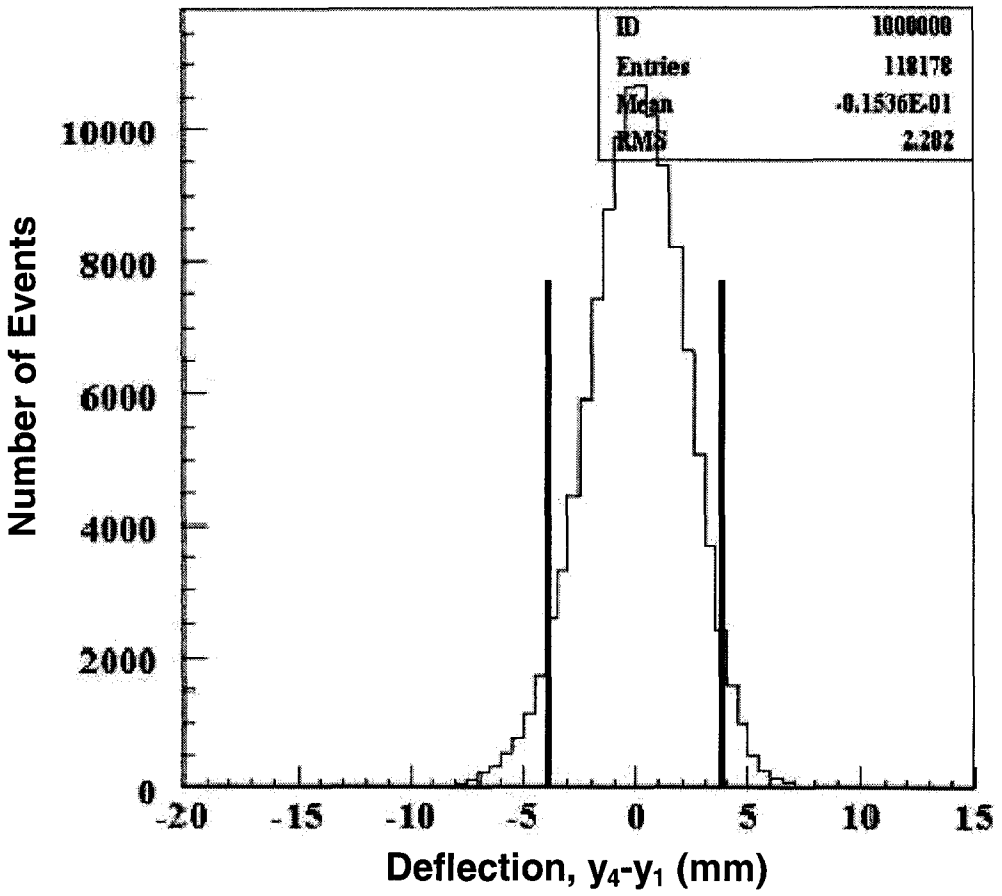

Fig. 4.8. Number of events as a function of deflection between PSD1 and PSD4. As can be seen, the vast majority of particles had relatively straight trajectories. The tails of the distribution represent particles that scattered somewhere between PSD1 and PSD4. Particles outside the heavy black lines were removed. These were events having a magnitude of deflection greater than 4.0 mm (0.165 degrees).

perpendicular to the beam axis). The x and y locations at z_0 were determined for each event based on interpolation of the trajectory between adjacent PSD's. The impact parameter (IP) was then determined for each event, defined as the radial distance that the particle traversed the x,y plane at z_0.

V. Energy Calibration

An energy calibration was performed on the remaining data, converting the TEPC pulse heights into energy deposited. Linearity of the response of both CAMAC ADC's connected to the TEPC was determined using an EG&G ORTEC Model 448 Research Pulser. The distribution of energy deposited from the internally mounted alpha source was then used to associate a known quantity of radiation with specific pulse heights. Details of the calibration are presented in Appendix B.

VI. Beam Fluence Normalization

The final step in preparing the data was to determine the response of the TEPC under conditions of uniform irradiation. Fig.4.9a shows a three-dimensional projection of the beam at the transverse plane of the TEPC ($z = z_0$). The number of events per square millimeter at the outer radius of the TEPC, 8.89 mm, was about half

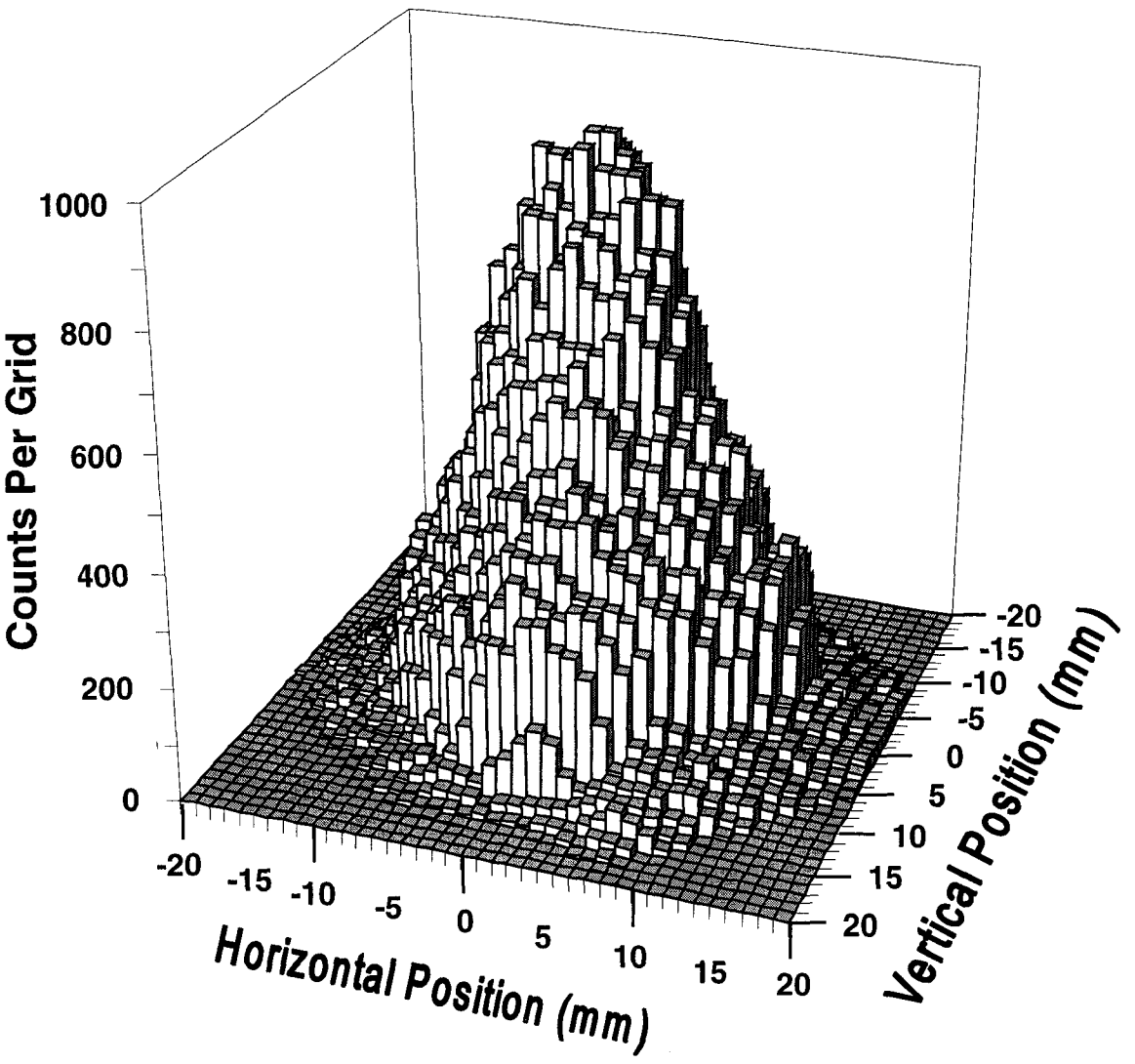

Fig. 4.9a. Three-dimensional plot showing the spatial distribution of the beam. The plot represents the number of events in a grid having 1 mm by 1 mm intervals. The radius of the silicon position detectors, 20 mm, is apparent. At a radius of 9 mm the outer surface of the TEPC sphere was fully covered by the beam. Each grid interval at this radius contains only about half the number of events that are found at the center of the beam.

the number occurring in the center. To account for this, the x,y plane through the center of the TEPC was sub-divided into 1 mm by 1 mm grids. The total number of events in each grid was found and normalized to a unit count. The overall distribution was then re-assembled and divided by the total number of grids used. The resulting event weighted beam represents a uniform fluence over the surface of the TEPC as shown in Fig.4.9b. The distribution of energy deposited in the TEPC under uniform irradiation, the response function, formed the basis from which all further analysis was derived.

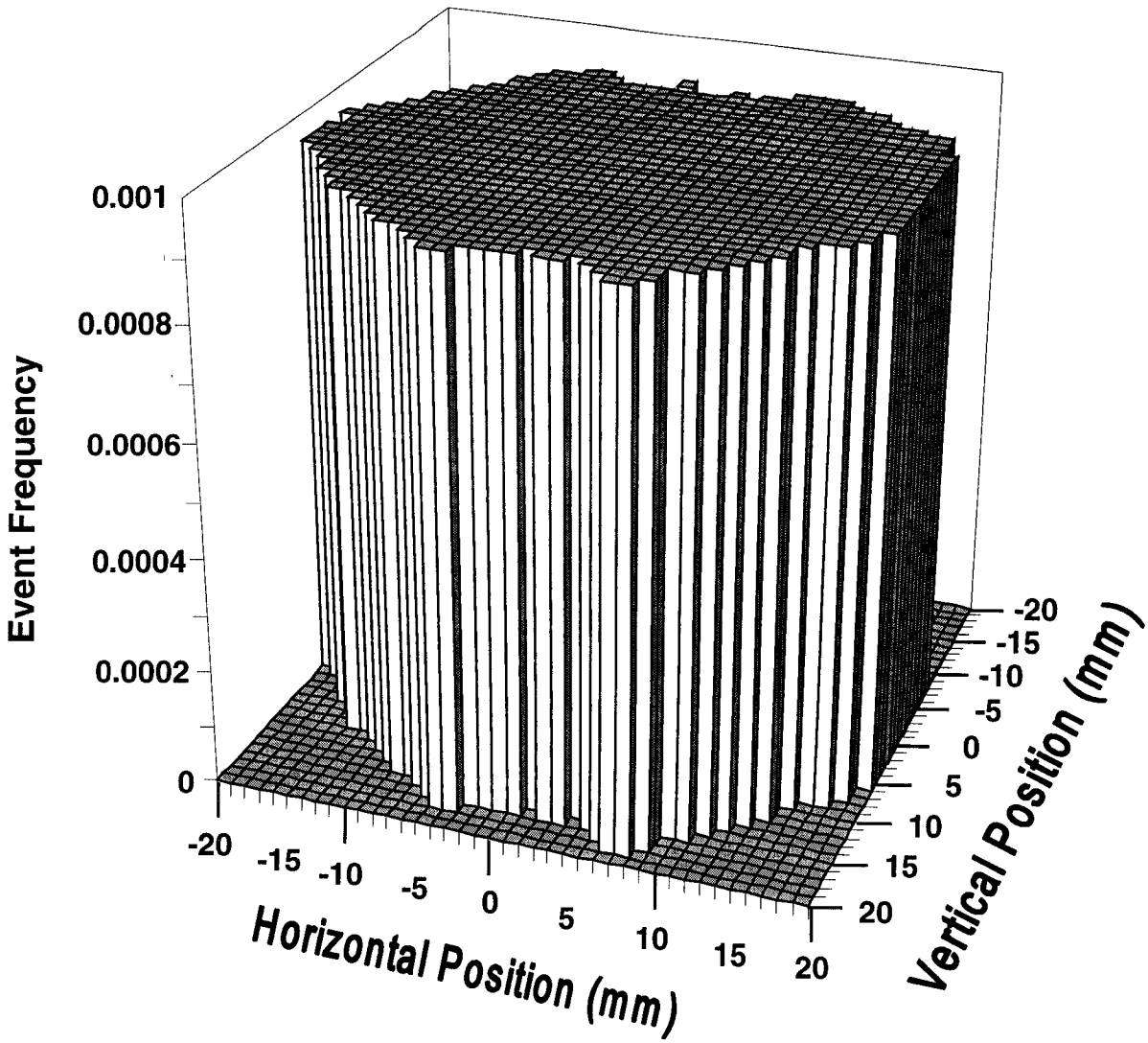

Fig 4.9b. Representation of the beam after normalizing the counts in each grid interval. The number of counts in each interval was first normalized to unity. Each grid interval was then divided by the total number of intervals containing a non-zero value. The result is a uniformly irradiating beam normalized to one event.

CHAPTER V - RESULTS AND DISCUSSION

Table-5.1 gives a summary of the properties of the ions used in this study. Prior to the experiment it was determined that three millimeters of lead would be required to reduce the energy of the oxygen beam so that the LET at the TEPC cavity more closely matched the other ions. At the time of beam delivery, the energy of oxygen at the exit window was less than expected and not precisely known. Observing energy deposited in the TEPC, it was determined that only two millimeters of lead should be used to adjust the LET of the beam. Using the Bethe-Bloch equation to determine energy loss in all components upstream of the TEPC the energy of oxygen at beam exit was later found to be 165 MeV/nucleon instead of the 180 MeV/nucleon expected. The average energy deposited in the TEPC was in turn slightly lower but still within ten percent of the other ions.

Table-5.1
Characteristics of Ions Studied

	Location					
	Beam Line	TEPC Gas Cavity				
Ion	Energy (MeV/nucleon)	Energy (MeV/nucleon)	Velocity (V/C)	LET (keV/μm)	Residual Range (cm-H_2O)	Maximum Energy Electron (keV)
Nitrogen	100	79	0.386	43.1	1.4	179
Oxygen	165	119	0.461	40.9	2.7	276
Neon	230	211	0.577	43.8	5.6	511
Silicon	800	781	0.838	46.4	32.6	2,407

Fig.5.1 shows the response of the TEPC to a uniform fluence of particles. There is a prominent peak of the distributions occurring at an energy deposition of approximately 30 keV. The frequency of low energy events differs for all ions, believed to be due to differences in the track structure, but the pattern of energy deposition is similar for all ions. The properties of the response functions presented in Fig.5.1 are shown in Table-5.2. The frequency mean lineal energy, $\bar{y}_f$, dose mean lineal energy, $\bar{y}_d$, and the relative variance in the distributions were found as discussed in Chapter III by converting the response of the TEPC as a function of energy deposited, ε, into distributions of lineal energy, y.

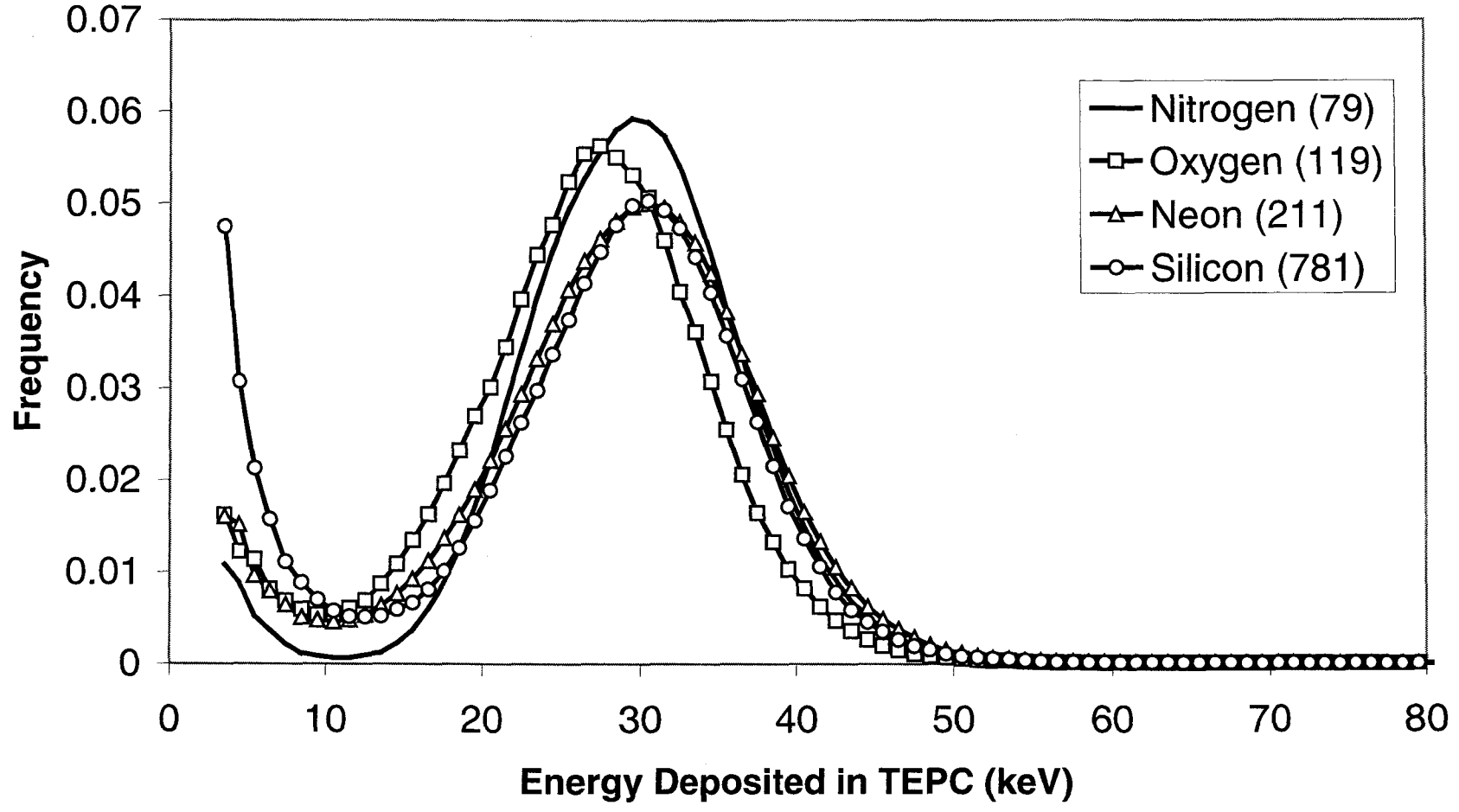

Fig. 5.1. TEPC Response Functions. Represents the response of the TEPC to a uniform fluence of parallel particles having similar LET. Each distribution has been normalized to unity, with the energy at the TEPC in parenthesis in the inset. The larger frequency of low energy events occurring in the detector in response to silicon is due to an increase in delta-ray influx caused by the much larger track structure associated with the ion, resulting in the distribution taking the shape of the wall-less distribution of Figure-L3. The narrower shape of the nitrogen distribution, and the lack of low energy events were due to the low energy of the beam. Nitrogen was nearing the end of its range in the longest paths through the detector wall.

Table-5.2
Summary of Data Analysis

Ion	Calculated LET (keV/μm)	$\bar{y}_f$ (keV/μm)	$\bar{y}_d$ (keV/μm)	$\bar{y}_f$/LET	$\bar{y}_d$/LET	Relative Variance of the Distribution
Nitrogen	43.1	43.7	46.8	1.01	1.09	0.071
Oxygen	40.9	39.1	43.9	0.96	1.07	0.123
Neon	43.8	42.4	47.6	0.97	1.09	0.123
Silicon	46.4	39.4	46.7	0.85	1.01	0.185

Cumulative distributions of the response functions are plotted in Fig.5.2. The large differences between the four response functions for low energy events are shown to have a minimal effect on when plotted cumulatively. Though variations in the low energy region are present, 50% of the energy is deposited below an energy of about 28 keV for all ions. The distributions become very similar above this point. For higher energy events, more important in dose assessment, cumulative plots show that most of the energy is deposited in much the same manner for each of the ions.

Multiplying the event frequencies by the energy deposition associated with the event, or $\varepsilon * f(\varepsilon)$, shows the distribution of energy deposition as a function of event size. This is shown in Fig.5.3. The difference in the number of events observed in the low energy deposition region are shown once again to be minimal in an assessment of how dose is delivered. The mean value of these distributions, in terms of lineal energy, is given in Table-5.2 as $\bar{y}_d$.

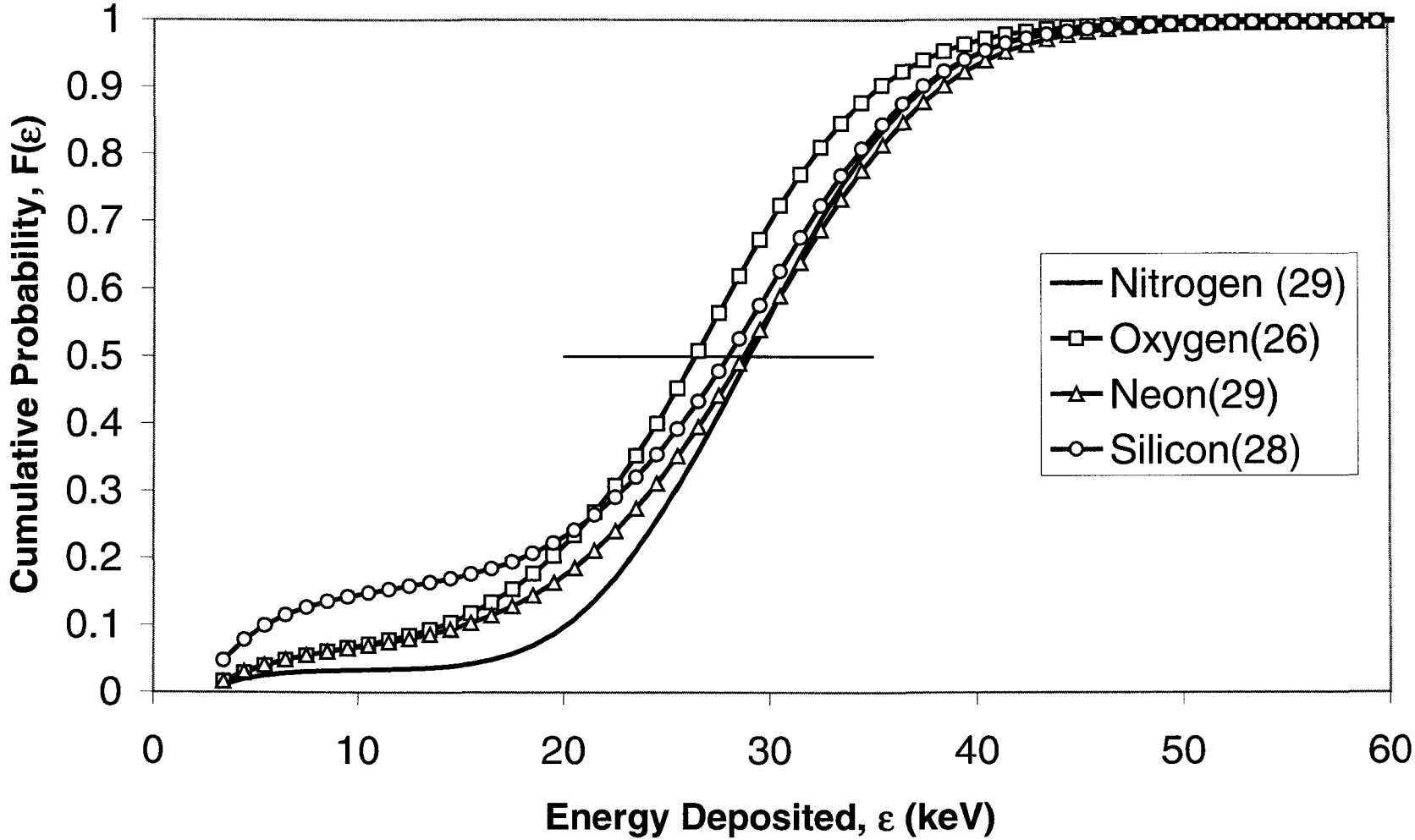

Fig. 5.2. Cumulative Distributions of TEPC Response. Cumulative probability as a function of energy deposited, ε, in the TEPC shows minimal effect of low energy differences. Thin horizontal line represents the point in the data sets corresponding to 50% cumulative probability. The numbers in parenthesis in the inset, in keV, marks the point at which 50% of the energy is deposited.

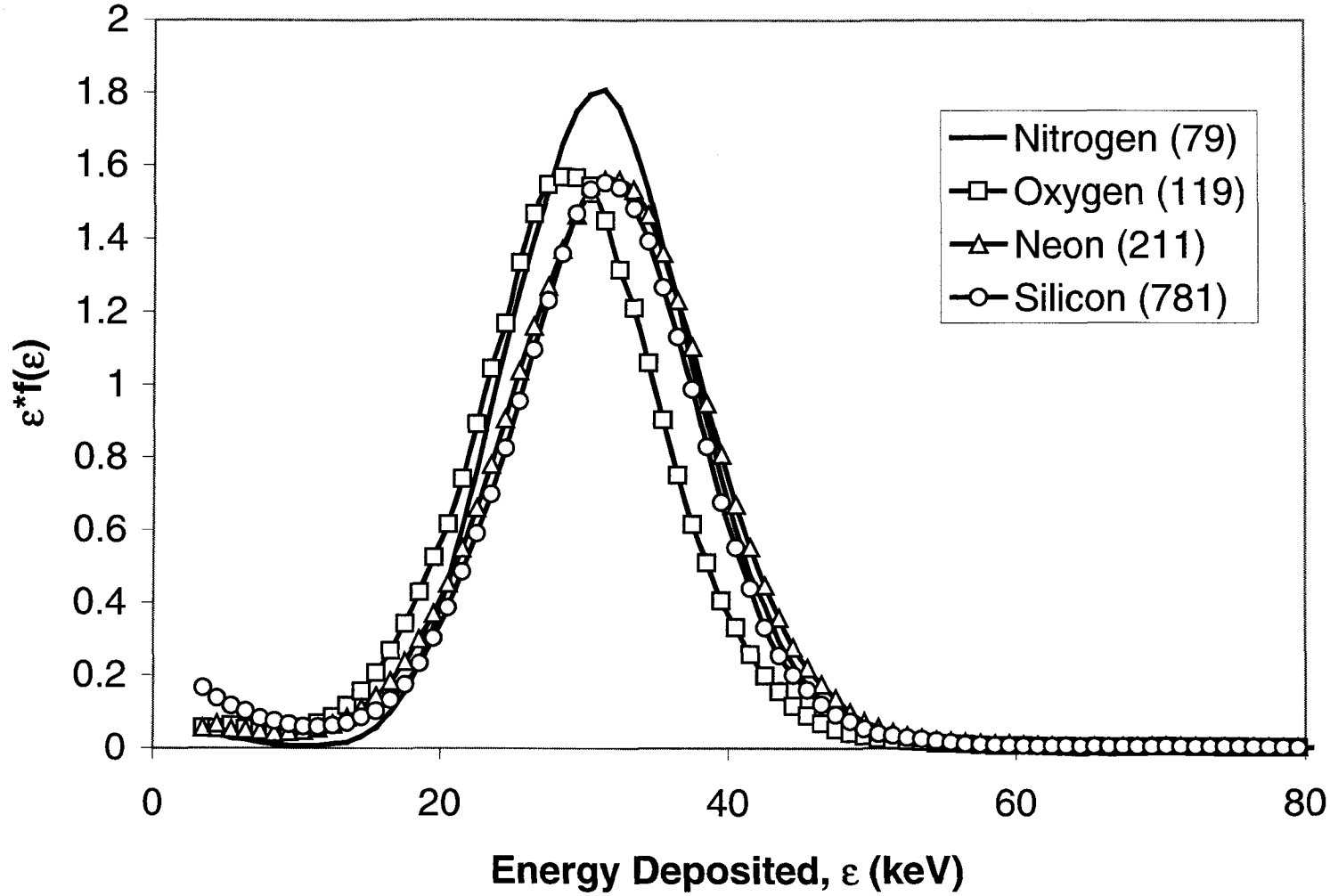

Fig. 5.3. Energy Deposited as a Function of Event Size. Multiplying the energy associated with an event, ε, by the frequency of its occurrence, f(ε), gives a determination of how the dose is delivered. The variability between the spectra in the left tail is minimized due to their low energies. The means of these distributions occur at an energy of about 36 keV. The standard deviation is about 5 keV for all four.

Selected Trajectories

Selecting events with impact parameters less than 0.8 mm results in particles having simulated path lengths of one micrometer, varying less than 1.0 percent. Plotting these events in Fig.5.4, the peak for all ions occurs at approximately 36 keV.

For particles having these impact parameters, the idealized energy deposition would be equal to LET times path length, the diameter of the detector. Since many of the high-energy delta rays produced by the ions had ranges larger than the simulated dimension of the TEPC, a portion of the energy that was liberated within the sensitive volume was deposited outside the TEPC and was not recorded. Based on mean values of the selected events, presented in Table-5.3, the data indicated that there was about a 17% loss in energy deposited from that expected by the LET times path length approximation. For silicon there was about a 22% loss. Previous measurements of ^{56}Fe having energies from 200 to 1,000 MeV/nucleon, recorded with the same TEPC, showed an average loss of about 20% for particles with these impact parameters.[16]

Track Structure Modeling

Track structure and radial dose models were used to compare the data to estimates from calculations. (Appendix C) The track structure model described by Chatterjee[18] predicts 24 percent loss for the lowest energy ion, nitrogen, up to a loss

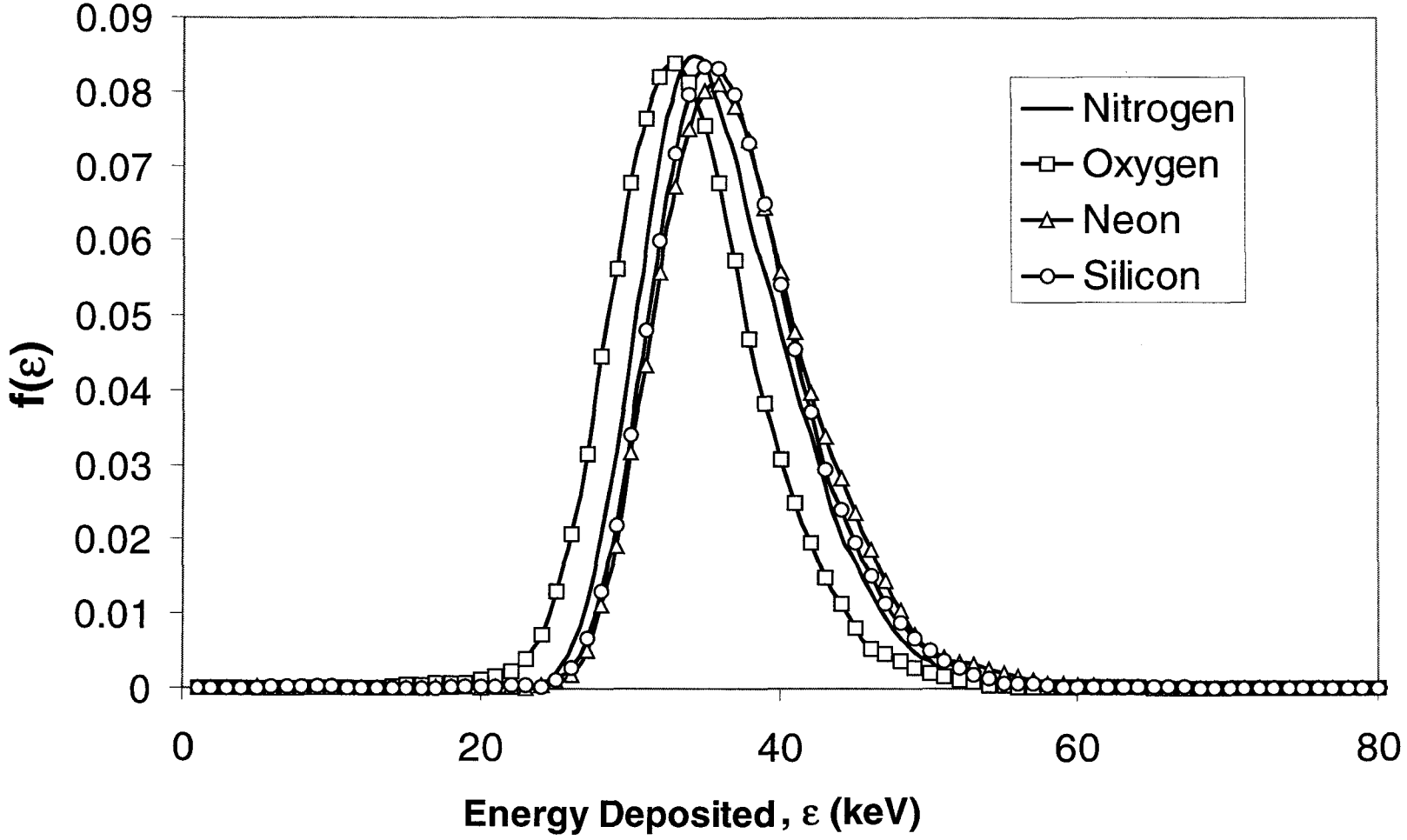

Fig. 5.4. Distribution of Energy Deposited for Particles Having Impact Parameters Less Than 0.8 mm. This impact parameter gives path lengths across the diameter of the detector, 1μm, varying less than 1.0 percent. The average energy deposition of oxygen was slightly lower due adjustment of beam energy at the time of the experimental run with a Pb moderator. However, the percent of energy retained in the detector, with respect to the LET of the ion, was very similar in all cases..

Table-5.3
Events with Impact Parameters less than 0.8 mm

Ion	Beam Energy (MeV/nucleon)	Peak (keV)	Median (keV)	Mean (keV)	Standard Deviation (keV)	LET times path length approximation (keV)	Percent Radial Loss
Nitrogen	100	34.0	35.0	35.7	5.19	43.1	17.2
Oxygen	165	33.0	33.0	33.5	5.42	40.9	18.1
Neon	230	36.0	36.2	36.9	5.63	43.8	15.8
Silicon	800	35.0	35.9	36.4	5.40	46.4	21.6

of 32 percent for silicon having the highest energy. The Cucinotta[19] radial dose model predicts losses of 30 to 39 percent for the lowest to highest energy ions, respectively. The differences observed between measured data and calculations stems from the assumptions used in the models. Both models use an infinite homogenous target medium and calculate the energy liberated by the ion in cylindrical volumes surrounding the ion trajectory.

These radial models were adjusted to simulate a spherical geometry by using very small track segments. Using track segments ten nanometers in length and varying radii to simulate the shape of a sphere using very thin cylinders, energy escaping the volume as predicted by Chatterjee increases and ranges from 29 to 36 percent while the model presented by Cucinotta predicts 38 to 44 percent energy loss.

Energy escaping is increased since volume of a one micrometer diameter sphere is less than a one micrometer cylinder with equal height and diameter.

Though energy escaping the volume is considered in both models, no energy influx due to electrons created outside the cavity is included. The TEPC, however, exhibits a change in density on the order of 10^4 times at the wall-cavity interface. A much greater number of electrons of all energies are liberated in the dense wall than in the evacuated cavity. Many of these electrons have sufficient energy to traverse the wall and enter the gas cavity. At the cavity-wall interface, even the low energy electrons enter the TEPC in much greater numbers and are recorded. The models therefore under predict energy deposited in the TEPC.

Using Cucinotta's approach to describe the radial distribution of dose, the response of a spherical TEPC to a uniform irradiation was simulated, as described in Appendix C. The radial dose distribution was first converted into a radial distribution of energy. A trajectory with respect to the center of a one micrometer diameter sphere was chosen at random and the structure of the track was superimposed on the sphere. The intersection between the sphere and the calculated ion track was found and energy deposition to the sphere found. The simulated response of the TEPC, which assumes a homogenous medium is presented in Fig.5.5.

The results of Nikjoo, et.al., comparing the simulated response of a TEPC considering homogenous (wall-less) and non-homogenous (walled) volumes indicates that it is not the model that under predicts energy deposition to the TEPC, but the assumption of homogenous conditions. Eighty percent of energy deposition in both wall-less and walled cases was due to secondary electrons generated within the

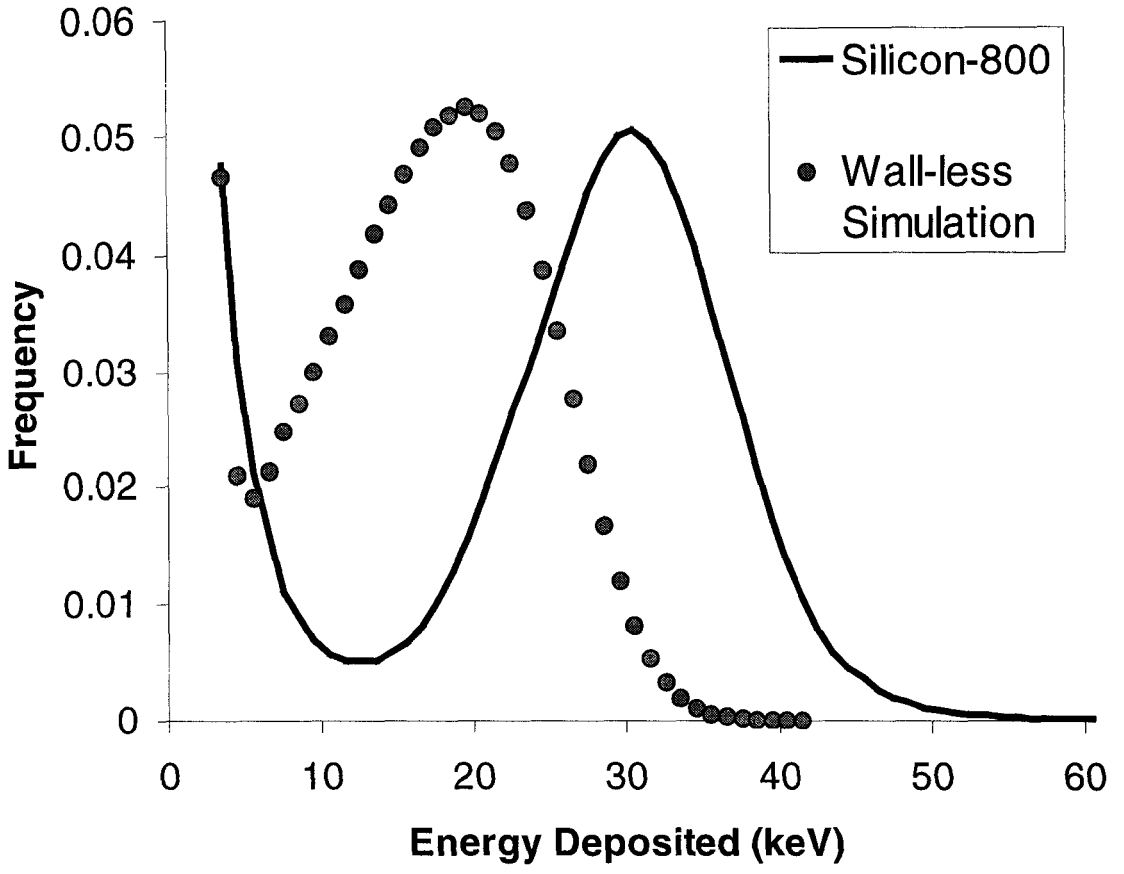

Fig. 5.5. Simulation of TEPC Response for an Irradiation by Silicon in a Homogenous Medium. Black line shows the response of a walled TEPC to silicon at 800 MeV/nucleon. Points represent a simulation of TEPC response using the radial distribution of dose described by Cucinotta. The shape of the simulation is similar to the measured distribution but with a lower mean value. This is due to the underlying assumption in the radial dose model of a homogenous medium. Particles crossing the cavity of a walled detector would be enhanced by an increased influx of electrons created in the detector wall. (see reference 20).

detector cavity when the primary ion crosses the volume. The other twenty percent, however, was due to secondary electrons produced in different locations depending on whether the wall was present or not.

For the homogenous, wall-less detector the remaining twenty percent of energy deposition was primarily due to electrons created by ions passing outside the cavity. These electrons entered the cavity normal to the ion trajectory. When simulating the non-homogenous, walled detector, the remaining twenty percent of energy deposition was shown to be from electrons created in the wall, outside of the cavity, from ions crossing the volume. These electrons were preferentially in the forward direction and entered the cavity along with the primary ion. Adjusting the simulation of energy deposition shown in Fig.5.5 by about twenty percent for ion trajectories crossing the detector volume results in a closer approximation to the measured data. Fig.5.6 shows the improvement of the simulation of silicon at 800 MeV/nucleon plotted against measurements of the same ion at the same energy.

Measured Wall Effects

Fig.5.7 is a scatter plot of measured energy deposited versus impact parameter for neon. The mean energy deposition as a function of impact parameter and the mean impact parameter as a function of energy were compared for these distributions in a similar fashion as in the work of Gersey[16] and Rademacher.[17] From the center of the TEPC outward, the transverse plane of the TEPC was divided into annuli

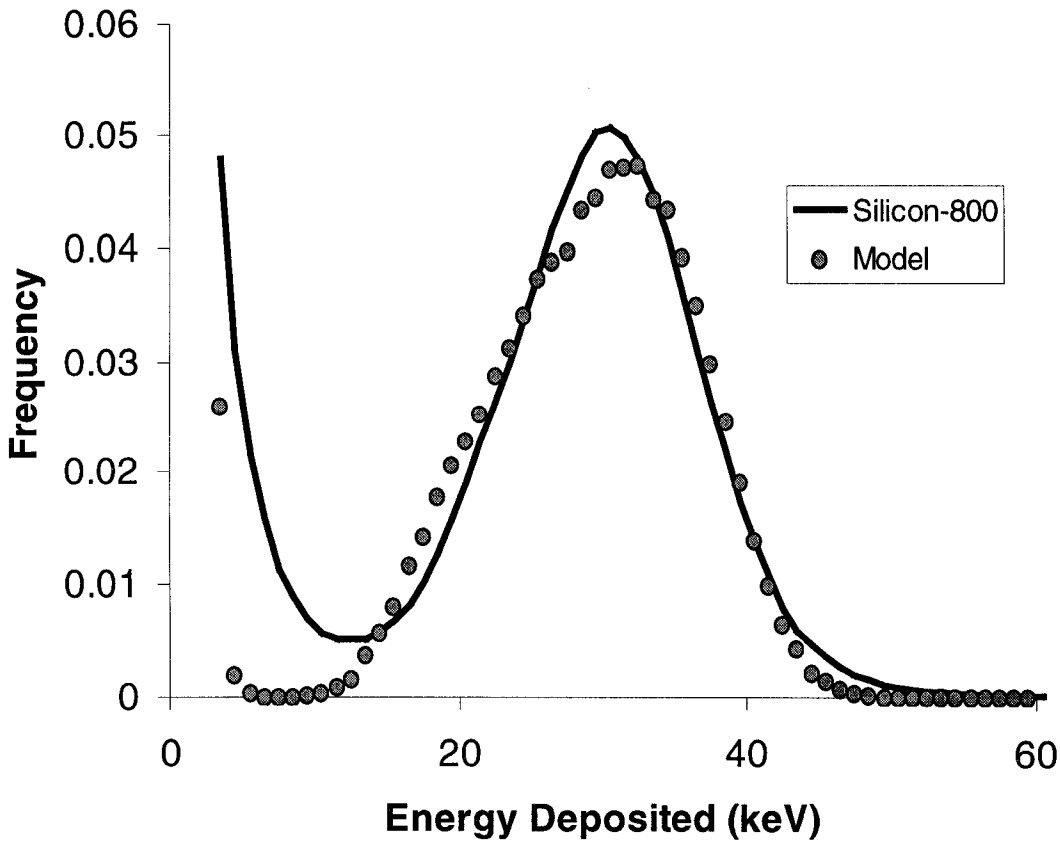

Fig. 5.6. Adjustment of Simulated TEPC Response for a Non-homogenous Medium. Black line represents measured TEPC response to silicon with an energy of 800 MeV/nucleon. Gray points show the simulated TEPC response to the same ion for a walled detector by enhancing energy deposition for particles crossing the detector volume.

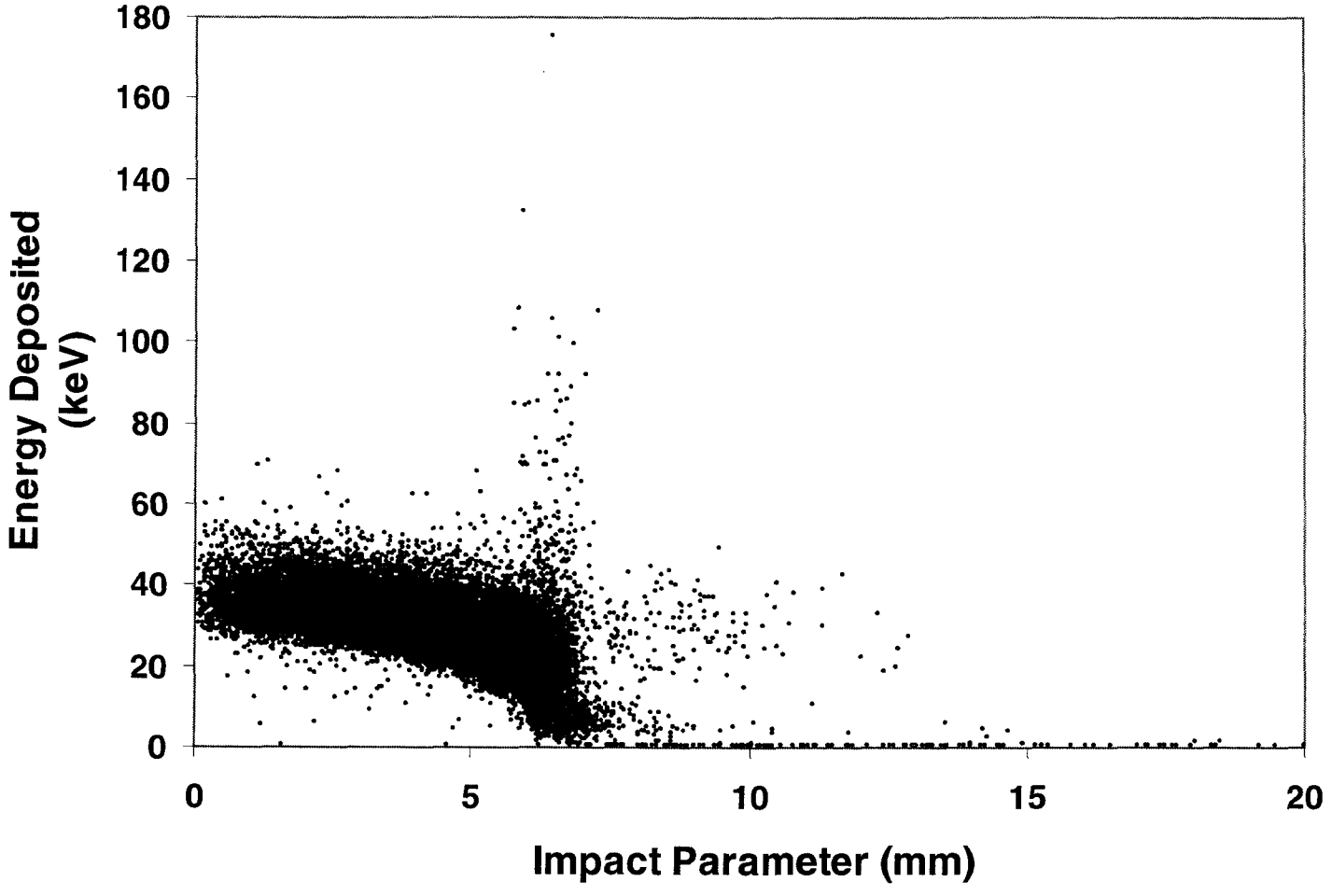

Fig. 5.7. Scatter-plot of Energy Deposited versus Impact Parameter for neon at 211 MeV/nucleon. The sharp drop occurs at the gas wall interface with a pronounced peak due to delta ray influx.

having equal areas. The mean energy deposition within each annulus was then calculated and plotted for an impact parameter occurring at the midpoint of the inner and outer radii of the annulus where the events occurred.

Due to the very low frequency, very large energy deposition events shown in Fig.5.7 at an impact parameter near the cavity-wall interface, 6.35 mm, were not visible after the method of averaging discussed above. To overcome this, the range of energy deposition was divided into equal areas and the average impact parameter found. Energy deposition events above about 55 keV/μm occurred only in the region of the gas-wall interface and could be clearly distinguished. Both methods of averaging were combined into the composite plot of Fig.5.8.

Also shown in Fig.5.8 is energy deposition approximated by multiplying the LET of the particle by its path length across the detector cavity. Particles passing through the gas cavity have energy depositions lower than predicted by this approximation due to more energy escaping the detector volume than enters from the production of electrons in the dense the wall. As the impact parameter approaches the radius of the detector cavity, energy influx begins to overcompensate losses and the average energy deposition becomes larger than predicted. At trajectories equal to the cavity radius, a large number of low energy electrons liberated in the dense wall enter the cavity and are recorded as large single energy depositions giving rise to the sharp peak observed. This anomalously large energy deposition was confirmed in Nikjoo's simulation of the response of a spherical walled TEPC, but was absent in simulating a wall-less detector.[20]

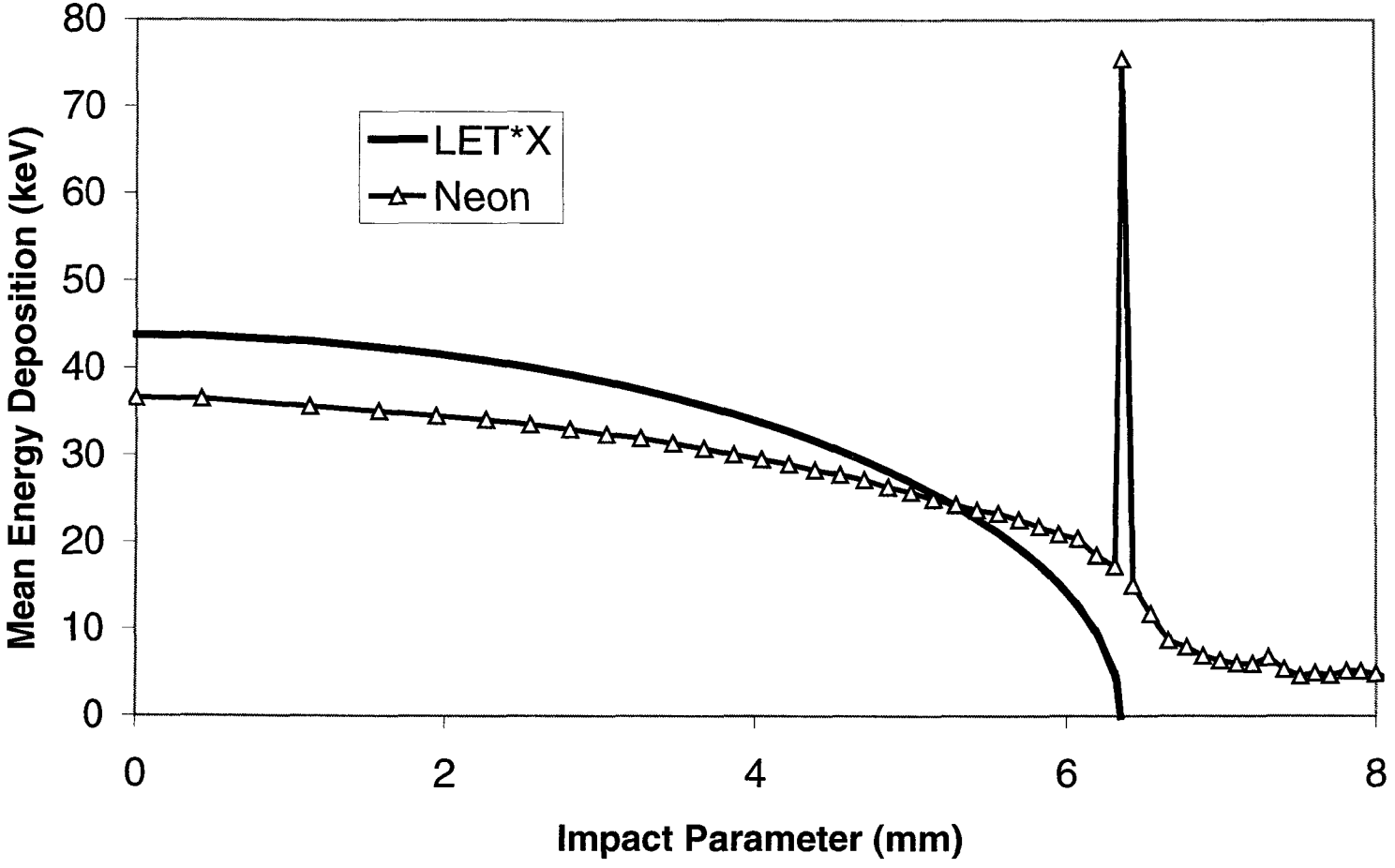

Fig. 5.8. Mean Energy Deposited by a 211 MeV/nucleon ^{20}Ne Particle for a Given Impact Parameter. Circles represent measured data. Smooth thick line represents a simple LET times path length approximation for the LET of the ion shown, 43.8 keV/μm. The detector measures less than LET time path length for particles crossing the sensitive volume due to energy transported out of the site by high-energy delta rays. Close to the gas-wall interface, more energy in recorded than predicted due to an increase in delta-ray influx with a sharp peak occurring just at the cavity radius.

Comparison of Individual Distributions

Because of the many processes involved in energy deposition within the sensitive volume of a TEPC, no single function adequately describes the measured spectra and population summary statistics such as the mean and variance do not completely describe the shape of the distributions. However, since there are over $5x10^5$ data points for each measured response function, the distributions do not require statistical fits to determine if they were sampled from a specific family of a known distribution. With this many data points, the spectra are themselves known distributions and may be analyzed directly.

Tests were performed, however, to confirm this position. A function completely describing the distribution of energy deposition is not known since the response of a TEPC is the result of many underlying processes. Non-parametric approaches were therefore used to compare the measured response functions. The Kruskal-Wallis test, a non-parametric equivalent to the ANOVA procedure, was used in a four-way comparison to test equality of means.[67] An underlying assumption of the Kruskal-Wallis test is that the distributions have the same shape but possibly different locations. The test statistic, based on a sum of ranked scores of the data, gets larger as the differences between the population means increase. The resulting test statistic is distributed Chi-squared with degrees of freedom equal to the number of samples minus one (3 in this case). The null hypothesis that the distributions had the same mean value could not be rejected.

The Kolmogorov-Smirnov goodness-of-fit approach was used to test the cumulative distributions of the response functions against each other.[68] The two sample test measures the maximum deviation between the cumulative empirical distribution functions to determine whether the distributions are derived from the same function. The null hypothesis that the distributions were the same was rejected in all possible two-way comparisons with a calculated *probability-values* less than 0.001.[69] Thus, the response functions created by different ions having similar LET are different distributions, having the same mean. Results of both tests are shown in Table-5.4

Table-5.4.
Kolmogorov-Smirnov and Kruskal-Wallis Test Statistics

Comparison	Critical Value	Calculated Test Statistic	P-value
	Kolmogorov-Smirnov		
N - O	0.1453	0.2906	< 0.001
N - Ne	0.1074	0.2147	< 0.001
N - Si	0.0778	0.1557	< 0.001
O - Ne	0.0515	0.1030	< 0.001
O - Si	0.0737	0.1474	< 0.001
Ne - Si	0.0357	0.0714	< 0.001
	Kruskal-Wallis		
Four-Way	7.8150 (α=0.05)	5.3310	0.2289

These distributions, presented in Fig.5.1 exhibit clear differences when plotted on a log-linear scale as shown in Fig.5.9. The nitrogen data shows a large divergence in both the high and low energy regions. Previous experiments measuring ^{56}Fe from 200 to 1,000 MeV/nucleon with the same TEPC showed that both very low and very high energy events were due to particles having impact parameters equal to the radius of the cavity, the gas-wall interface.[16] This was verified in the present study by careful selection of events based on energy deposition.

Fig.5.10a shows the coordinates of particles having energy depositions between 3 and 5 keV, taken from the response of neon. Fig.5.10b shows the location of neon ions having energy depositions greater than 60 keV, twice the average energy deposition. Both types of events occur in the region of the gas-wall interface. Due to the lower energy of the nitrogen beam, many of the particles were nearing the end of their range in many of the longest paths through the dense detector wall. Energy deposition by nitrogen at these trajectories was therefore greatly reduced and plots such as Fig.5.10a and Fig.5.10b could not be made.

This illustrates the point that the range of electrons ejected by the primary ion passing through material is dependent upon the velocity of the ion. Thus, the competing processes of energy loss for ions having impact parameters less than the inner radius of the cavity and energy influx for particles passing outside the cavity occur in different magnitudes for the different energy ions, even though their LET is similar. For higher velocity ions, energy is deposited further from the path of the ion than in the case of lower velocity ions. Higher energy ions may therefore cause

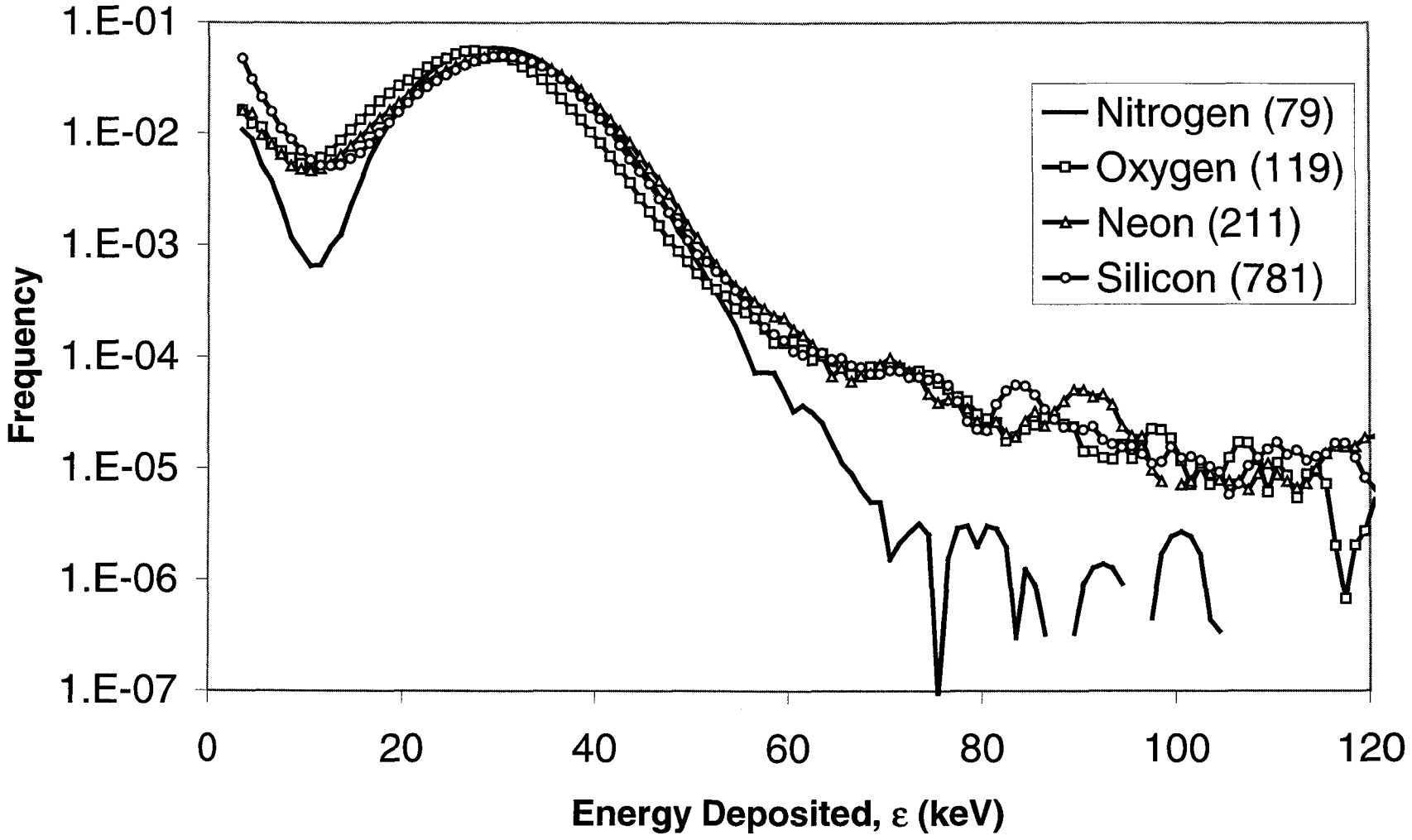

Fig. 5.9. TEPC Response Functions Plotted on a Log-linear Scale. Energy of the ion at the detector cavity, in MeV/nucleon, is shown in parenthesis in the inset. TEPC response to oxygen, neon and silicon is very nearly the same while there is a lack of events in the nitrogen spectra at both low and high energies. Events depositing these energies were shown to be due to particles passing through the longest trajectory of the detector wall. Nitrogen ions with these trajectories were slowing appreciably with a reduction in the energy of the electrons ejected from the track. These electrons did not have sufficient range to make it into the detector resulting in the lack of events shown.

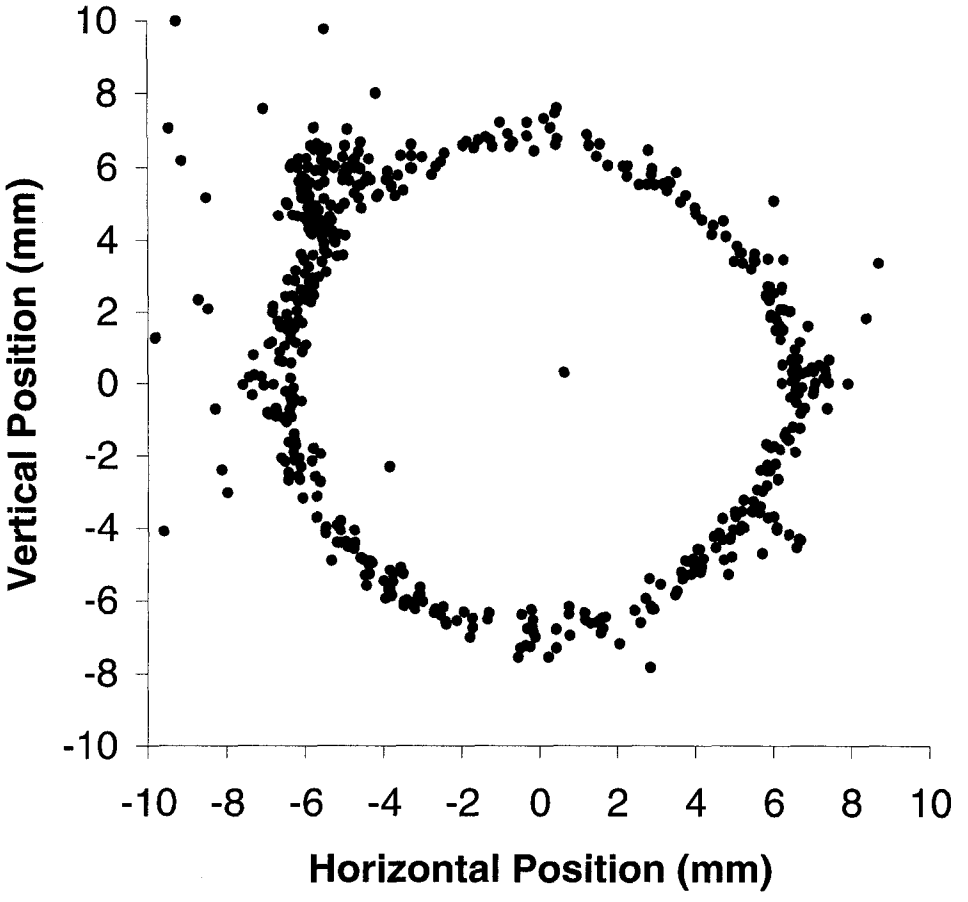

Fig. 5.10a. Location of Particles Having Low Energy Depositions. Data taken from the response of the TEPC to neon with an energy of 211 MeV/nucleon at the detector volume. Points represent the location of ion traversal with respect to the center of the TEPC (x,y = 0,0) for particles depositing 3 and 5 keV in the detector. All of the particles have trajectories through the wall of the detector very near the cavity/wall interface (6.35 mm).

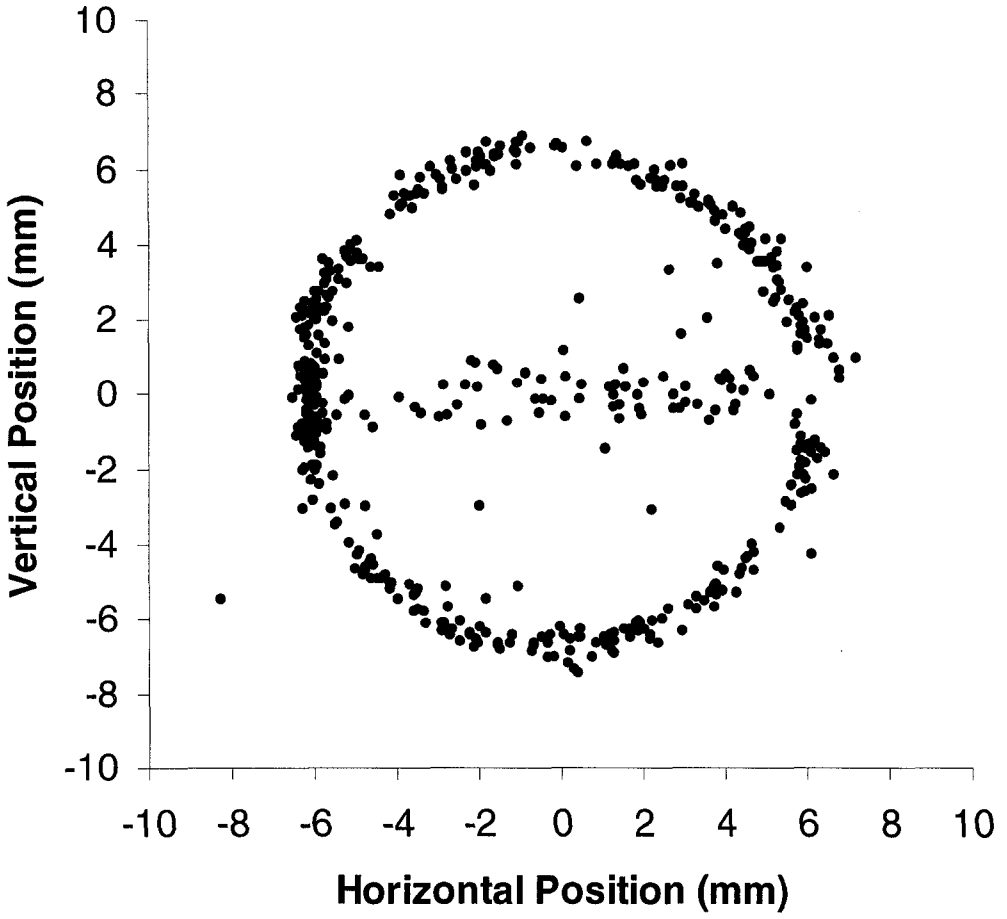

Fig. 5.10b. Location of Particles Having High Energy Depositions. Data taken from the response of the TEPC to neon with an energy of 211 MeV/nucleon at the detector volume. Points represent the location of ion traversal with respect to the center of the TEPC (x,y = 0,0) for particles depositing greater than 60 keV in the detector. Most of the particles have trajectories through the wall of the detector, as in the plot of low energy events. Unlike the plot of low energy events, there are also particles that passed through the center of the detector. These represent particles interacting with the central anode and helix wire.

energy deposition events within the TEPC from distances further outside the TEPC volume, as well as exhibit a larger amount of radial loss for particles crossing the cavity.

These differences are also seen in the TEPC response functions. Silicon, having a much greater energy than the other ions, shows a higher frequency of events with low energy deposition. Selecting only these events shows trajectories in the region of the wall. (as in Fig.5.10a for neon) As shown in Table-5.3, silicon also shows larger energy escaping the volume of the TEPC for particles crossing the gas cavity due to the larger volume of energy deposition associated with its track.

Even in the presence of these differences, the frequency mean and dose mean values for lineal energy are very similar. Due to the very large number of counts within each response function the summary statistics exhibit very small standard errors as presented in Table-5.5. The frequency means of all response functions were within four percent of their calculated LET for all ions except silicon, which was within fifteen percent. Silicon, at 800 MeV/nucleon, showed larger radial losses resulting in a larger divergence between the calculated frequency mean of the measured distribution and the LET of the particle. The calculated values of the dose mean lineal energy, $\bar{y}_d$, showed the opposite trend. For the lower energy ions, $\bar{y}_d$ was within nine percent of calculated LET while that of silicon was within one percent. Thus, $\bar{y}_f$ was a better predictor of LET for the lower energy ions in this study and $\bar{y}_d$ was closer for the higher energy ions.

Table-5.5

Error in $\bar{y}_f$ and $\bar{y}_d$

Ion	$\bar{y}_f$	Error in $\bar{y}_f$	$\bar{y}_d$	Error in $\bar{y}_d$
Nitrogen	43.7	0.021	46.8	0.019
Oxygen	39.1	0.024	43.9	0.024
Neon	42.4	0.025	47.6	0.024
Silicon	39.4	0.025	46.7	0.022

Determination of Average Quality of the Radiaiton

Recommendations of ICRP Report 40 would have assessed a quality between 5 and 10 for ions having an LET between 23 and 53 keV/μm in water.[33] Current recommendations contained in ICRP Publication 60 give exact values as presented in Table-5.6 under the heading Q(LET). Previous studies measuring ^{56}Fe with energies ranging from 200 to 1,000 MeV/nucleon indicated that $\bar{y}_d$ gave a more accurate determination of the average quality of the incident radiation, and thereby dose equivalent, as $\bar{y}_f$ consistently underestimated LET.[16] Results of the present study indicate that, for all ions with energies less than and including neon, replacing LET with $\bar{y}_f$ may be a more accurate determinant of radiation quality than $\bar{y}_d$.

Also shown in Table-5.6 are determinations of Q using alternative approaches. The first is based on the current ICRP60 definition of quality with the assumption that

y is equal to LET, or Q(LET = y).[21] The second is based on a method derived by Kellerer and Hahn where quality is based on the lineal energy spectra, Q(y) with a modification for energy loss straggling.[34] These two methods weigh the quality associated with a specific lineal energy by its frequency of occurrence. These weights are then summed to determine the average quality of the radiation. Quality factor as a function of the frequency mean lineal energy, $Q(LET = \bar{y}_f)$, and the dose mean lineal energy, $Q(LET = \bar{y}_d)$, using the ICRP60 definition are shown in the last columns of Table-5.6. These last methods simply replace the average LET with the appropriate summary statistic, $\bar{y}_f$ or $\bar{y}_d$.

Table-5.6

Derived Quality Factors Based on LET, Lineal Energy, $\bar{y}_f$, and $\bar{y}_d$

Ion	Q(LET)	Q(LET=y)	Q(y)	$Q(LET = \bar{y}_f)$	$Q(LET = \bar{y}_d)$
Nitrogen	11.6	11.8	11.7	11.8	12.8
Oxygen	10.6	10.3	10.5	10.3	11.8
Neon	11.8	11.4	11.3	11.4	13.0
Silicon	12.6	10.5	10.5	10.4	12.7

For nitrogen, oxygen and neon, all methods of determining the quality factor are in good agreement with recommendations of ICRP Publication 60, within four percent, except for the use of $\bar{y}_d$, which is within ten percent. For the much higher

energy silicon, $\bar{y}_f$ estimates quality within about twenty percent of the ICRP60 suggestion, while $\bar{y}_d$ gives a quality within six percent. This trend is shown graphically in Fig.5.11 by plotting the ratios of $\bar{y}_f$ and $\bar{y}_d$ to LET, as a function of ion energy.

Combining this data with past studies of TEPC response for iron, the trend seen in the ratios of $\bar{y}_f$ and $\bar{y}_d$ to LET as a function of energy does not hold. Plotting the ratios as a function of the momentum of the ion, however, fits the combined data as shown in Fig.5.12. Once again, $\bar{y}_f$ is a better predictor of quality when ion momentum is low and $\bar{y}_d$ is more accurate for larger momentum ions. $\bar{y}_f$, however, diverges from LET much faster than $\bar{y}_d$ as the momentum of the ion increases. In all cases, $\bar{y}_d$ remains within 10 percent of LET.

Dose Equivalent

Absorbed dose, D, delivered to the TEPC per unit fluence was calculated by integrating the response functions, based on energy deposited, and dividing by the mass of a one micrometer diameter sphere of tissue. Since the response functions are normalized to unity, determination of dose in this manner represents the dose delivered to a one micrometer volume of tissue per unit fluence. These numbers were numerically equal to a determination of the specific energy, z, based on $\bar{y}_f$ from the distribution of lineal energy. (see Chapter *Terms and Quantities*).

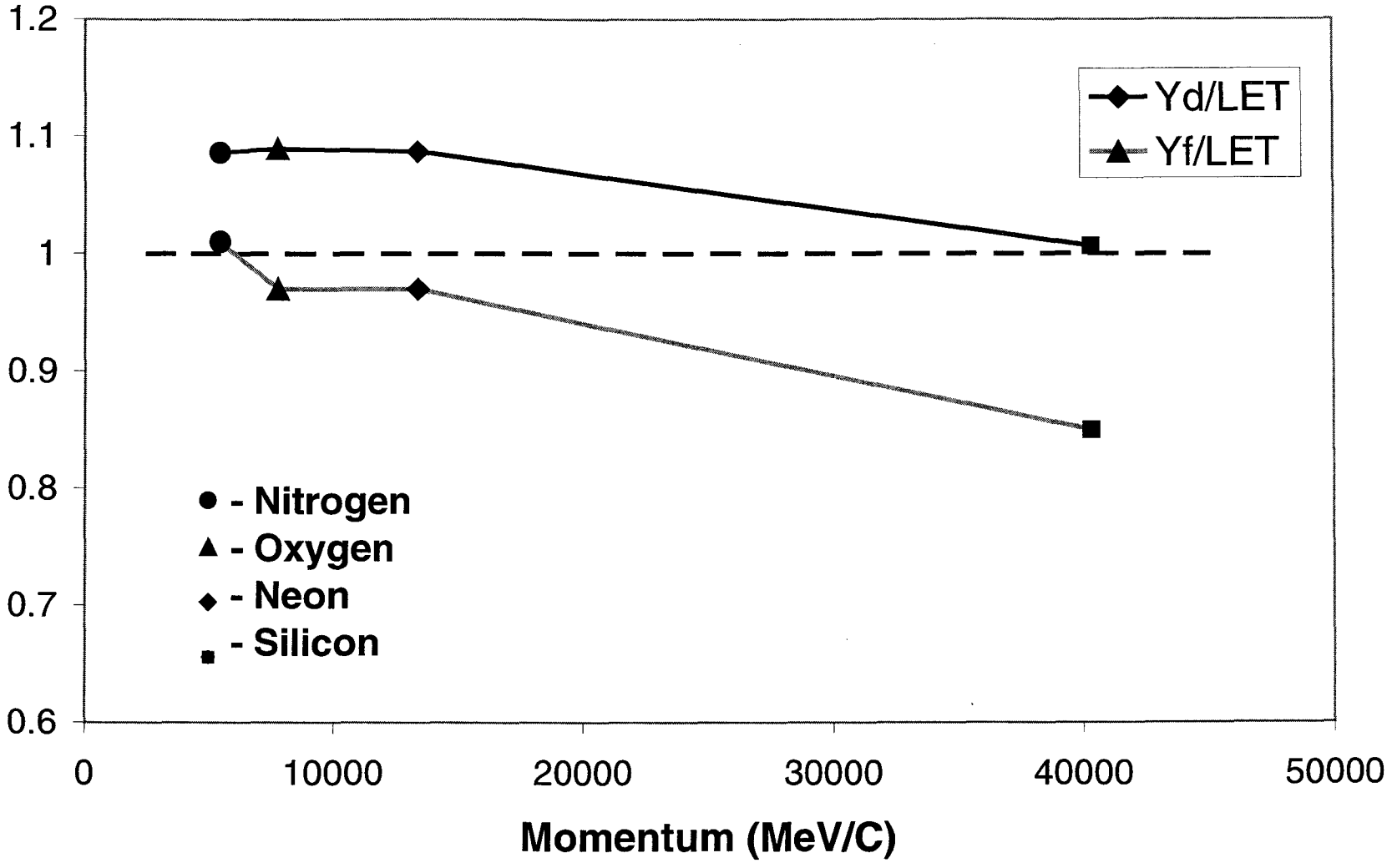

Fig. 5.11. Ratios of $\bar{y}_f$ and $\bar{y}_d$ to LET for each of the four ions as a function of momentum. For ions having a lower associated momentum $\bar{y}_f$ is a closer approximate to LET while $\bar{y}_d$ is a better predictor for higher momentum ions. The horizontal dashed line representing a ratio of 1.0 is plotted for reference.

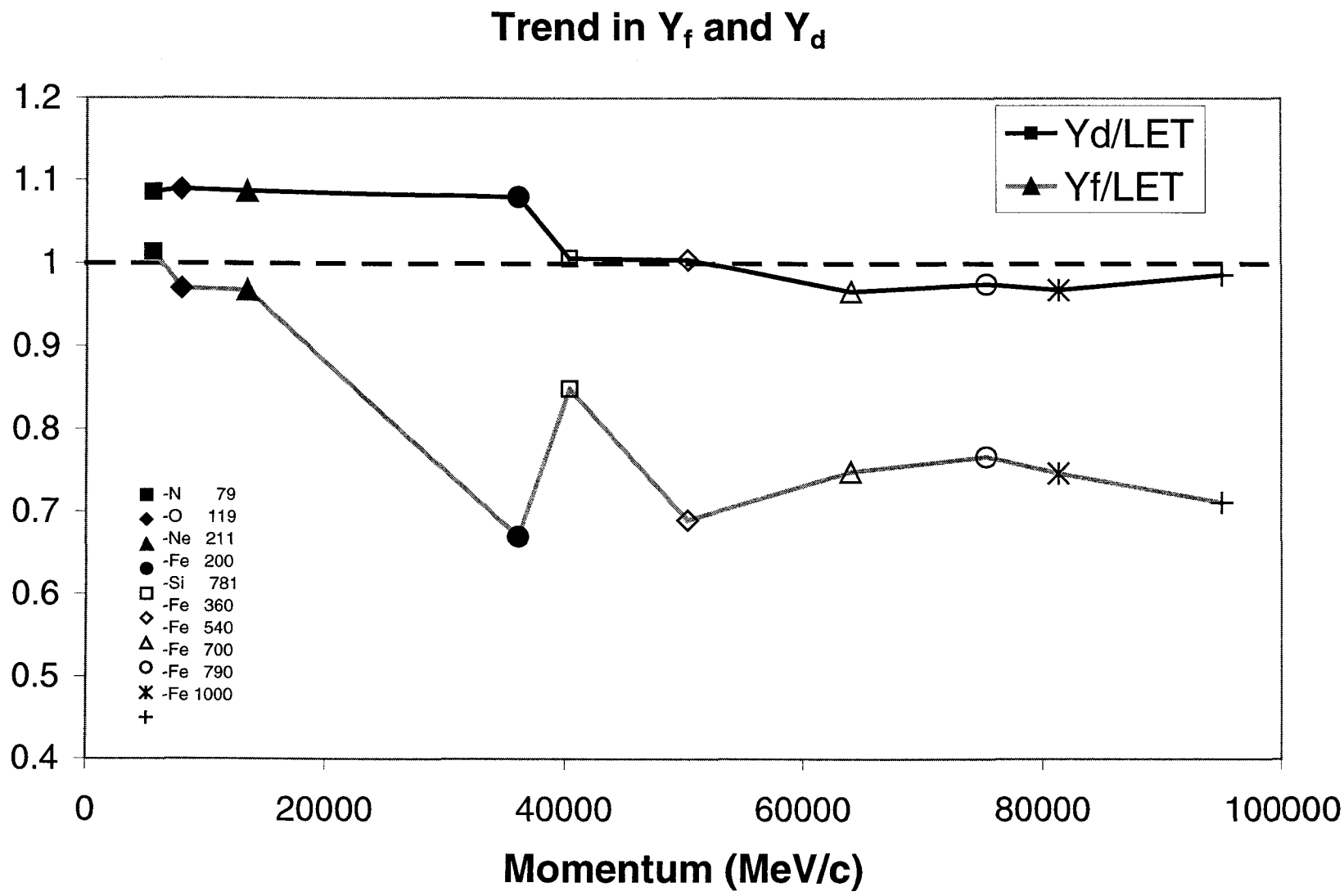

Fig. 5.12. Ratios of $\bar{y}_f$ and $\bar{y}_d$ to LET as a Function of Ion Momentum Combined with ^{56}Fe Data From Previous Work. The trend in $\bar{y}_f$/LET and $\bar{y}_d$/LET holds with the exception of ^{56}Fe having an energy of 200 MeV/nucleon, and possibly ^{56}Fe with an energy of 360 MeV/nucleon. The inset in the lower left corner of the graph gives the ion energy in MeV/nucleon along with its associated symbol. The horizontal dashed line representing a ratio of 1.0 is plotted for reference.

Multiplication by the quality, Q, gives dose equivalent, H, in Sieverts. Table-5.7 lists the dose to tissue for the four ions, followed by the dose equivalent. Radiation quality was determined by the ICRP60 recommendations based on LET, $\bar{y}_f$ and $\bar{y}_d$.

Table-5.7

Determination of Dose Equivalent

Ion	Dose to 1 μm Tissue (Gy)	Dose Equivalent (Sv)		
		Using Q(LET)	Using Q(LET = $\bar{y}_f$)	Using Q(LET = $\bar{y}_d$)
Nitrogen	8.91	103.4	105.1	114.5
Oxygen	7.98	87.8	83.8	94.2
Neon	8.65	102.1	98.6	112.5
Silicon	8.04	101.3	83.6	102.1

As can be seen from Table-5.7, since $\bar{y}_f$ more closely approximates the ICRP recommended method for determining Q for the first three ions, dose equivalent, H, is also more accurate. Errors in quality and dose equivalent were calculated using $\bar{y}_f$ to determine Q and H for nitrogen, oxygen and neon, and $\bar{y}_d$ for silicon, and are presented in Table-5.8. Since the standard errors associated with the summary statistics were low due to the high number of counts, the respective errors in Q and H were also low.

Table-5.8

Errors Associated with the Determination of Quality and Dose Equivalent

Ion	Error in Dose (Gy)	Error In Quality (ICRP Method, based on $\bar{y}_f$)	Error In Dose Equivalent (Sv)
Nitrogen	0.0043	0.0067	0.0784
Oxygen	0.0049	0.0077	0.0800
Neon	0.0051	0.0080	0.0904
Silicon	0.0045	0.0070	0.0775

CHAPTER VI - CONCLUSIONS

In radiobiological studies, variations in RBE have been shown to exist for heavy charged particles having similar LET. Track structure calculations show that the radial extent of energy deposition is different for similar LET particles having different charge and velocity. In this study, the fraction of energy lost by the incident particle that escapes the detector volume was seen to be larger in relation to the velocity of the ion studied.

However, due to the construction of the TEPC used in this study, similar to those used in the active dosimetry of manned space missions, as well as those used to characterize high-energy therapy beams, the measured energy deposition distributions are very similar for ions having similar LET. Though a greater fraction of energy liberated by ions having larger track volumes escapes the detector, the means of the distributions are similar. Simulation of detector response confirms that although the TEPC measures only a fraction of energy liberated by charged particles crossing the sensitive volume, an enhanced production of electrons in the dense wall of the detector gives back much of the energy lost.

Particles that passed through the center of the detector deposited only about 80% of the energy expected from LET times the diameter. The decrease was attributed to high-energy delta rays escaping from the sensitive volume. The radial dose model indicated that the energy escape from delta rays would result in only about 60% of the LET being deposited by particles passing through the center of the sphere. The difference between the data and calculation was attributed to forward moving electrons produced in the front wall of the detector. This forward contribution of electrons was not sufficient to compensate for the electrons escaping the sensitive volume. However, energy compensation from the wall exceeds energy loss from the gas when the impact parameter is greater than about 85% of the radius. It was shown that for a uniform fluence of particles at 800 MeV/nucleon, the measured distribution of energy deposition, $f(\varepsilon)$, could be reproduced computationally using the radial dose model if energy deposition for tracks passing through the sphere were enhanced by 35% and events that did not pass through the sphere were not enhanced at all.

Four ions were recorded, all having an LET within six percent of a mean value of 43.6 keV/μm. Due to the large number of counts contained within the measured distributions, the standard error of summary statistics $\bar{y}_f$ and $\bar{y}_d$, were very small. Values of the frequency mean lineal energies, $\bar{y}_f$, of the four ions were all within six percent of a mean value of 41.2 keV/μm. The dose mean lineal energies were within about five percent of an average of 46.3 keV/μm.

For all ions except the higher energy silicon, $\bar{y}_f$ was within four percent of the calculated LET of the ion, and $\bar{y}_d$ was within nine percent. The frequency mean of

silicon was within fifteen percent of the LET of the ion, while the dose mean lineal energy was within one percent. Thus, while $\bar{y}_f$ diverged from the calculated LET by as much as fifteen percent, $\bar{y}_d$ remained within ten percent of LET for all ions. It is interesting to note, however, that one standard deviation of either $\bar{y}_f$ or $\bar{y}_d$ for any ion includes the respective LET of the ion, and the average LET of all four, 43.5 keV/μm.

REFERENCES

1. F. Verhaegen, H. Palmans, Microdosimetric Characterization of Clinical Proton Beams, *Microdosimetry, an Interdisciplinary approach*, Edited by: D.T. Goodhead, P. O'Neill and H.G. Menzel (Royal Society of Chemistry, Cambridge, UK), (1997).

2. National Council on Radiation Protection and Measurements, Guidance on Radiation Received in Space Activities, NCRP Report 98, Bethesda, MD (1989).

3. National Council on Radiation Protection and Measurements, Radiation Protecrtion Guidance for Activities in Low-Earth-Orbit, NCRP Report 132, Bethesda, MD (2000).

4. J.E. Turner, *Atoms Radiation and Radiation Protection*, 2d ed., p. 145, John Wiley & Sons, New York, (1995).

5. F.H. Attix, *Introduction to Radiological Physics and Radiaion Dosimetry*, John Wiley & Sons, New York (1986).

6. International Commission of Radiation Units and Measurements, Linear Energy Transfer, ICRU Report 16, Washington, D.C. (1970).

7. National Council on Radiation Protection and Measurements, The Relative Biological Effectiveness of Radiations of Different Quality, NCRP Report 104, p. 4, Bethesda, MD (1990).

8. E.J. Hall, *Radiobiology for the Radiologist*, 4th ed., Chapt. 9, Lippincott-Raven, New York, NY (1994).

9. A.J. Waker, Principles of Experimental Microdosimetry, Rad.Prot.Dos., Vol. 61, No. 4, pp. 297-308 (1995).

10. B. Coutrakon, J. Cortese, A. Ghebremedhin, J.Hubbard, J. Johanning, P. Koss, G. Maudsley, C.R.. Slater, C. Zuccarelli, Microdosimetry Spectra of the Loma Linda Proton Beam and Relative Biological Effectiveness Cmparisons, *Med. Phys.* **24**(8) (1997).

11. G.D. Badhwar, The Radiation Environment in Low-Earth Orbit. *Radiat. Res.* **148** (Suppl.), S3-S10 (1997).

12. G.D. Badhwar, F.A. Cucinotta, L.A. Braby, A.Konradi, Measurements on the Shuttle of the LET Spectra of Galactic Cosmic Radiation and Comparison with the Radiation Transport Mode. *Radiat Res.* **139**, 344-351 (1994).

13. G.D. Badhwar, A. Konradi, A. Hardy, L.A.Braby, Active Dosimetric Measurements on Shuttle Flights., *Nucl. Tracks Radiat. Meas.* **20**, 13-20 (1992).

14. A.S. Johnson, G.D. Badhwar, M.H. Golighty, A.C., Hardy, A. Konradi, T. Yang, Spaceflight Radiation Health Program at the Lyndon B. Johnson Space Center, NASA Technical Memorandum 104782, 1993.

15. G.F. Knoll, Radiation Detection and Measurement, 2d Edition, John Wiley and Sons, New York, pp. 106-172 (1989).

16. B.B. Gersey, T.B. Borak, S. Guetersloh, C. Zeitlin, J. Miller, L. Heilbronn, T. Murakami, Y. Iwata, The Response of a Spherical Tissue-Equivalent Proportional Counter to ^{56}Fe Particles from 200-1000 MeV/nucleon., *Rad. Res.* **157**, 350-360, (2002).

17. S. Rademacher, T.B. Borak, C. Zeitlin, L. Heilbronn, J. Miller, Wall Effects Observed in Tissue-Equivalent Proportional counters from 1.05 GeV/nucleon Iron-56 Particles. *Rad. Res.* **149**, 387-395 (1998).

18. A. Chatterjee, H.J. Schaefer, Microdosimetric Structure of Heavy Ion Tracks in Tissue, *Rad. and Environm. Biophys.*, **13**, 215-227 (1976).

19. F.A. Cucinotta, R. Katz, J.W. Wilosn, R.R. Dubey, Heavy Ion Track-Structure calculations for Radial dose in Arbitrary Materials, NASA Technical Paper 3497 (1995).

20. H. Nikjoo, I.K. Khvostunov, F.A. Cucinotta, The Response of Tissue-Equivalent Proportional Counters to Heavy Ions, *Rad. Res.*, **157**, 435-445 (2002).

21. International Commission on Radiological Protection, Report 60, 1990 Recommendations of the International Commission of Radiation Protection, Annals of the ICRP, 21, (1991).

22. R.E. Zirkle, D.R. Marchbank, K.D. Kuck, Exponential and sigmoid survival curves resulting from alpha and X irradiation of *Aspergillus* spores., *J. Cell. Comp. Physiol. Suppl. 1*, **39**, 75-85 (1952).

23. R.E. Zirkle, General Features of Radiobiological Actions, *Phys. Rev.*, **31**, 1 (1959).

24. Y.S. Kim, Density Effect in dE/dx of Fast Charged Particles Traversing Various Biological Materials, *Rad. Res.*, **56**, 21-27 (1973).

25. H.E. Johns, J.R. Cunningham, *The Physics of Radiology*, 4th Edition, Charles C. Thomas, Springfield, IL (1983).

26. D.T. Goodhead, M. Belli, A.J. Mill, D.A. Bance, L.A. Allen, S.C. Hall, F. Ianzini, G. Simone, D.L. Stevens, A. Stretch, M.A. Tabocchini, R.A. Wilkinson, Direct Comparison Between Protons and Alpha Particles at the Same LET, I., Irradiation Methods and Inactivation of Synchronous V79, HeLa and C3H10T1/2 Cells, *Int. J. Radiat. Biol.*, **61**, 611-624 (1992).

27. M. Durante, L. Cella, Y. Furusawa, K. George, G. Gialanella, G. Gross, M. Pugliese, M. Saito, T.C. Yang, The Effect of Track Structure on the Induction of Chromosomal Aberrations in Murine Cells, *Int. J. Radiat. Biol.*, **73**/3. 253-262 (1998).

28. Y. Furusawa, K. Fukutsu, M. Aoki, H. Itsukaichi, K. Eguchi-Kasai, H. Ohara, F. Yatagai, T. Kanai, K. Ando, Inactivation of Aerobic and Hypoxic Cells from Three Different Cell Lines by Accelerated ^{3}He-, ^{12}C-, and ^{20}Ne-ion Beams, *Rad. Res.*, **154**, 485-496 (2000).

29. G. Kraft, Radiobiological Effects of Very Heavy Ions: Inactivation, Induction of Chromosome Abberations and Strand Breaks, *Nuclear Science Applications*, **3**, 1-28 (1987).

30. J.J. Butts, R. Katz, Theory of RBE for Heavy Ion Bombardment of Dry Enzymes and Viruses., *Radiat. Res.*, **30**, 4, 855-871 (1967).

31. E.H. Goodwin, S.M. Bailey, D.J. Chen, M.N. Cornforth, The Effect of Track Structure on Cell Inactivation and Chromosome Damage at a Constant LET of 120 keV/μm, Advances in Space Research, **18**, 93-98 (1996).

32. International Commission on Radiological Protection and International commission on Radiation Units and Measurements, *Report of the RBE Committee to the International commissions on Radiological Protection and on Radiological Units and Measurements*, *Health Phys.*, **9**, 357-384 (1963).

33. International Commission on Radiation Units and Measurements, *The Quality Factor in Radiation Protection*, ICRU Report 40, Bethesda, MD (1986).

34. Rossi, H. H., Zaider, M., *Micordosimetry and its Applications*, Springer-Verlag, New York (1996).

35. A.M. Kellerer, D. Chmelevsky, Criteria for the Applicability of LET, *Rad. Res.*, **63**, 226-234 (1975).

36. International Commission on Radiation Units and Measurements, *Microdosimetry*, ICRU Report 36, Bethesda, MD (1983).

37. A.M. Kellerer, K. Hahn, The Quality Factor for Neutrons in Radiation Protection: Physical Parameters, *Radiat. Prot. Dos.*, **23**, 1/4, 73-78 (1988).

38. M. Scholtz, G. Kraft, Track Structure and the Calculation of Biological Effects of heavy Charged Particles, *Adv. Space Res.*, **18**, 1/2, 5-14 (1996).

39. M.E. Rudd, User-Friendly Model for the Energy Distribution of Electrons From Proton or Electron Collisions. Nucl. Tracks Radiat. Meas., **16**, 2/3, 213-218 (1989).

40. E.J. Kobetich, R. Katz, Electron Energy Dissipation., *Nucl. Instrum. Methods*, **71**/2, 226-230 (1969).

41. H.H. Rossi, W. Rosenzweig, A Device for the Measurement of Dose as a Function of Specific Ionization., Radiology, **64**, 404-411 (1955).

42. International Commission on Radiation Units and Measurements, *Quantitative Concepts and Dosimetry in Radiobiology*, ICRU Report 30, Bethesda, MD, (1979a).

43. International Commission on Radiation Units and Measurements, *Tissue Substitutes in Radiation Dosimetry and Measurement*, ICRU Report 44, Bethesda, MD, (1989).

44. A.M. Kellerer, An Assessment of Wall Effects in Microdosimetric Measurements, *Rad. Res.*, **47**, 377-386 (1971).

45. W.A. Glass, L.A. Braby, A Wall-Less Detector for Measuring Energy Deposition Spectra, *Rad. Res.*, **39**, 230-240 (1969).

46. W. Gross, B.J. Biavati, H.H. Rossi, Microdosimetry of Directly Ionizing Particles with Wall-less Proportional Counters, Proceedings of the Second Symposium on Microdosimetry (1970).

47. R.C. Rogers, J.F. Dicello, W. Gross, The Biophysical Properties of 3.9 GeV Nitrogen Ions - II. Microdosimetry, *Rad. Res.*, **54**, 12 (1973).

48. J.L. Humm, J. Booz, An Anomaly in the Performance of Spherical Proportional Counters for Microdosimetry, *Radiat. Prot. Biol.*, **15**, 1, 9-14 (1986).

49. A.M. Kellerer, Fundamentals of Microdosimetry, The Dosimetry of Ionizing Radiation, Vol. 1, pp. (?) (1985).

50. A.M. Kellerer, Mikrodosimetrie, Grundlagen einer Theorie der Strahlungsqualität, Gesellschaft fur Strahlenforschung GSF Ser. Monogr., Munich, (1968).

51. R.J. Larsen, M.L. Marx, *An Introduction to Mathematical Statistics and its Applications*, 2d Ed., Prentice-Hall, New Jersey (1986).

52. Y. Hirao, H. Ogawa, S. Yamada, Y. Sato, T. Yamada, K. Sato, A. Itano, M. Kanazawa, K. Noda, S. Matsumoto, Heavy ion synchrotron for medical use—HIMAC project at NIRS-JAPAN, *Nucl. Phys. A.* **538**, 542–550 (1992).

53. P. Kliauga, A.J. Waker, J. Barthe, Design of Tissue-Equivalent Proportional Counters, Rad.Prot.Dos., Vol 61, No. 4, pp. 309-322 (1995).

54. P. Segur, P. Olko, P. Colauti, P. Numerical Modelling of Tissue-Equivalent Proportional Counters, Rad.Prot.Dos., Vol. 61, No. 4, pp.323-350 (1995).

55. Physical Reference Data, National Institute for Standards and Measurement, http://physics.nist.gov/PhysRefData/contents.html.

56. Far-West Technologies, Inc., 330 South Kellogg Ave., Goleta, CA 93117.

57. R.F. Shonka, J.E. Rose, G. Failla, Conducting Plastic Equivalent to Tissue, Ion and Polystyrene, 2d United Nations International Conference on Peaceful Uses of Atomic Energy, **21**:184, (1958).

58. C. Zeitlin, J. Miller, L. Heilbronn, K. Frankel, W. Gong, W. Schimmerling, The Fragmentation of 510 MeV/Nucleon Iron-56 in Polyethylene., I. Fragment Fluence Spectra, *Rad. Res.* **145**, 655-665, (1996).

59. F.A. Cucinotta, R. Katz, J.W. Wilson, L.W. Townsend, J. Shinn, F. Hajnal, Biological Effectiveness of High-Energy Protons: Target Fragmentation, Rad. Res. **127**, 130-137 (1991).

60. M. Wong, W. Schimmerling, W.M. Phillips, B.A. Ludewigt, D.A. Landis, J.T. Walton, S.B. Curtis, The multiple Coulomb scattering of very heavy charged particles, *Med. Phys.* **17**, 163-171 (1990).

61. C. Zeitlin, K.A. Frankel, W. Gong, L. Heilbronn, E.J. Lampo, R. Leries, J. Miller, W. Schimmerling, A Modular Solid State Detector for Measuring High energy Heavy Ion Fragmentation near the Beam Axis, Rad. Meas. **23**(1), 65-81 (1994).

62. C. Zeitlin, L. Heilbronn, J. Miller, Detailed Characterization of the 1087 MeV/nucleon ^{56}Fe Beam Used for Radiobiology at the AGS, Lawrence Berkeley National Laboratory, LBL-39267/UC-000 (1997).

63. C. Zeitlin, L. Heilbronn, J. Miller, S.E. Rademacher, T.B Borak, T.R. Carter, K.A. Frankel, W. Schimmerling, C.E. Stronach, Heavy fragment production cross sections from 1.05 GeV/nucleon 56 Fe in C, Al, Cu, Pb and Ch2 targets, Phys.Rev.C **56**(1), 388-397 (1997).

64. P.L. Chapman, in *Applications of Probability and Statistics in Health Physics*, Edited by T. Borak, Medical Physics Publishing, WI, (2000).

65. EG&G ORTEC, 100 Midland Rd., Oak Ridge, TN 37830.

66. Hytec Electronics, LTD., 5 Cradock Road, Reading, Berkshire, RG2 0JT, England.

67. R.J. Larsen, M.L. Marx, *An Introduction to Mathematical Statistics and Its Applications*, 2d. Ed., Prentice-Hall, New Jersey, (1986).

68. W.J. Conover, *Practical Nonparametric Statistics*, John Wiley & Sons, New York, (1971).

69. The data analysis for this paper was generated using SAS software. Copyright, SAS Institute Inc. SAS and all other SAS Institute Inc. product or service names are registered trademarks or trademarks of SAS Institute Inc., Cary, NC, USA

70. G. Dietze, H.G. Menzel, G. Buhler, Calibration of Tissue-Equivalent Proportional Counters used as Radiation Protection Dosemeters, *Rad. Prot. Dos.*, **9**/3, 245-249 (1984).

71. T.A. Kniss, F.L. Glesius, A Method for Calibration of Cylindrical Tissue Equivalent Proportional Counters, *Transactions on Nuclear Science*, **33**, no. 1 (1986).

72. D. Srdoc, Experimental Technique of Measurement of Microscopic Energy distribution in Irradiated Matter Using Rossi Counters, *Rad. Res.*, **43**, 302-319 (1970).

73. U.J. Schrewe, H.J. Brede, P. Pihet, H.G. Menzel, On the Calibration of Tissue-Equivalent Proportional Counters with Built-in α Particle Sources, *Rad. Prot. Dos.*, **23**, 1/4, 249-252 (1988).

74. M.N. Varma, Calibration of Proportional Counters in Microdosimetry, Proceedings of the 8th Symposium on Microdosimetry, EUR 8395, London, Harwood Academic, London, 1051-1059, (1983).

75. H.G. Menzel, G. Buhler, H. Schuhmacher, Investigation of Basic Uncertanties in the Experimental Determination of Microdosimetric Data, Proceedings of the 8th Symposium on Microdosimetry, EUR 8395, Harwood Academic, London, 1061-1072 (1983).

76. American Institute of Physics Handbook, 2d Ed., McGraw-Hill, New York, (1963).

77. E. Anachkova, A.M. Kellerer, H. Roos, Calibrating and Testing Tissuue Equivalent Proportional Counters with ^{37}Ar, *Radiat. Environ. Biophys.*, **33**, 353-364 (1994).

78. A. Chatterjeee, H.D. MaCabee, C.A. Tobias, Radial Cutoff LET and Radial Cutoff Dose calculations for Heavy Charged Particles in Water, *Rad. Res.*, **54**, 479-494 (1973).

79. L.H. Toburen. W.E. Wilson, Energy and Angular Distributions of Electrons Ejected from Water Vapor by 0.3-1.5 MeV Protons, *J. Chem. Phys.*, **66**/11, 5202-5213 (1977).

80. S. Schmidt, C. Kelbch, H. Schmidt-Bocking, G. Kraft, Delta-Electron Emission in Heavy Ion Collisions, Terrestrial Space Radiation and its Biological Effects, Percival D. McCormack, Charles E. Swenberg, and Hurst Bucker, eds., Plenum Press, 205-212 (1988).

81. M.E. Rudd, L.H. Toburen, N. Stolterfoht, Differential Cross Sections for Ejection of Electrons From Helium by Protons, *Atomic Data and Nuclear Data Tables*, **18**/5 413-432 (1976).

82. L.H. Toburen, Distribution in Energy and Angle of Electrons Ejected From Xenon by 0.3-2.0 MeV Protons, *Phys. Rev. A*, **9**/6, 2505-2517 (1974).

83. W.E. Wilson, H. Nikjoo, PITS: A code set for positive ion track structure, *Computational Approaches in Molecular Radiation Biology, Monte Carlo Methods*, M.N. Varma, A. Chatterjee, eds., Plenum Press, 137-153 (1994).

84. International Commission on Radiation Units and Measurements, *Stopping Powers and Ranges for Protons and Alpha Particles*, ICRU Report 49, Bethesda, MD (1993).

APPENDIX A

LINEAR ENERGY TRANSFER

The term Linear Energy Transfer (LET) was introduced by Zirkle, et.al., (1952) to explain the energy lost by a charged particle passing through a medium.[22,23] Charged particles traversing matter lose energy either by inelastic nuclear collision, or, more predominantly, by Coulomb interaction with the electrons of the target medium. In the latter process, the Coulomb electric force field surrounding the charged particle interacts with one or more of the orbital electrons of the target atoms causing excitations or ionizations.[5]

Charged particles lose energy in random interactions. The LET of a particle is the expectation value of the rate of energy loss per unit distance traveled by a particle in a specific medium, or dE/dx, in interactions with orbital electrons. [36] It is typically referred to as the stopping power of the particle in the given medium, and has units of MeV/cm or keV/μm. Dividing the stopping power by the density, ρ, of the target medium gives a quantity called the mass stopping power, which is usually given in units of MeV-cm^2/g and is useful in determining the stopping power of a particle passing through a medium composed of more than one element.

A theoretical expression for mass stopping power has been derived by Bohr, Bethe and Bloch to explain charged particles.[24] It is dependent upon the charge and velocity of the projectile and the atomic number and atomic weight of the target medium[5] , and is given by the following relation:

$$\left(\frac{dE}{\rho dx}\right) = 0.307 \frac{z}{A} \frac{Z^2}{\beta^2} \left[13.8373 + \ln\left(\frac{\beta^2}{1-\beta^2}\right) - \beta^2 - \ln(I) \right] \qquad \text{Equation A.1}$$

where:

ρ = density of the target medium,
I = mean excitation potential of the target medium,
A = atomic weight of the medium,
z = atomic number of the medium (charge),
Z = charge of the projectile, and
β = velocity of the projectile with respect to the speed of light, C.

Frequently it is important to determine the stopping power of a charged particle interacting with a medium composed of more than one element. The mass stopping powers of each constituent is first determined and multiplied by the weight fraction of each element in the compound F_i, as given in Equation A.2. To determine the stopping power of the particle in that medium, the total mass stopping power is multiplied by the density of the compound.[4]

$$\left(\frac{dE}{\rho dx}\right)_T = \sum_{i=1}^{n}\left(\frac{dE}{\rho dx}\right)_i \qquad \text{Equation A.2}$$

When studying the rate of energy loss for different charged particles interacting with the same medium, variables describing the medium, ρ, z, A and I, become constants. The expression is then dependent only upon the characteristics of the projectile, Z^2/β^2. Fig.A.1 shows stopping power as a function of Z^2/β^2 for oxygen and silicon. As can be seen in the plot, for a given value of the stopping powers of the particles are not exact, but very similar.

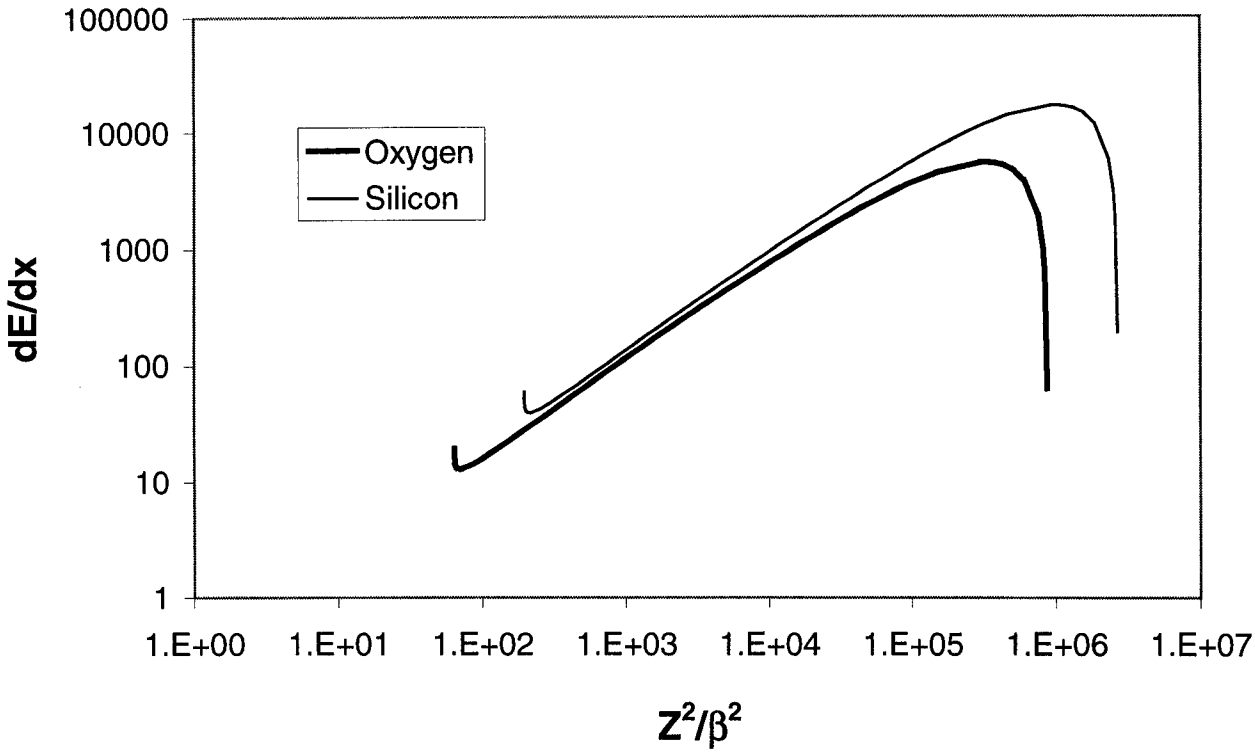

Fig.A.1. Stopping Power as a Function of Z^2/β^2. In the same medium the Beta-Bloch approximation to energy loss becomes dependent upon the ion charge and its velocity. For energies in the range of interest to radiation protection and radiation biology there is a region where equivalent ratios of the square of charge to velocity gives similar LET for different ions.

Choosing the LET of a particle to study in turn fixes the value of the square of the ratio of charge to velocity. Since the charge is unique for a given ion, choosing the velocity becomes the controlling factor in setting the LET of the particle. To find the energy of the beam to give the chosen LET requires a determination of the velocity with respect to the speed of light, β, by use of relativistic kinematics and is given by the relation:

$$\beta = \sqrt{1 - \left(\frac{M_0 C^2}{T + M_0 C^2} \right)^2} \qquad \text{Equation A.3}$$

where:

M_0C^2 = the rest mass of the projectile, in MeV, and
T = the kinetic energy of the projectile, in MeV.

Fig.A.2 shows the variation in stopping power as a function of β for the ions studied. The solid dots indicate the point at which each ion has the same LET. It is also important to note from this plot that care must be taken in the choice of LET studied. Choosing a stopping power less than 40 keV/μm precludes the study of silicon. No value of β exists that would give silicon this LET, except where the function is rapidly approaching zero at a very low velocity.

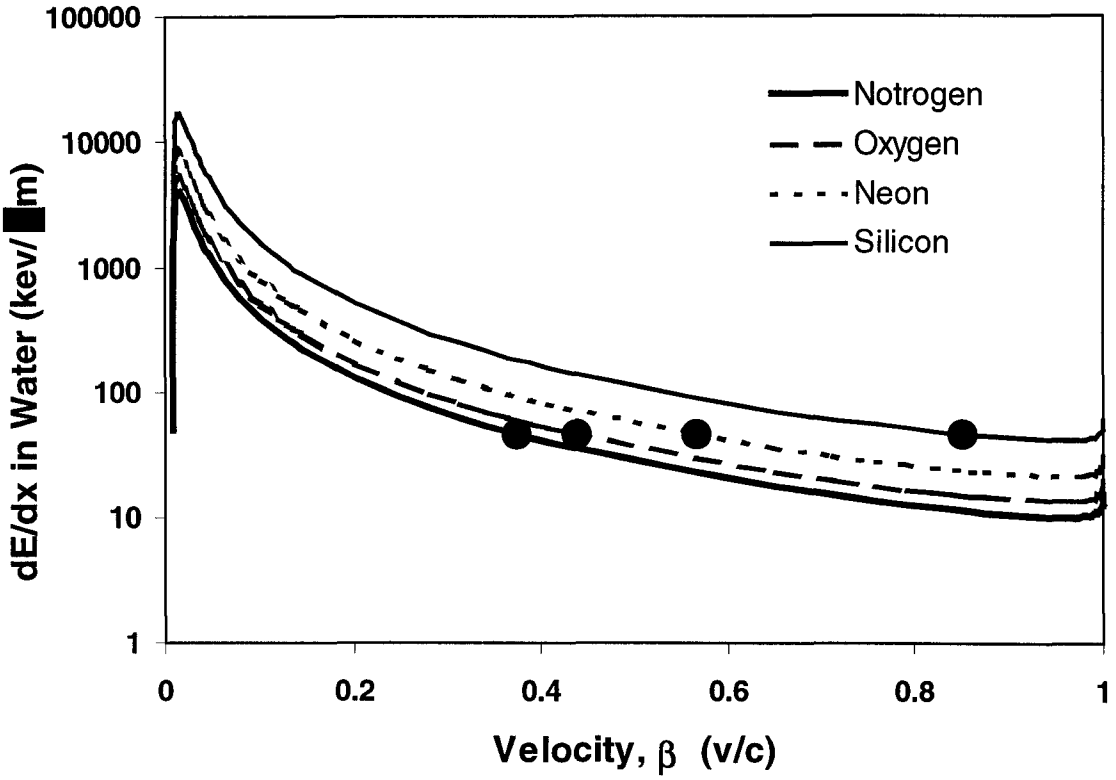

Fig.A.2. Stopping Power as a Function of Velocity (β). The Beta-Bloch formula for stopping power, dE/dx, is depicted as a function of velocity, β, for the four ions measured. The solid dots represent the point at which all ions have the same stopping power, in this case 45 kev/μm.

Table-A.1
Beta and Energies Required to give an LET of 45 keV/μm

Ion	Beta (v/c)	Energy Incident upon the Detector (Mev/nucleon)	Beam Exit Energy (Mev/nucleon)
Nitrogen	0.375	73	95
Oxygen	0.437	105	129
Neon	0.566	200	221
Silicon	0.851	830	841

The velocities of all four ions that would give an LET of 45 keV/μm are presented in Table-A.1. The energies, in MeV/nucleon, associated with this stopping power are shown in the second column. For a study of similar LET, the energies are chosen so that the stopping power is similar at the point of measurement. In many modern experiments, there are some components associated with the detection system located between the detector and the beam exit window. A calculation of energy loss in each of these components is therefore required to arrive at the beam exit energies giving the required stopping power at the point of measurement. Performing this calculation for the energies above gives beam exit energies shown in the last column.

The energies ordered at HIMAC were not exactly as listed in Table-A.1, however, but energies easily delivered at the facility. The LET of all particles were within 6.0 % of 43.5 keV/μm.

APPENDIX B

ENERGY CALIBRATION

Tissue Equivalent Proportional Counters used in microdosimetric studies measure the number of ions created in the sensitive volume of the detector by the passage of charged particle.[70] Volumes on the order of 10^{-18} cubic meters are simulated to achieve a relationship with the spatial patterns of energy deposition that would occur in biological tissue of similar dimensions.[9] In radiation protection dosimetry, the goal of calibration is to determine a factor that converts the measured pulse height spectra into a distribution of energy deposition events for later determinations of dose, radiation quality and dose equivalent.[71]

When accelerated charged particles interact with the TEPC fill gas and surrounding wall to form ionizations, electron-ion pairs are produced.[15] The electrons are multiplied in the electric field of the detector and collected on the anode. The corresponding charge collected is converted into a voltage pulse by the pre-amplifier. The amplifier then conditions and increases this pulse to be recorded in a specific channel of a pulse height analyzer. The recorded data is a distribution of voltages sent by the amplifier based on the number of original ion-pairs produced in the detector by a single traversing charged particle.[9]

Conversion of the recorded pulse height spectra into energy deposition requires the measurement of a quantity of radiation with a known energy deposition to measure the TEPC response.[48] Several methods have been discussed that use neutrons, alpha emitters and low energy photons.[70-73] Research pulsers are also used to verify the accuracy of the electronic system.[45] Since there are errors associated with each process,[74,75] more than a single method should be used to accurately determine TEPC and system response.

Neutron Calibration

Because they are uncharged, neutrons do not create ionizations in the sensitive volume of the TEPC. Secondary particles, primarily protons, are liberated when the neutron collides with the nucleus of the atoms that make up the dense surrounding wall of the detector. Some of the secondary protons ionize the fill-gas and surrounding wall, creating ion pairs that may be recorded. A representative pulse height distribution, on exposing a spherical TEPC to neutrons, is shown in Fig.B.1. The spectrum of neutron energies from the PuBe source results in the distribution of energy deposition primarily by proton recoils.

The sharp drop in number of events occurring between channels 150 and 200, the "proton edge", represents the point at which the energy deposited by a recoil proton is reaching its maximum. The location of the edge in the spectrum is dependent on TEPC geometry and cavity pressure. Particles with high LET and short trajectories produce voltage pulses similar to those from particles with lower LET and longer trajectories. This overlapping of event types having similar energy depositions gives rise to the slope of the proton edge seen in Fig.B.1. [71]

The point at which the number of counts approaches background is called the proton drop point.[71] The energy associated with this channel can be found by integrating the Beta-Bloch equation (Appendix A) in the region where the stopping power is a maximum, the Bragg-peak. Fig.B.2 is a plot of proton stopping power as a function of residual range. The vertical dashed lines show the region of maximum

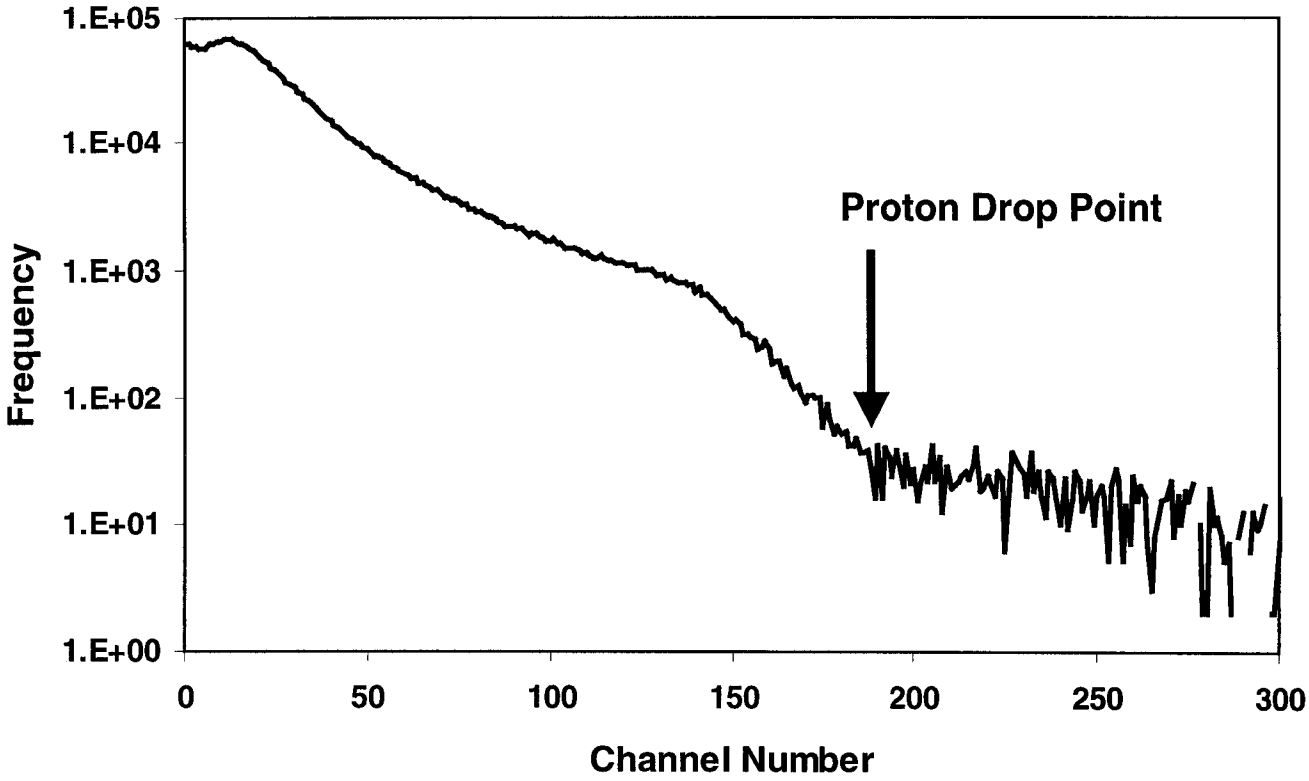

Fig.B.1. Neutron Calibration Spectra. Pulse height spectra of TEPC exposed to PuBe neutron source. The proton drop point represents the maximum energy that a proton can deposit in the detector. This energy is due to a proton having maximum LET, crossing the longest path of the detector volume. For a sphere, this is the diameter of the cavity.

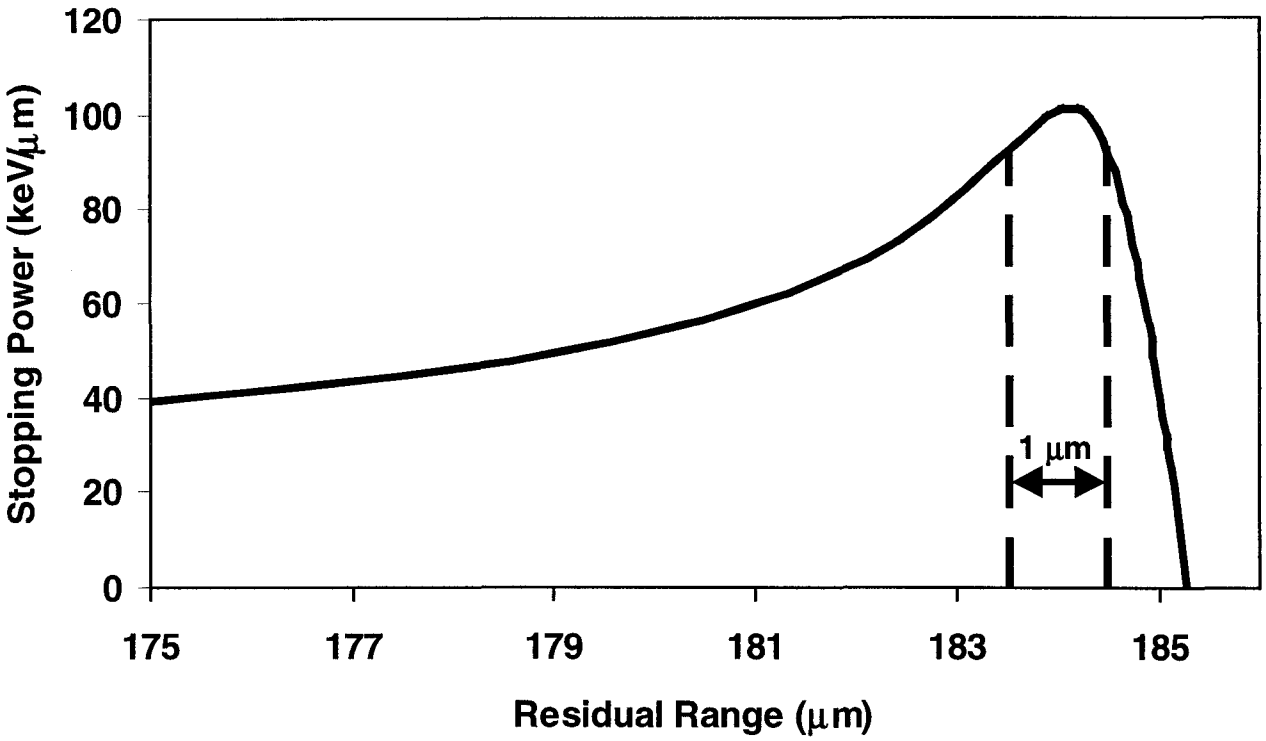

Fig.B.2. Proton Stopping Power in Water. The dashed vertical lines show the region encompassing the Bragg peak for a path of one micrometer where stopping power is maximized. Integrating the Bethe-Bloch equation in this region gives a maximum energy loss of 97.65 keV. This is the energy associated with the proton drop point measured by a spherical TEPC simulating a one micrometer diameter volume of tissue when exposed to neutrons.

energy deposition for a path of 1 μm. Thus for the example presented in Fig.B.1, a maximum energy deposition of 97.65 keV (Fig.B.2) occurs in about channel 185, giving a calibration factor of 0.528 keV per channel, under the conditions of measurement.

Alpha Calibration

Internally mounted alpha sources are a common calibration method offering an easy, fast and reproducible calibration.[73] Inverting the TEPC exposes a small bore hole in the rigid surrounding wall allowing the alpha particles to cross the sensitive volume.[70,73] With a known stopping power, and a known path length across the detector, the energy deposition is readily calculated. Though there are small uncertainties in alpha energy deposition in Tissue-equivalent gas as well as path length,[75] this method offers the advantage of having three energy deposition points.[73]

A typical pulse height distribution measured as a result of alpha particles emitted by an internally mounted ^{244}Cm source is shown in Fig.B.3 for a spherical 12.7 cm diameter TEPC. Peak B represents unscattered alpha particles traversing the cavity diameter.[73] The average energy deposition under this peak is simply the energy loss of the alpha particle for the distance traveled, LET times Δx. The 5 MeV alpha particle emitted by the ^{244}Cm source has an average energy deposition of 84.15 keV/μm.[76]

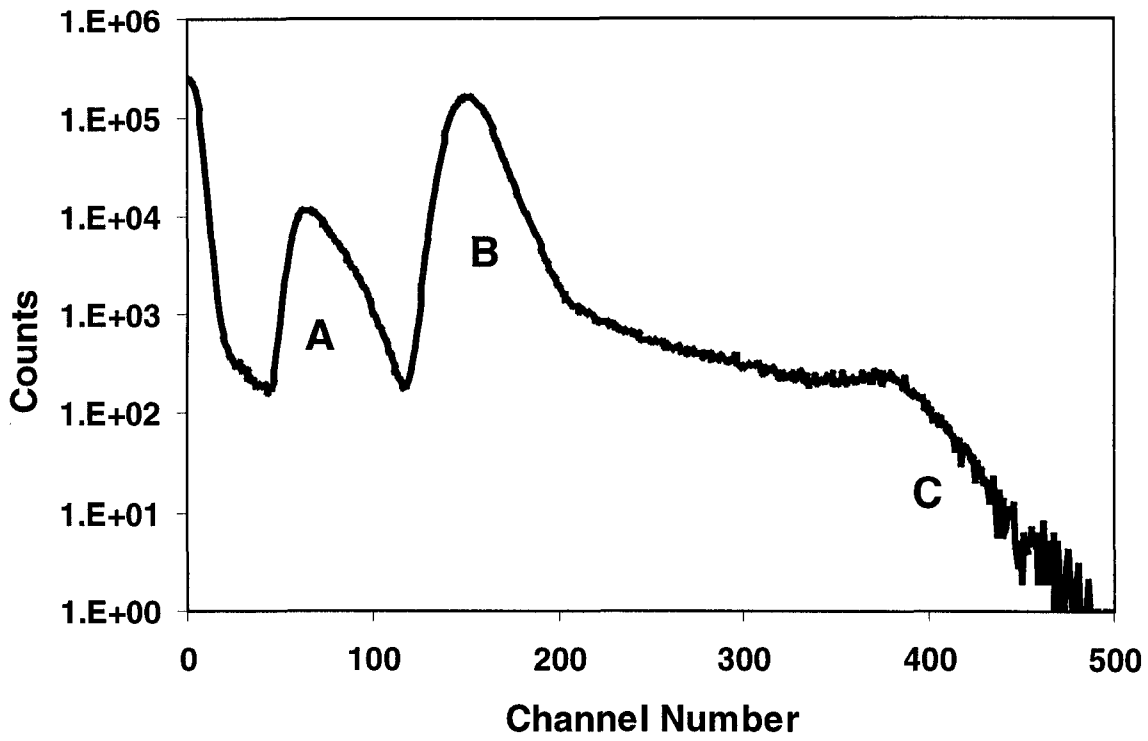

Fig.B.3. Alpha Calibration Spectra. Pulse height spectra from internally mounted ^{244}Cm source. Peak A is due to alpha particles stopped in the central anode of the TEPC. With path lengths half the diameter of the TEPC cavity, energy deposition is half that of the primary peak. Peak B represents alpha particles crossing the full diameter of the detector cavity. Simulating a one micrometer diameter volume of tissue, the average energy deposition under this peak is 84.15 keV from this source (LEt of 84.15 keV/

Simulating a volume of tissue having a 1 m diameter, the conditions of measurement of Fig.B.3, the energy deposition under peak B would therefore have an average value of 84.15 keV.

Peak A of Fig.B.3 is a result of unscattered alpha particles that are stopped in the central anode and surrounding helix wire of the detector.[73] Since the path traversed is about half the diameter of the cavity, the mean energy deposition associated with peak A corresponds to roughly half that of peak B, or 42.1 keV. Due to variations in path lengths for particles stopping in the anode compared with particles stopping in the helix wire, there is a larger error associated with the average energy deposition under peak A.

The sharp drop occurring at point C of Fig.B.3 represents the maximum energy that an alpha particle can deposit in the cavity of the detector. This alpha edge is caused by scattered alpha particles crossing the diameter of the cavity that are slowed down to energies such that their stopping power is maximized.[73] The energy deposition associated with these events is found in the same manner as discussed above in determining the proton edge for a neutron calibration, by integration, over the maximum path length, of the Beta-Bloch equation in the region of maximum stopping power.

X-ray Calibration

Calibration may also be carried out with X-ray sources as long as the X-ray energy is low enough that the range of the secondary electrons is much less than the simulated diameter of the TEPC cavity.[36] When X-rays interact with the counter gas they liberate electrons with known energies. The requirement that the range of these secondaries be much smaller than the effective diameter of the TEPC means that they are fully stopped in the detector volume, resulting in a distinct peak with a very small uncertainty.[48,70] One inconvenience associated with this type of calibration is that most methods require a modification of the detector and an external source.[48,70,77] Another problem is that they generally test only a part of the counter volume.[77]

It has been recommended by the International Commission on Radiation Units and Measurements, in Report 36, that for the measurement of low-LET radiations, soft x rays should be used to calibrate the detector thereby minimizing difference in W values between the radiation studied and the calibration source.[36] A simple method that avoids the problems discussed above is the incorporation of ^{37}Ar into the counter gas. 813 keV X-rays are emitted by the argon within the detector. Calibrations are therefore representative of the entire counter volume and no modification of the detector is required. Furthermore, it has been shown that mixtures containing a volumetric ratio of less than 0.01 ^{37}Ar do not affect the operation of the proportional counter.[77]

Experimental Method

The primary calibration method in this study entailed the use of an internally mounted alpha emitter in conjunction with an ORTEC Research Pulser. Since the study was based on the measurement of heavy charged particles, the internal alpha source afforded a quick, reproducible energy deposition with only a small difference in W value from that of the accelerated charged particle.[36]

The alpha source gave a correlation between known energy deposition events and the channel numbers corresponding to the charge that was collected. The research pulser provided a means to check the linearity of the pulse height analyzers, ensuring that the energy deposition by the alpha particle in a few channels could be related to energy depositions in all other channels.

Immediately after each experiment, a number of pulses at varying voltages were sent through the data acquisition system to determine linearity of the low-gain and high-gain pulse height analyzers. A linear regression of the data for each of the analyzers was preformed returning an equation relating the pulser setting as a function of the channel number recording the pulse. Fig.B.4 shows the results of this analysis.

The TEPC was then inverted so that the internal alpha calibration source could be measured under the same conditions. The mean value in the pulse height analyzer corresponding to the primary peak of the alpha spectrum was equated with the average energy deposition of the calibration source, 84.15 keV, as shown in Fig.B.2.

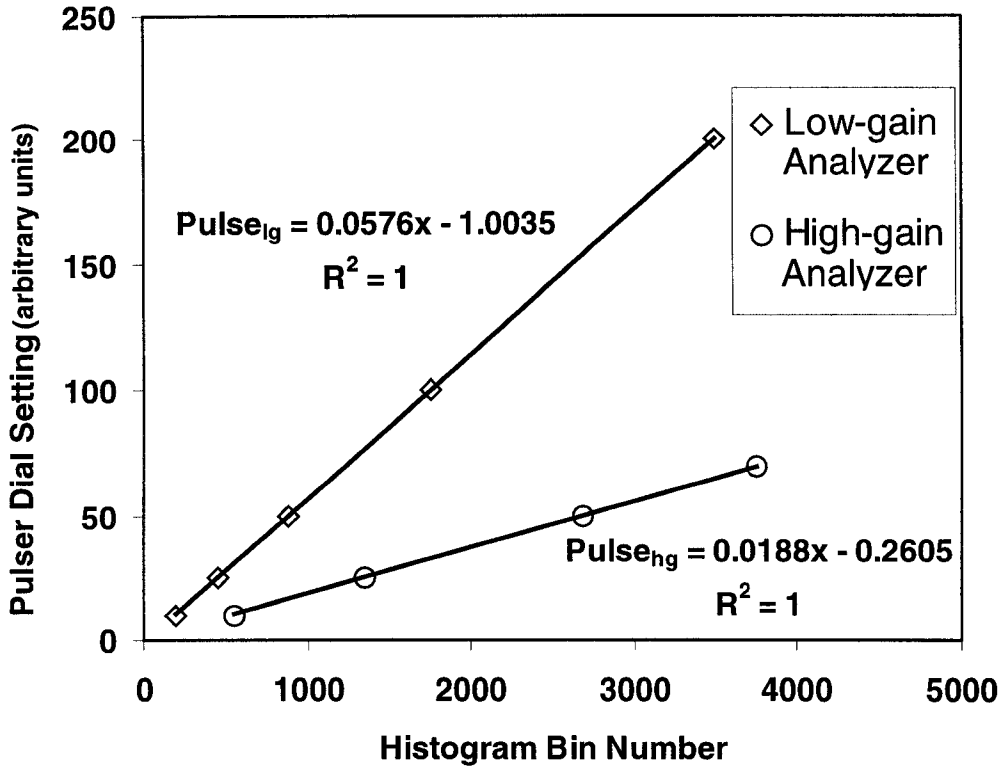

Fig.B.4. Pulsar setting as a function of histogram bin number. White diamonds represent pulsar settings associated with the low-gain ADC channel. White circles represent the bin that the same pulsar setting occurs in for the high-gain ADC. Both equations returned an R^2 of 1.0 showing linear response across the full scale of both ADCs.

For the calibration shown in Fig.B.1 the pulser settings giving rise to a voltage pulse at the mean value of the primary alpha peak for the low gain and high gain pulse height analyzers were 91.1 and 90.2, respectively. Dividing these pulser settings into the average energy deposited by the alpha particle gave the conversion factor, in keV per unit pulser setting, to be applied to the regression equation. For the low-gain ADC this value was 0.924 keV/pulser-setting, while the high-gain scaling factor was 0.933 keV/pulser-setting.

This process was repeated using the secondary peak of the alpha distribution shown in Fig.B.2. The mean energy deposition of 42.1 keV was equated with pulser settings of 45.7 for the low gain analyzer and 45.17 for the high gain analyzer. The scaling factors derived were 0.921 keV/pulser-setting for the low-gain analyzer and 0.932 for the high-gain, showing good agreement. The equations were transformed to keV as a function of channel number and applied to the each individual event.

APPENDIX C

TRACK STRUCTURE MODELING

The delta-ray theory of track structure attributes energy lost by a charged particle to the ejection of secondary electrons from the material the ion is passing through.[19] Calculations and models based on track structure have provided correct descriptions of a variety of phenomena associated with heavy ion irradiation. Experimental measurements of radial dose and energy loss through matter, as well as heavy ions response of physical detectors such as scintillators, thermoluminescence detectors and the Fricke dosimeter have been explained using track structure theory.[19] Recently, track structure has been used to explain the differences observed between measurements with walled and wall-less tissue equivalent proportional counters.[20]

Track Structure of Heavy Ions

To limit energy deposition in microscopic volumes in terms of geometry, instead of using energy restricted LET, Chatterjee, et. al., proposed a model to calculate energy deposition radially around the trajectory of a heavy charged particle in tissue.[78] Later revisions partitioned energy deposition into two distinct regions, an inner core and an outer penumbra.[18] Roughly half of the total energy loss by ionization was assigned to each region.

The core referred to a central region of dense energy deposition very close to the track of the ion. Energy deposited in this region was due primarily to the very low energy electrons with short or negligible range. All energy deposited by these

electrons, energies less than 1600 eV, was considered locally deposited. The radial distance, in nanometers, describing this dense region of energy deposition was given by:

$$R_c = 0.0116 \cdot \beta \qquad \text{Equation C.1}$$

Where: β = velocity of incident ion with respect to the speed of light (V/C).

The penumbra was the region outside of the core where energy deposition radially away from the track was described in relation to the inverse square of the distance normal to the ion trajectory. The maximum radius of the penumbra was related only to the ion energy, in MeV/nucleon, given by:

$$R_p = 0.768 \cdot E - 1.925 \cdot \sqrt{E} + 1.257 \quad \text{(micrometers)} \qquad \text{Equation C.2}$$

Where: E = energy of the incident ion (MeV/nucleon).

The fraction of energy deposited within a micrometer cylinder of tissue with radius *r* surrounding the ion track was then given by:

$$F = 0.5 + \frac{1 + 2\ln(r/r_c)}{4\ln(\sqrt{e}\, r_p / r_c)} \qquad \text{Equation C.3}$$

Table-C.1 presents the dimensions of the core and penumbra for the four ions of this study. Also included in the table is the LET of the particle and the amount of energy deposited in a one micrometer diameter cylinder of tissue.

Table-C.1
Radial Dimensions of the Core and Penumbra of Four Ions

Ion	Energy (MeV/nucleon)	LET (keV/μm)	Core Radius (nm)	Penumbra Radius (μm)	Energy Deposited in 1.0 μm Cylinder of Tissue (keV)
Nitrogen	79	43.1	4.48	44.8	32.7
Oxygen	119	40.9	5.35	71.6	30.3
Neon	211	43.8	6.69	135.3	31.5
Silicon	781	46.4	9.72	547.3	31.5

Radial Distribution of Dose

A more detailed description of the pattern of energy deposited at distances normal to a charged particle track was given by Cucinotta, et.al., in terms of the radial distribution of dose.[21] The distribution of electron energies ejected from the path of a charged particle in water, based on the calculations of Rudd,[34] was included in the model. The angular distribution of ejected electrons was determined by first

assuming that the most probable angle based on electron energy was given by classical kinematics as:

$$\cos^2(\theta) = w / w_m \qquad \text{Equation C.4}$$

where:

θ = angle of ejection relative to the forward direction of the ion,
w = energy of the given electron (eV), and
w_m = maximum energy the ion can transfer to a free electron (eV).

The double differential cross section of electron ejection, based in part on experimental measurement, was given as:

$$\frac{dn}{dw d\Omega} = \frac{dn}{dw} f(\theta, w) \qquad \text{Equation C.5}$$

and;

$$f(\theta, w) = \frac{N}{[\theta - \theta_c(w)]^2 + K/w} \qquad \text{Equation C.6}$$

where:

N = normalization constant,
K = 15 eV, determined from experiment, [79-82]
$\theta_c(e)$ = the root of Equation C.4

Results of Equations C.5 and C.6 are presented in Fig.C.1 as probability density distributions, as a function of angle of ejection, for electrons with an energy of 50 eV and 50 keV ejected from the path of silicon at 800 MeV/nucleon. For very low energy electrons there is almost an equal probability of the electron being ejected at any angle. Higher energy electrons are primarily distributed about the peak value

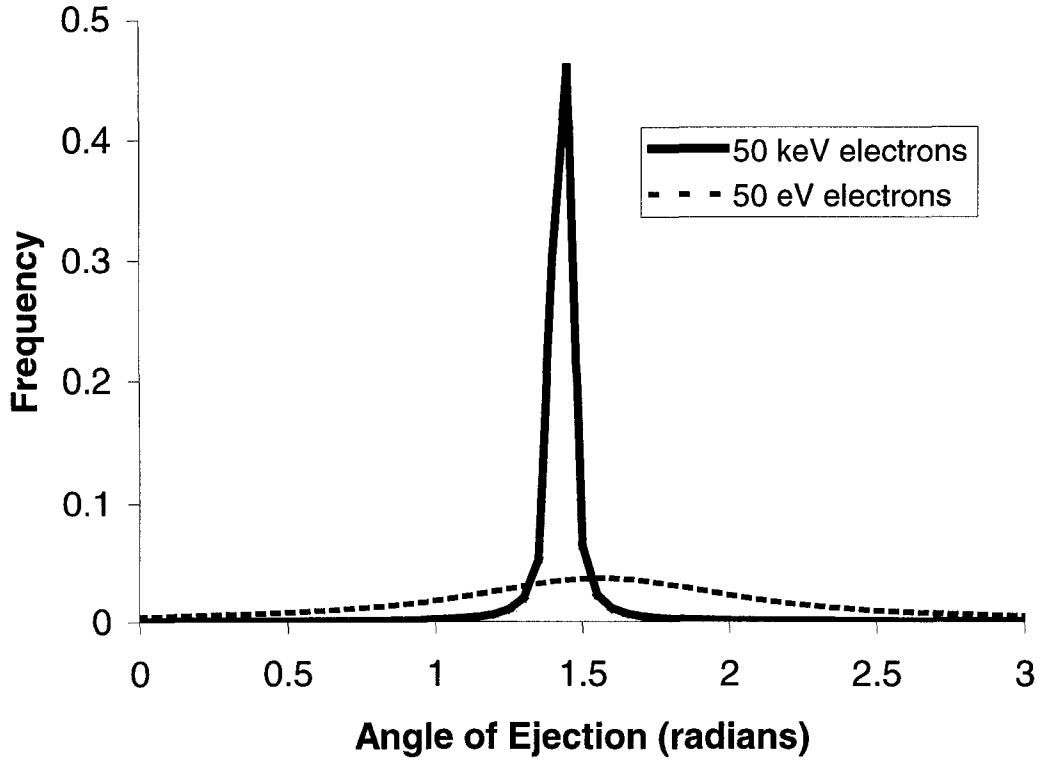

Fig.C.1. Frequency of Electron Production as a Function of Angle of Ejection. Calculations are based on an incident silicon ion accelerated to 800 MeV/nucleon traversing a volume of tissue. Maximum energy delta ray produced is about 2.5 MeV. The angle of ejection is with respect to the forward direction of the primary ion. Dashed line shows that for very low energy electrons, 50 eV, there is almost an equal probability of the electron being ejected at any angle. The solid line indicates that for higher energy electrons, 50 keV, the angle of ejection is peaked about the value found by classical scattering kinematics.

described by classical kinematics. Solving Equation C.6 for θ, the probability density distribution as a function of electron energy for a given angle may be found as presented in Fig.C.2 for ejection angles of 30 and 60 degrees from the forward direction of a silicon ion at 800 MeV/nucleon.

All energy deposition from all electrons intersecting a point ejected with energy w and angle θ, was assumed to be due to a events normal to the ion track with magnitude w/sin(θ). All possible ejection angles were considered and summed to give the portion of energy deposited at radial distance r. The mass of the cylindrical ring with a length of one micrometer and radius of r to r+dr was then included to arrive at dose.

Applying the radial dose model to the four ions analyzed in this study gives the distributions shown in Fig.C.3. Fig.C.4 shows the similarities between this model and Chatterjee's approach for silicon at 800 MeV/nucleon.

Simulated TEPC Response

Energy deposition in the volume of a spherical TEPC was simulated by Nikjoo, et. al., using track structure models.[20] The study was motivated by the experimental results of Rademacher[17] that showed anomalously large energy depositions for ions with trajectories equal to the radius of the TEPC cavity. This phenomena was attributed to either spallation, elastic scattering of the incident ion, fragmentation of the ion with neutron loss only, fragmentation of target nucleus only, or the increase in secondary electron production in the dense wall of the detector.[20]

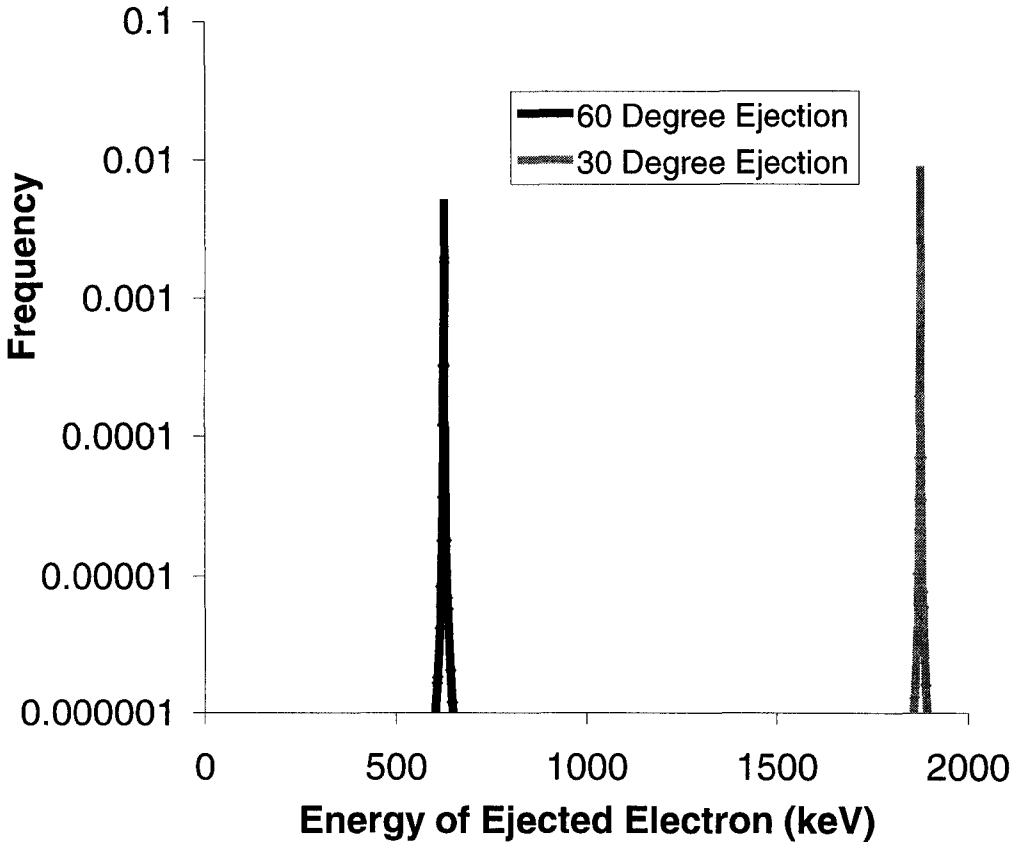

Fig.C.2. Electron Production as a Function of Energy for 30 and 60 Degree Angles of Ejection. Calculations were based on an incident silicon ion at 800 MeV/nucleon traveling through tissue. Higher energy electrons have smaller angles of ejection with respect to the forward direction of the incident ion. At 30 degrees, the most probable energy of electrons ejected is about 1.8 MeV (light line). At 60 degrees, however, the energy of ejected electrons is on the order of 650 keV (dark line).

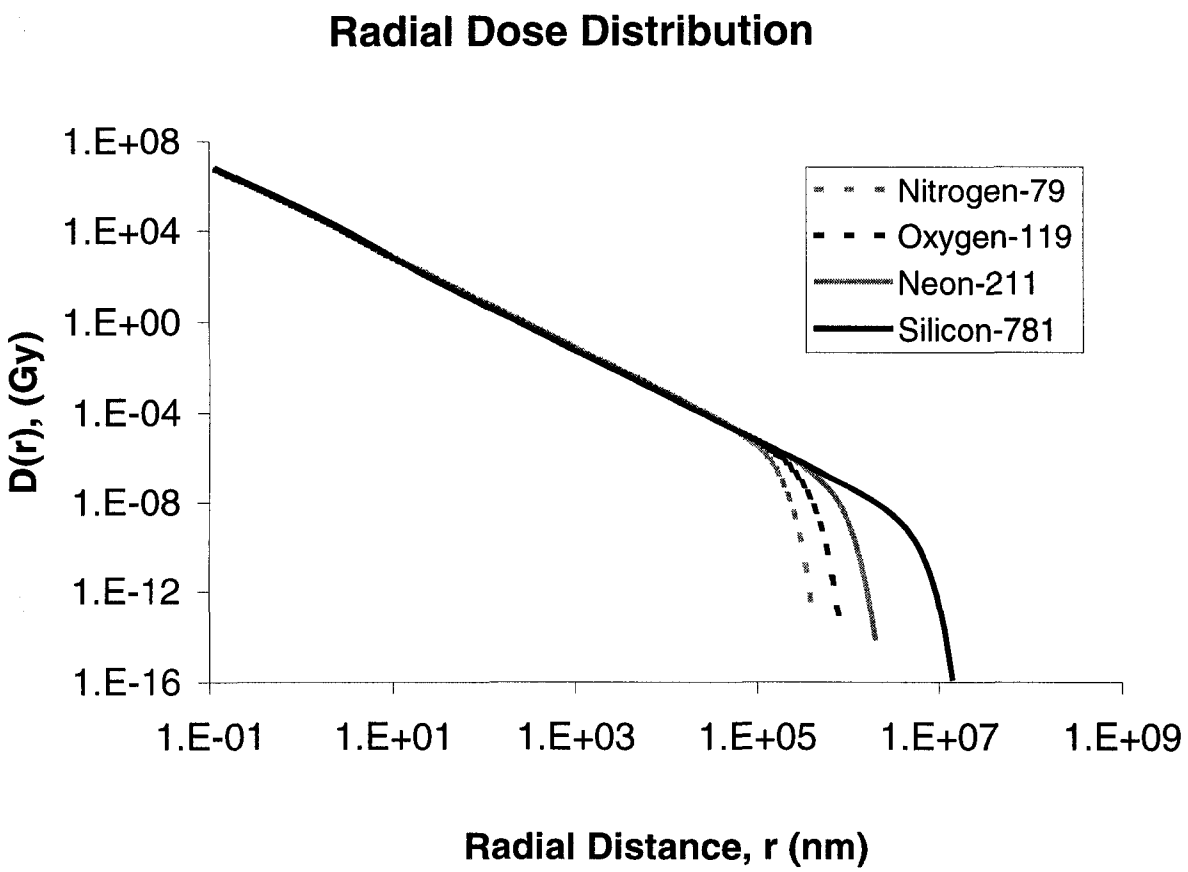

Fig.C.3. Radial Distribution of Dose for Ions Studied. The dose as a function of radial distance from the path of ^{14}N, ^{16}O, ^{20}Ne and ^{28}Si are plotted on a log-log scale to show the full extent of the distributions. The dose is is shown to be an inverse function of distance from the path of the ion. The distributions are very similar for all ions out to a radius of about 50 micrometers.

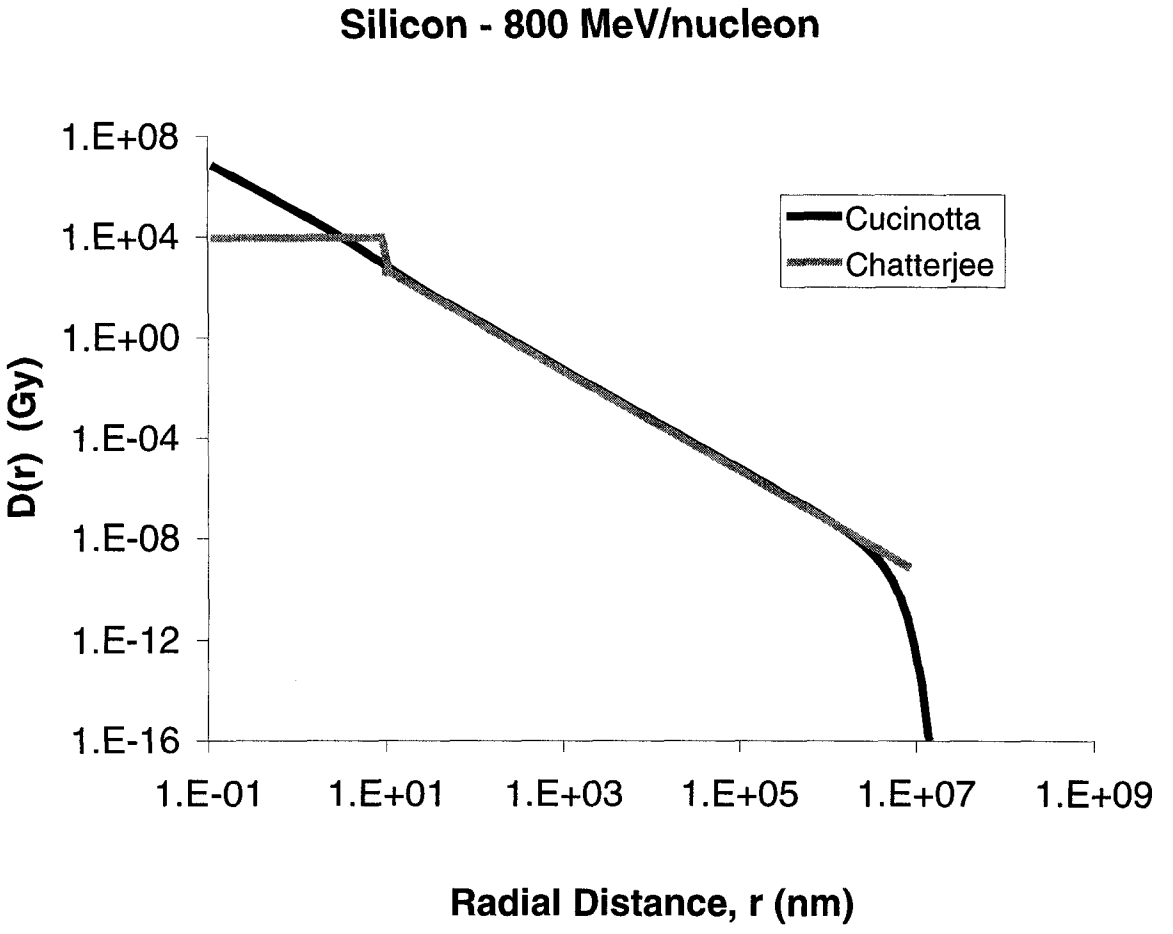

Fig.C.4. Comparison of Chatterjee and Cucinotta Methods of Determining Energy Loss of a Heavy Charged Particle. The dark line shows the method described by Cucinotta for an incident silicon ion at 800 MeV/nucleon interacting in a water media. The light line shows the results of the Chatterjee method, converted to a distribution of radial dose. The horizontal portion of the Chatterjee model is a result of the assumption that roughly half of the energy lost by the primary ion is in the dense region close to the ion path labeled the "track core".

The Monte Carlo code PITS[83] was used to generate locations and magnitudes of energy depositions surrounding a single charged particle track due to secondary electron emission. Results of energy loss calculated by PITS were in good agreement with values of energy loss published in ICRU report 49.[84] Furthermore, calculations of the radial distribution of dose surrounding the generated path of the ions compared well to experimental data.[20]

To simulate experimental conditions, a spherical volume with a diameter of 12.7 millimeters was incorporated into the model. Ion trajectories were chosen randomly representing a uniform irradiation. The range of the electron tracks ejected by the incident ion was expanded on intersection with the TEPC volume, mimicking the reduced pressure of the TEPC. For each incident ion, the location with respect to the center of the TEPC and total energy deposition in the sensitive volume was recorded. This process was repeated until the total response of the TEPC was logged.

Results modeling a walled TEPC was compared to a model of a homogenous wall-less detector. Results indicated that the large increase in energy deposition for particles with trajectories equal to the cavity radius was only observed in the case of the walled detector and was present due to an enhanced production of electrons in the dense wall. These results confirmed experimental findings of Rademacher studying the response of a spherical TEPC to 1,000 MeV/nucleon ^{56}Fe.[17]

Four locations of enhanced electron production were discussed. In relation to the volume of the detector, these were:

1) in front; enhanced energy deposition from electrons generated in the path of the ion track in front of the cavity,
2) inside; from primary ion and secondary electrons created inside the cavity,
3) behind; electrons created in the path of the track behind the cavity, and,
4) outside; from electrons generated by ion trajectories outside the cavity.

Both the walled and wall-less models showed that roughly 80% of the total energy deposition was due to condition (2), ions crossing the detector cavity with secondary electrons generated inside the volume. The remainder of energy deposited in the detector was partitioned differently depending on the presence or absence of the dense wall. For the wall-less model, the majority of the remaining energy was due to electrons generated by ions passing outside the detector cavity, item (4). The walled model showed most of the remaining energy deposited from ions crossing the detector volume, due to electrons created before the primary ion entered the cavity, item (1). There was a small contribution from item (3) in both cases, though larger in the walled detector.

This Study

Though the Chatterjee and Cucinotta approaches described above assumed a cylindrical geometry, both were, used to model energy deposition to a sphere. Thin cylinders (10 nm) with varying diameters were stacked together to simulate a one micrometer sphere. Energy deposition was calculated for each cylinder, given its radius, and divided by a factor of 100 to return energy deposition in the thin slice.

Energy deposition to each slice was added representing total energy deposition to the sphere for particles passing through its diameter. Results of the original cylindrical model and the spherical modification are given in Table-C.2. Since the volume of a one micrometer diameter sphere is less than the volume of a one micrometer, height and diameter, cylinder, energy deposition to the sphere was seen to be less.

Table-C.2
Applying Track Structure Models to a Spherical Geometry

		Energy Deposited in 1 μm Volume (keV)			
		Cylindrical		Spherical	
Ion	LET at TEPC (keV/μm)	Chatterjee	Cucinotta	Chatterjee	Cucinotta
Nitrogen	43.1	32.7	29.2	30.8	26.2
Oxygen	40.9	30.3	27.3	28.6	24.8
Neon	43.8	31.5	28.0	29.7	25.6
Silicon	46.4	31.6	28.1	30.0	25.8

Expanding on this approach, a code was written in C++ that repeats the process using very thin cylinders to determine energy deposition in a sphere, but does so for all possible ion trajectories. Cucinotta's approach to radial dose was first converted into the radial distribution of energy. A random ion trajectory was chosen with respect to the center of the sphere. The area of intersection of the sphere and one cylindrical shell of the track structure model was used to determine the fraction of energy retained in the sphere from total energy dissipated in the cylindrical shell.

Intersection with all possible radial shells were determined and added to give total energy retained in the sphere. A new trajectory was randomly chosen and the process repeated for a uniform irradiation.

A histogram was created, as shown in Fig.C.5, that represents the total response of the spherical volume in a homogenous medium to an irradiation by silicon at 800 MeV/nucleon. Since the simulation gives discrete values of energy deposition for a given impact parameter, the output was convoluted with a normal distribution representing the combined effects of energy loss straggling and detector resolution. The mean of the distribution used for folding assumed to be the energy occurring for the specific ion trajectory. The variance of the distribution was se equal to half the value of the mean as this reasonably modeled experimental conditions.

The location of about twenty percent of the energy deposited in the volume of the detector, in Nikjoo's study, was determined to be dependent upon the presence of the detector wall. For a homogenous medium, the wall-less detector, this energy was due to indirect events. In the non-homogenous case, the wall blocked many of these electrons, because of their short range. However, this loss of energy was compensated for by an increase in electron production in the wall for ions crossing the detector cavity. These were higher energy electrons ejected in the forward and backward directions. These energy depositions combine with the energy deposited by the ion crossing the volume and recorded as a single event. Thus, the average energy deposited from particles crossing the cavity of a homogenous detector should be eighty percent of the non-homogenous case. The energy deposition distribution of

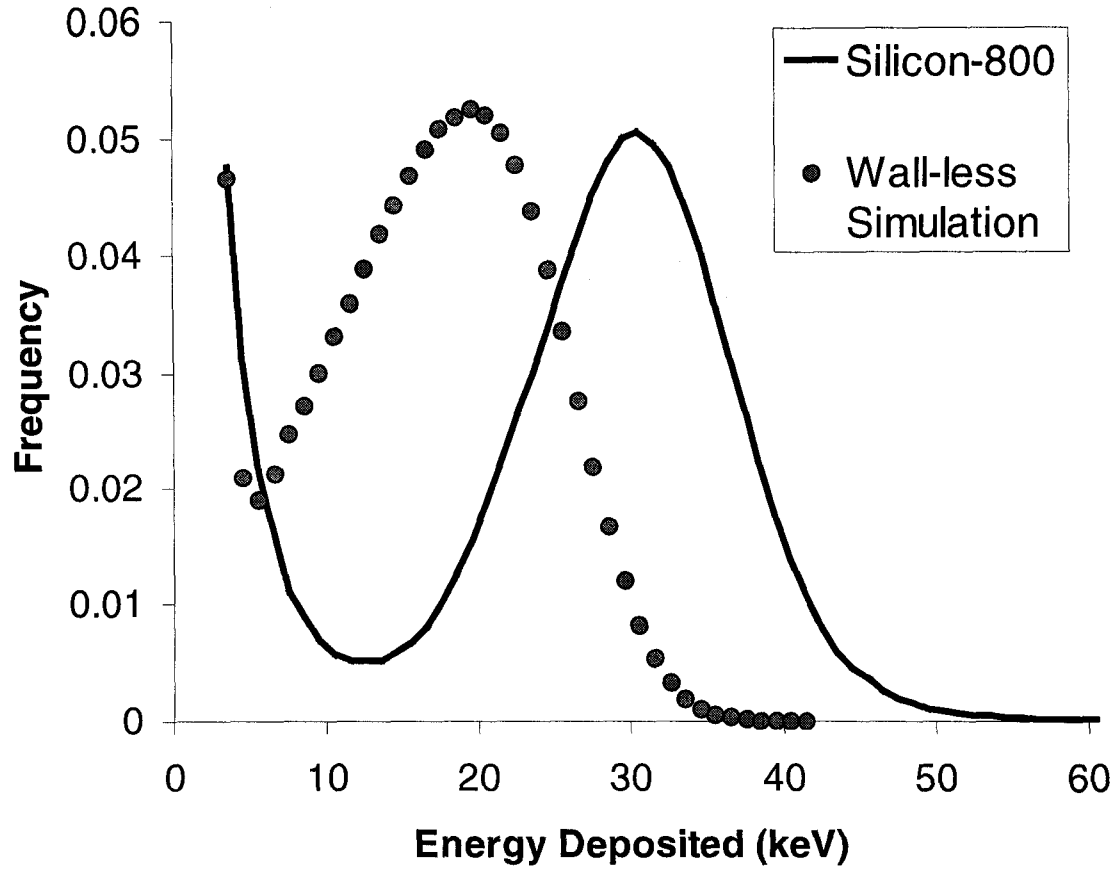

Fig.C.5. Simulation of TEPC Response Function in a Homogenous Medium Using the Radial Dose Model. Black line shows the response of a walled TEPC to silicon at 800 MeV/nucleon. Points represent a simulation of TEPC response using the radial distribution of dose described by Cucinotta. The shape of the simulation is similar to the measured distribution but with a lower mean value. This is due to the underlying assumption in the radial dose model of a homogenous medium. Particles crossing the cavity of a walled detector would be enhanced by an increased influx of electrons created in the detector wall. (see reference 20).

Fig.C.5 was augmented by this amount, only for cavity crossers, and compared to the measured distribution of silicon at 800 MeV/nucleon, as shown in Fig.C.6.

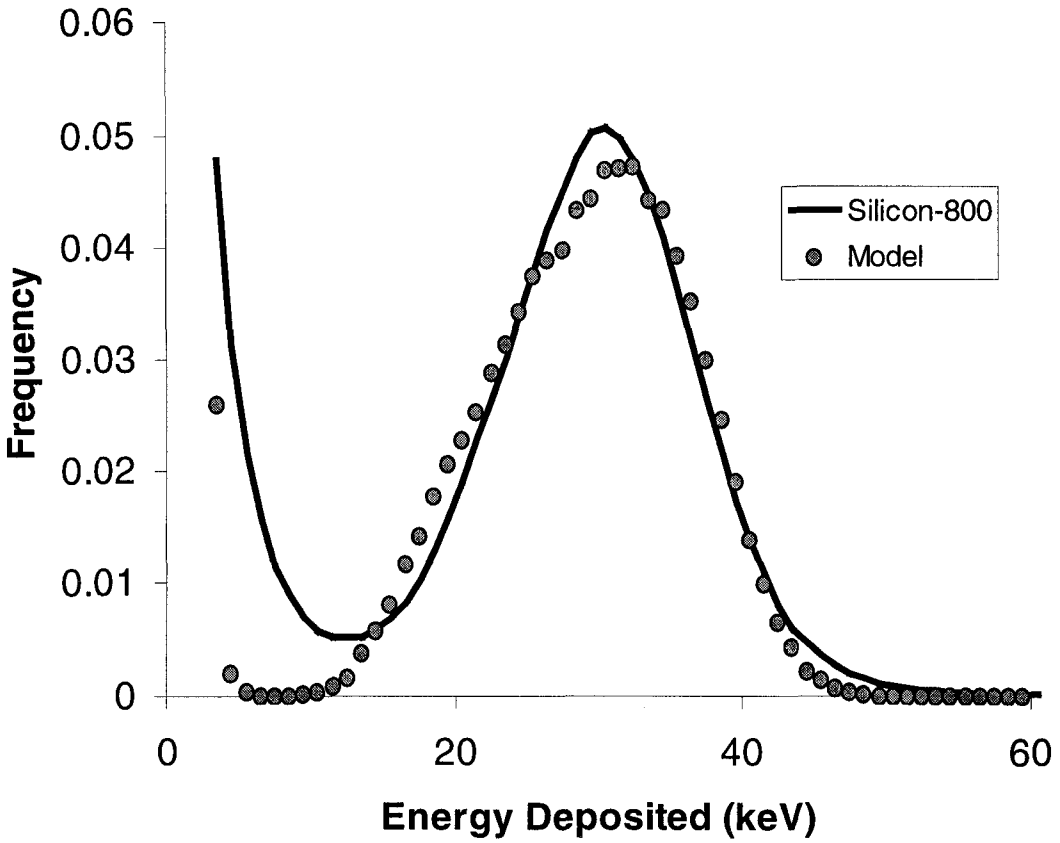

Fig.C.6. Simulation of TEPC Response Function Adjusting the Radial Dose Model for a Non-homogenous Medium. Black line represents measured TEPC response to silicon with an energy of 800 MeV/nucleon. Gray points show the simulated TEPC response to the same ion for a walled detector by enhancing energy deposition for particles crossing the detector volume.